ON THE POTENTIAL FOR INDUCED SEISMICITY AT THE CAVONE OILFIELD: ANALYSIS OF GEOLOGICAL AND GEOPHYSICAL DATA, AND GEOMECHANICAL MODELING

BY

Luciana Astiz - University of California San Diego

James H. Dieterich - University of California Riverside

Cliff Frohlich - University of Texas at Austin

Bradford H. Hager - Massachusetts Institute of Technology

Ruben Juanes - Massachusetts Institute of Technology

John H. Shaw –Harvard University

July, 2014

ON THE POTENTIAL FOR INDUCED SEISMICITY AT THE CAVONE OILFIELD: ANALYSIS OF GEOLOGICAL AND GEOPHYSICAL DATA, AND GEOMECHANICAL MODELING

Luciana Astiz

Associate Director of IGPP Real Time Data Array, Scripps Institution of Oceanography, University of California San Diego, La Jolla, CA 92093-0225, USA

James H. Dieterich

Distinguished Professor of Geophysics, Graduate Division, Department of Earth Sciences, University of California, Riverside, CA 92521, USA

Cliff Frohlich

Associate Director, Institute for Geophysics, University of Texas at Austin, Austin, TX 78758, USA

Bradford H. Hager

Director, Earth Resources Laboratory, Department of Earth, Atmospheric and Planetary Sciences, Massachusetts Institute of Technology, Cambridge, MA 02139, USA

Ruben Juanes

Associate Professor, Department of Civil and Environmental Engineering, Massachusetts Institute of Technology, Cambridge, MA 02139, USA

John H. Shaw

Chair, Department of Earth & Planetary Sciences, Harry C. Dudley Professor of Structural & Economic Geology, Harvard University, Cambridge MA 02138, USA

TABLE OF CONTENTS

EXECUTIVE SUMMARY

Production of substantial volumes of oil within tectonically active areas such as Southern California and Northern Italy has been ongoing since the early 20th century with no documented instances of triggered seismicity. However, the recent increase in seismic activity in more stable plate interior regions such as the central United States where new, largely unconventional oil and gas resources are being developed, has caused concern that human activity could trigger earthquakes. Although almost all documented cases of triggered seismicity are associated with injection of large volumes of fluids, not net production, it is natural and prudent to ask the question of the extent to which production of oil might trigger earthquakes.

In particular, the occurrence of a sequence of highly damaging earthquakes during May, 2012, near the Cavone oil field raised the question of whether these earthquakes might have been triggered, or, if not, if future activities might trigger other damaging events. The purpose of this report is to attempt to answer these questions given our current state of knowledge and state-of-the-art techniques in seismology, structural geology, tectonic geodesy, reservoir flow simulation, and geomechanics.

Because the likelihood of triggering earthquakes depends upon the current tectonic stress and rate of loading by ongoing deformation of the crust, we begin our study by examining the seismotectonic setting of the field. We analyze seismic data and previous studies to determine the rate, pattern, and style of deformation recorded in the geological record of folding and faulting. We also examine the rate of ongoing deformation observed using GPS, as well as the historical rate at which earthquakes comparable to the damaging May 2012 sequence occur. All three approaches give consistent results, showing deformation rates of ~ 1 mm/yr over distances of tens of kilometers, elastic stress accumulation rates of order 0.02 bars/yr, and the release of this accumulated elastic stress by earthquakes with typical rates of occurrence of about one per century somewhere in the region for magnitude $M_w = 6$ events.

To compare the tectonic rates of stress accumulation to the loading rates from production of oil and the associated lesser amount of injection of waste water in the Cavone field, we use reservoir models that include not only the pressure changes associated with the flow of pore fluids, but also the regional stress changes resulting from volumetric strain of the reservoir. We also identify the geometry and tectonic style of potentially seismogenic faults.

There are good records of the volumes of oil and water produced from and injected into all of the wells in the Cavone field since production began in 1980. In order to estimate the resulting fluid pressure changes, along with the changes in stress on the faults in the region, it

is necessary to determine the properties of the reservoir. Most important is the permeability structure; the porosity structure and compressibility structure are also important. These properties can be estimated from measurements on cores, from injection tests of wells, and from the history of pressure variations in wells on time scales of weeks to decades. The variation of these properties with position is more difficult to determine, making it necessary to carry out model sensitivity studies.

Analysis of the injection and interference tests during May and June, 2014 at the Cavone 14 injector well provide constraints on the permeability structure of the reservoir. The tests suggest that there are fractures that intersect the well, leading to high transmissivity within a region of many tens of meters around the well (negative skin effect). At ranges up to several hundred meters from the well, an average effective permeability of about 1.1 mD is appropriate. At larger distances, there some obstruction to flow is evident, with the effective permeability reduced to about 0.27 mD. There is also evidence from the temperature profile in this well that the injected water is penetrating some distance below the well, with communication to the aquifer below providing partial pressure support of the reservoir.

A simple analytical model that assumes that the injection and production occur at the top of a uniform porous half-space, capped by an impermeable layer, matches the observed pressure changes at the injector and producing wells. This simple model predicts that the fluid pressure changes and resulting Coulomb failure stress changes on faults at the hypocenters of the 20 May 2012 mainshock and 29 May aftershock are both negative, as well as being very small. For the dynamical model, the changes in Coulomb stress in the region near the May 29th hypocenter on the Mirandola fault is very small (< 0.01 bar) suggesting no effect of production and injection at the hypocenter. The May 20th hypocenter is on a different fault and farther from the Cavone field, outside the domain of the geomechanical study, and for which the pressure changes from reservoir operations is predicted to be zero in both dynamic models.

In order to examine the stress variations within several kilometers of the wells, a fully coupled fluid flow/poroelastic geomechanical model was developed. A mesh was constructed that honored the major structures of the reservoir, as well as the Mirandola fault. Models were run both without and with hydraulic support from the aquifer beneath the reservoir. An upper bound permeability of 1 mD was used to place a conservative upper bound on the distance that pressure changes could propagate and influence the state of stress. The model is driven by the actual production and injection history of the wells in the Cavone field.

Except within a few hundred meters of injector well Cavone 14, the fluid pressure within the reservoir is dominated by the net depletion of the field. Thus, beyond a few hundred meters from the injection well the pressure drops substantially, decreasing the likelihood of tectonic earthquakes occurring within the region in hydraulic communication with the reservoir. Outside but within a few kilometers of the reservoir, the stresses resulting from contraction of

the reservoir are in a sense to promote earthquake activity. However, the rate of increase of Coulomb stress from both fluid pressure and poroelastic stress, < 0.02 bars/yr, is comparable to the rate at which tectonic stress accumulates, and much less than the loading rates that have increased rates of seismicity elsewhere. In addition, analysis of the locations of aftershocks of the May 2012 sequence shows a lack of seismicity in the area where the stressing rates from contraction of the reservoir are largest. This observed lack of seismic activity within 1 – 2 km from the reservoir suggests that production of the Cavone field is not an important driver for seismicity.

Also, because reduction of fluid pressure promotes fault stability, there is no physical reason to suspect that pressure changes at their hypocenters associated with production or injection activities at the Cavone field triggered the May, 2012 sequence.

INTRODUCTION

Through the analysis of geological and geophysical data, and geomechanical modeling this report examines seismicity in the Emilia-Romagna region of northern Italy, in the context of oil production operations at the Cavone oil field.

The seismological literature commonly uses both the terms "induced" and "triggered" to describe earthquakes in which human activities have played some role. In many publications both terms are used interchangeably, while in others *induced earthquakes* are events where human activities are responsible for nearly all of the crustal stresses relieved by the earthquake — and in contrast, *triggered earthquakes* are events where the stress on a fault is tectonic, but human activities slightly perturb the stress, or frictional strength of the fault, allowing it to slip as an earthquake before this slip might have happened naturally. An obvious difficulty with the latter usage of these terms is that many earthquakes in which human activities played a role are neither purely induced nor purely triggered. Studies of crustal stress generally find elevated stresses nearly everywhere, even in continental interiors far from plate boundaries, and even where earthquakes are rare (Zoback and Zoback, 1980; Barton et al., 1995; Zoback and Townend, 2001). Consequently, in many, and perhaps most cases, tectonic stresses play an important role, even though human activities may have also contributed significantly to both the occurrence of, and stresses released, in the earthquake. Hence, for the purposes of this report we use the terms "induced" and "triggered" interchangeably. Also, in accordance with common usage in the scientific literature we also use the term *triggered earthquake* to denote purely tectonic earthquakes that occur in response to naturally occurring stress perturbations such as seismic waves, tidal stressing (in the solid earth or by ocean loading), and static Coulomb stress transfer from nearby earthquakes, which generates aftershocks.

An assessment of the potential of induced seismicity necessarily involves a number of components. These include

1) Characterization of the seismo-tectonic framework, including crustal deformation rates and background seismic activity due to tectonic processes. These are needed to provide a basis for evaluation observed seismic activity in the future. At Cavone, such assessments will be complicated somewhat by continuing aftershocks to May 2012 earthquakes.

2) Structural characterization and evaluation of potential earthquake faults that could be activated or affected by field operations.

3) Characterization of fluid pressures and poroelastic volume changes in, and around, the field and their evolution time. This is needed to evaluate effects of human-caused

stress changes on faults that may generate earthquakes. At Cavone an effort is currently underway to develop a detailed reservoir model.

4) Implementation of conceptual and/or quantitative physics-based models of induced seismicity to make projections of possible future activity under specific injection/production scenarios, and to evaluate seismic activity that will be observed in the future.

In this report:

Section 1 assembles and reviews available information on the tectonic framework of the region including earthquake history, characterization of tectonic structures, and evidence of recent and on-going tectonic deformation in and around the Cavone field.

Section 2 examines past seismicity including relevant technical details of the May 2012 earthquakes.

Section 3 reviews physical mechanisms for inducing earthquakes that have been proposed in the scientific literature. This includes assessment of the possible relevance of those mechanisms in the context of the conditions and structures in and around the Cavone field.

Section 4 describes the development ofmodels of pressure and stress changes associated with production of hydrocarbons and injection of waste-water in the region of the Cavone reservoir, , including constraints on reservoir properties from observed pressure changes accompanying reservoir production.

1 TECTONIC FRAMEWORK OF THE EMILIA-ROMAGNA REGION

1.1 SEISMOTECTONIC SETTING

The May 2012 Northern Italy earthquake sequence occurred in the eastern Po Plain, a tectonically active region situated between the Apennine mountains to the south and the Alps to the north. Crustal shortening during the Miocene generated a series of fold-and-thrust belts that border both the northern and southern Po Plain. Since the late Miocene, however, deformation has been localized in the southern Po Plain, which represents the foreland of the Apennine mountain belt (e.g., Pieri, 1983). The southern Po Plain contains three major tectonic arcs, or salients that extend north from the Apennine range front. The Cavone field and 2012 earthquake sequence are situated in the easternmost of these salients, known as the Ferrarese-Romagnolo arc (Figure 1.1.1).

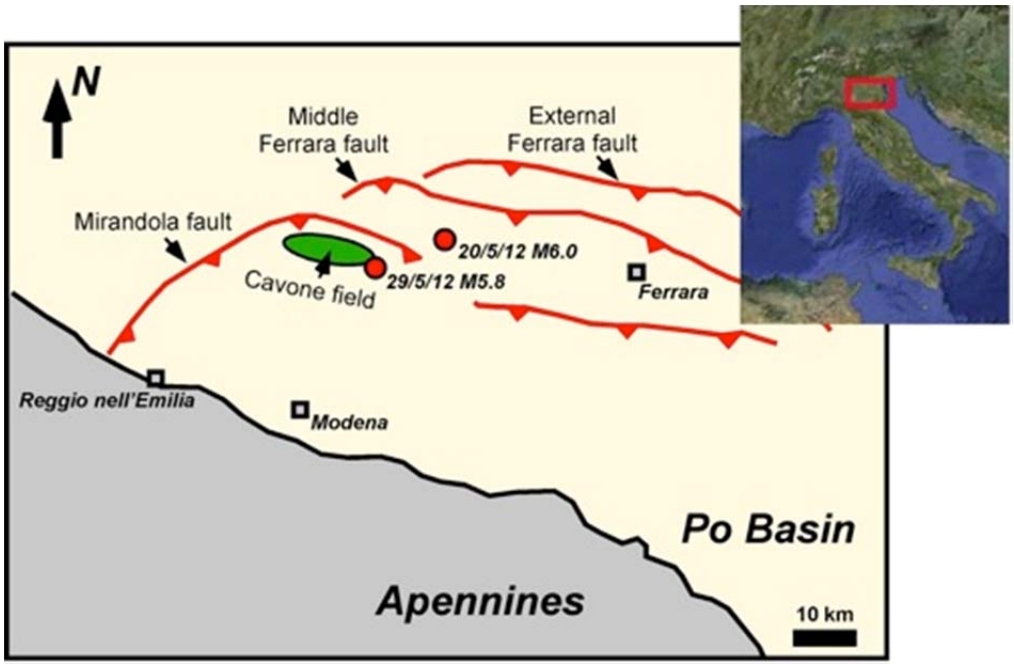

Figure 1.1.1: Regional map showing location of the Cavone oil field, epicenters of the two largest 2012 Emilia-Romagna earthquakes, and principal thrust faults.

Structures in the Ferrarese-Romagnolo arc are comprised of deep-seated reverse faults with tip-line or fault-propagations folds developed in their hanging walls (e.g., Pieri, 1983; Ciaccio and Chiarabba, 2002; Bonini, 2013). These structures involve a Triassic to Cretaceous carbonate platform sequence, which provides the main petroleum reservoirs, overlain by a Tertiary clastic section. Pliocene and younger syntectonic strata are locally up to 6 km thick, and generally bury the fold and fault systems. As a result, the active reverse faults are

typically blind. Blind faults do not reach the surface but rather have displacements that decrease upward into the cores of the overlying fault-related folds (e.g., Stein and Yeats, 1989; Shaw and Suppe, 1994). Folding of the overlying syntectonic strata record the Pliocene and Quaternary activity of these reverse faults (Shaw and Suppe, 1994, 1996; Pratt et al., 2002; Dolan et al., 2003).

The Po Plain, including the Ferrarese-Romagnolo arc, is seismically active. Within the arc, historical sources report a series of events occurred near the city of Ferrara. The most noteworthy earthquake sequence began early in the morning on 17 November 1570 and caused the collapse of many balconies and chimneys. This initial event was followed by several events that were felt strongly, with the largest occurring at approximately 19:10 (GMT) causing extensive damage to the buildings, churches and towers of Ferrara. Felt reports of this larger earthquake, Me 5.5 (estimated magnitude), indicate that the epicenter was at approximately 44.817 °N, 11.633 °E, (http://storing.ingv.it/cfti4med/). The extent of the felt area of the 1570 Ferrara earthquake is similar to that reported by the U.S.G.S. for the May 20th, 2012 event.

1.1.1 Historical Seismicity in the Emilia-Romagna Region

1.1.1.1 Summary of historical Activity

A search of the catalog of strong earthquakes in Italy (http://storing.ingv.it/cfti.4med/) indicates that historically there have been 103 events felt in the city of Ferrara before 1997; 26 of those events have estimated magnitude Me ≥. 4.0 and are listed in the Table 1.1.1.

The largest historical event that occurred in the Emilia-Romagna region prior to the 2012 earthquake sequence was the 1570 Ferrara earthquake (Me 5.5). This was preceded by the 1411 (Me 5.1) and 1346 (Me 4.9) events, which are listed as occurring near the city of Ferrara, as are all events that occurred prior to 1787. An event occurred on August 1, 1574 (Me 3.5) in a very similar location to the 9 January 1411 earthquake, Me 5.1, with its epicenter near the city of Ferrara at approximately 44.833 °N, 11.617 °E.

Eastward of Ferrara in the Ferrarense region three events occurred, two in 1922 (Me 3.7, 2.9) and one in 1931 (Me 4.8). To the west of Ferrara, i.e. toward the location of the Emilia-Romagna May 2012 earthquake sequence, several earthquakes are reported: near the town of Cento in 1916 (Me 3.7), and further west near Finale Emilia in 1908 (Me 4.3) and more recently in 1963 (Me 4.1). These events occurred within 10 km of the M_w 6.0 May 20, 2012 epicenter. Earthquakes in 1910 (Me 3.9) and 1912 (Me 3.2) near Mirandola also occurred within 10 km of the May 20 epicenter and within 5 km of the May 29, 2012 (M_w 5.8). The estimated magnitudes assigned to these historical earthquakes are greatly dependent on population distribution, felt and damage reports.

Table 1.1.1: Historical events with Me ≥ 4.0, from http://storing.ingv.it/cfti.4med/

Date	Time	Lat	Lon	Rel	Io	Imax	Sites	Me	Location
1978 12 30	10:38:46	44.867	11.05	b	4.5	4.5	7	4	Bassa mantovana
1978 12 25	22:53:41	44.85	10.983	b	5	5.5	28	4.5	Bassa mantovana
1970 11 02	08:42:12	44.85	11.167	b	4.5	5.5	3	4.1	Bassa modenese
1963 04 05	13:49:42	44.833	11.267	b	4.5	5.5	6	4.1	Finale Emilia (MO)
1931 03 27	***02:46:57***	***44.817***	***11.767***	***b***	***6***	***6***	***7***	***4.8***	***Ferrarese***
1922 05 25	04:23	44.867	11.517	b	3.5	4.5	5	3.7	Ferrarese
1922 05 24	21:17:25	44.817	11.4	b	4	4.5	7	3.9	Ferrarese
1916 06 20	19:30	44.783	11.45	b	3.5	4	2	3.7	Cento (FE)
1912 02 24	09:30	44.883	11.067	b	2.5	2.5	12	3.2	Mirandola (MO)
1910 03 22	23:29	44.817	11.167	b	5	5.5	15	4.3	Bassa modenese
1910 03 22	23:32	44.833	11.133	b	4	4	1	3.9	San Felice sul Panaro (MO)
1908 06 28	03:19:58	44.833	11.333	b	5	6	15	4.3	Finale Emilia (MO)
1901 01 20	06:34:20	44.883	11.083		5	5	12	4.2	Bassa modenese
1901 01 20	06:30	44.9	11.1		4	4	10	4	Bassa modenese
1787 07 26	***07:15***	***44.833***	***11.617***	***b***	***6.5***	***6.5***	***1***	***4.9***	***Ferrara***
1787 07 16	10:00	44.833	11.617	b	5.5	6.5	3	4.5	Ferrara
1678 07 15	-	44.833	11.617	b	5	5	1	4.3	Ferrara
1594 10 03	-	44.833	11.617	b	5	5	1	4.3	Ferrara
1574 08 01	-	44.833	11.617		3	3	1	3.5	Ferrara
1570 11 17	***19:10***	***44.817***	***11.633***	***b***	***7.5***	***8***	***60***	***5.5***	***Ferrara***
1561 11 24	01:25	44.783	11.45	b	5.5	6.5	5	4.5	Ferrara
1411 01 09	***02:00***	***44.833***	***11.617***	***b***	***7***	***7***	***1***	***5.1***	***Ferrara***
1409 08 17	00:35	44.833	11.617	b	6	6	1	4.7	Ferrara
1409 08 14	08:45	44.833	11.617	b	4	4	1	3.9	Ferrara
1346 02 22	***11:00***	***44.833***	***11.617***	***b***	***6.5***	***7.5***	***5***	***4.9***	***Ferrara***
1339 11 16	14:10	44.833	11.617	b	6	6	1	4.7	Ferrara

Note that the epicenter of the 1970 event is located almost equidistant (~ 6 km) of the 20 and 29 May 2012 earthquakes. The historical seismicity in the surrounding region of the May 2012 earthquake sequence clearly indicates that this region is tectonically and seismically active.

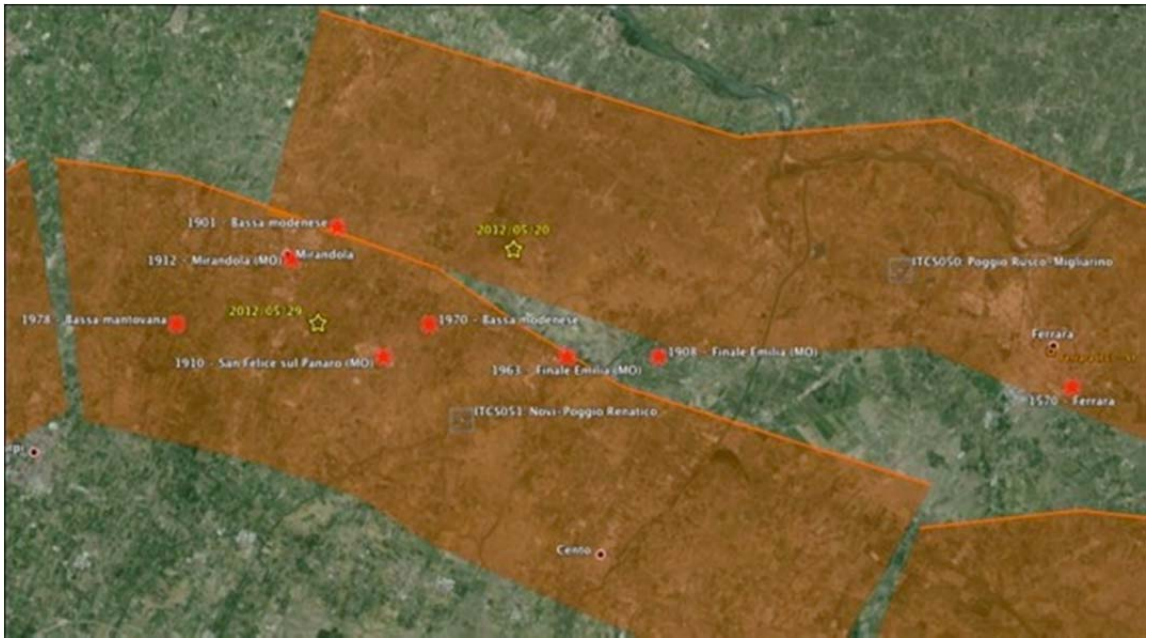

Figure 1.1.2: Yellow stars show the location of the May 20 and 29, 2012 earthquakes and red stars the location of events occurred before 1997 in the Emilia-Romagna region. The orange surface to the north represents the Middle and External Ferrara faults and that to the south the Mirandola fault (DISS, 2007).

A more detailed study of historical seismicity in the Emilia-Romagna region was done by Castelli et al (2012) to ascertain the completeness of the Italian historical catalog from the historical catalog in the Mirandola region, their preliminary conclusion was that in December 15, 1761 strong shaking was felt in Mirandola but there is no damage reported, however, this event was felt in Carpi and Modena. No magnitude has been estimated for this event.

All events listed above and those shown in Figure 1.1.2 occurred before the establishment of the Cavone oil field in 1982.

1.1.1.2 Felt reports from the 1570 earthquake near Ferrara, Italy.

The following description of the 1570 Ferrara earthquake was translated from: http://storing.ingv.it/cfti4med/. "The sources agree in Ferrara that a long series of earthquakes began in the early hours of 17 November and continued throughout the day. The time in which the four strongest events happened is remembered with accuracy: the first occurred at 9:30 am Italian (1:40 GMT approximately), causing the collapse of many blackbirds, balconies and chimneys, which damaged many roofs as they fell. Several aftershocks were followed during the night and the following morning, among which were the strongest at 20 hours Italian time, (24:10 GMT), violently shaking houses, and slightly damaging walls, and at about 24 hours Italian time (16:10 GMT), another event occurred, causing the collapse of chimneys and eaves as well as serious injuries in the masonry. The main shock occurred at

19:10 GMT approximately, shaking buildings that were already heavily damaged and uneven causing even more serious damage. In Ferrara the medieval part of the city was especially damaged, with some buildings collapsing completely and almost all the other structures had a wall or part of the roof fall, or disconnecting walls, which made the city largely uninhabitable as damage was extensive to both public buildings and private homes. The greatest damage was done to the tall buildings: churches, bell towers, and buildings with vaulted ceilings. The tremors destroyed all the buildings located near the corners of the street, as these buildings were not supported by others. Private construction suffered damaged to about 40% of the homes. Outside the city, there was considerable damage within a radius of about 15 - 20 km, approximately 30 towns and villages of the countryside, documented damage to churches. The earthquake was felt across a wide area including the main cities of Emilia, Milan, Padua and Venice in the north and Pesaro to the south. The overall picture of the effect is cumulative shock of 17 November. Numerous and frequent aftershocks were remembered and described by sources until the first months of 1572, some tremors were felt as well in 1573 and in 1574."

Italian version:

'*Le fonti ferraresi ricordano concordemente una lunga serie di scosse iniziata nelle prime ore del 17 novembre e continuata per tutta la giornata. Le quattro più forti sono ricordate con precisione oraria: la prima avvenne alle ore 9:30 italiane (1:40 GMT ca.) e causò il crollo di molti merli, terrazzini e comignoli, che cadendo danneggiarono molti tetti. Numerose repliche si susseguirono durante la stessa notte e nella mattinata successiva; fra queste le più forti furono quella delle ore 20 italiane (12:10 GMT ca.), che scosse violentemente le case, lesionando leggermente le murature, e quella delle ore 24 (16:10 GMT ca.), che causò il crollo di comignoli e cornicioni e gravi lesioni nelle murature. La scossa principale avvenne alle ore 3 (19:10 GMT ca.), colpì edifici già notevolmente lesionati e sconnessi e causò i danni più gravi. A Ferrara fu danneggiata soprattutto la parte medievale della città, dove alcuni edifici crollarono totalmente e quasi tutti gli altri subirono caduta di muri e tetti, lesioni e sconnessioni di pareti, che resero in gran parte inagibili sia gli edifici pubblici, sia le abitazioni private. I danni maggiori riguardarono gli edifici sviluppati in altezza: chiese campanili, palazzi con soffitti a volta. Le scosse colpirono soprattutto gli edifici posti all'estremità delle vie, che non erano sostenuti da altre costruzioni. Diversi dettagli si hanno anche sull'edilizia privata: risulta danneggiato circa il 40% delle abitazioni. Fuori dalla città, in un raggio di circa 15-20 km, notevoli danni subirono circa 30 paesi e villaggi della campagna, dei quali sono documentati soprattutto i danni agli edifici religiosi. La scossa fu sentita in una vasta area comprendente le principali città emiliane, Milano, Padova e Venezia a nord; Pesaro a sud. Il quadro complessivo degli effetti è cumulativo delle scosse del 17 novembre. Numerosissime e frequenti furono le repliche ricordate e descritte dalle fonti fino ai primi mesi del 1572; qualche scossa fu avvertita anche nel 1573 e nel 1574.'*

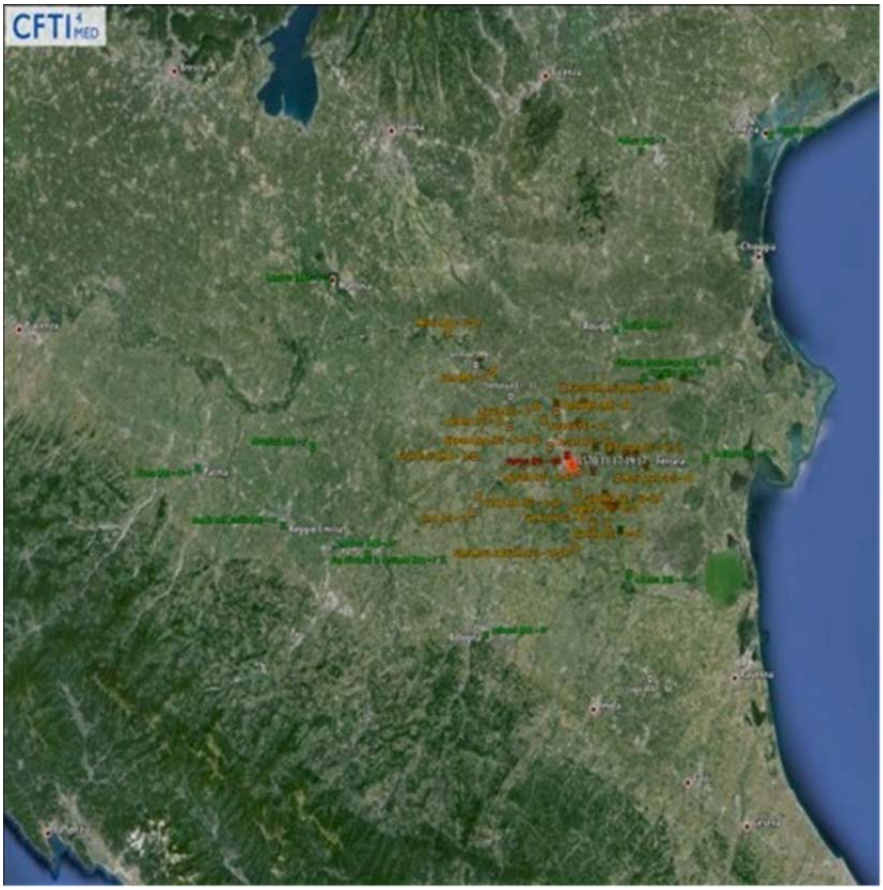

Figure 1.1.3: The red circle shows the location of the 1570 Ferrara earthquake, the name of cities and towns where earthquake damage was severe (I >5) are shown in orange, green labels show locations where the earthquake was felt.

The USGS Shake Maps shown in Figures 1.1.4 and Figures 1.1.5 display the felt area of the May 20 and 29, 2012 earthquakes which are similar to the pattern shown in Figure 1.1.3 from the 1570 Ferrara earthquake, i.e. a concentrated damage area and an extensive felt region indicating that this XVI century earthquake probably occurred in external blind thrust of the Ferrarese-Romagnolo arc.

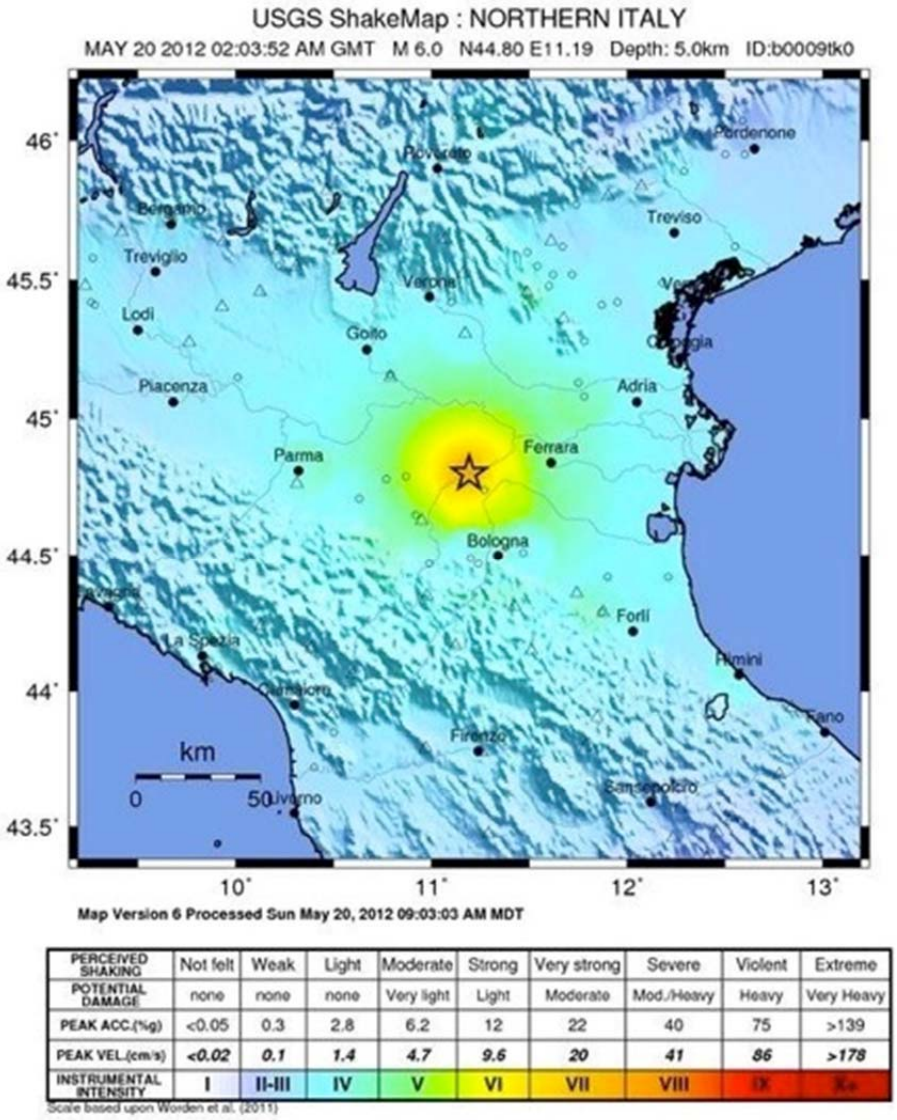

PERCEIVED SHAKING	Not felt	Weak	Light	Moderate	Strong	Very strong	Severe	Violent	Extreme
POTENTIAL DAMAGE	none	none	none	Very light	Light	Moderate	Mod./Heavy	Heavy	Very Heavy
PEAK ACC.(%g)	<0.05	0.3	2.8	6.2	12	22	40	75	>139
PEAK VEL.(cm/s)	*<0.02*	*0.1*	*1.4*	*4.7*	*9.6*	*20*	*41*	*86*	*>178*
INSTRUMENTAL INTENSITY	I	II-III	IV	V	VI	VII	VIII	IX	X+

Figure 1.1.4: ShakeMap for the 20 May 2012 (Mw 6.0) earthquake.

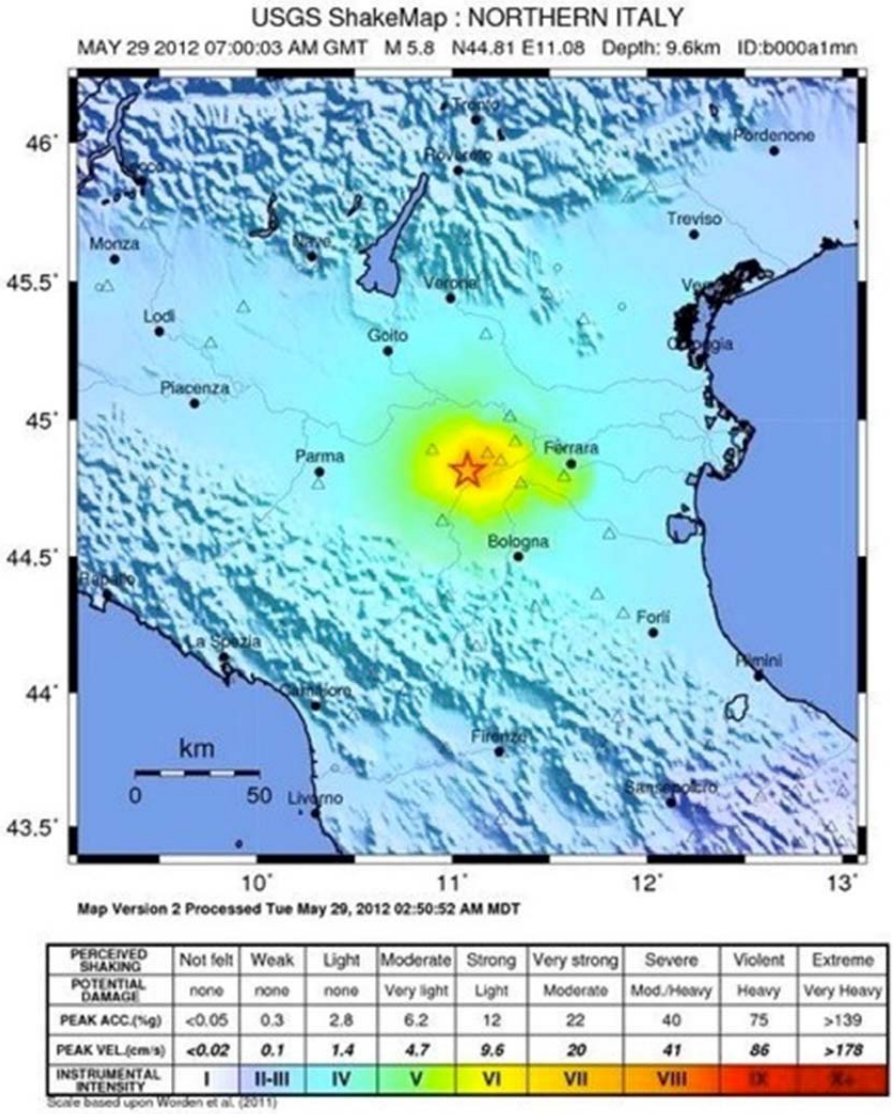

Figure 1.1.5: ShakeMap for the 29 May 2012 (Mw 5.8) earthquake.

1.2 CAVONE STRUCTURE

We investigated the geometry and tectonic activity of the Cavone structure and other thrust sheets in the Ferrarese-Romagnolo arc using seismic reflection profiles and well data provided by the operators of the Mirandola concession (Figure 1.2.1). These data were evaluated in conjunction with earthquake focal mechanisms provided by INGV and the U.S.G.S. (Table 2.2.1) to generate a series of cross sections and a 3D structural model that define the location and geometry of the Cavone structure and other tectonic elements in the region (Figure 1.2.2).

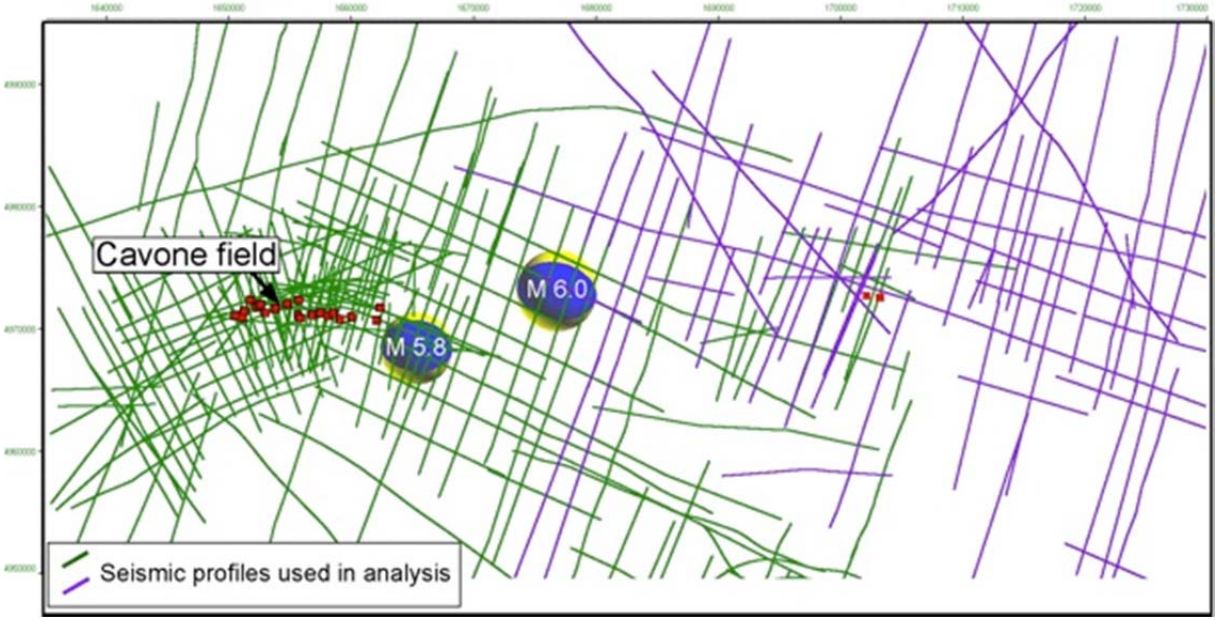

Figure 1.2.1: Basemap of the study area showing seismic reflection profile traces, wells from the Cavone field, and the location and focal mechanisms of the 2012 M 6.0 and 5.8 earthquakes (INGV-Table 2.2.1).

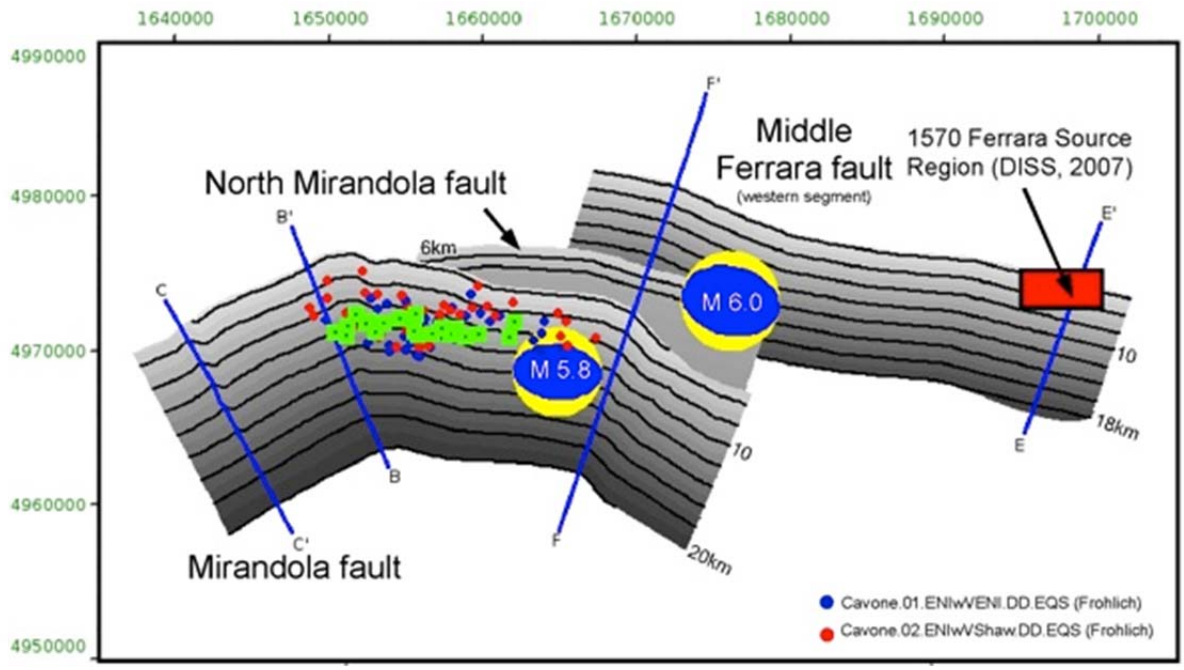

Figure 1.2.2: Map showing location and geometry of the Mirandola fault and adjacent structures with the 2012 Northern Italy (M 6.0 and M 5.8) earthquakes (INGV Table 2.2.1) and select relocated aftershocks. Traces of seismic lines and cross sections in this report are shown.

The Cavone structure is representative of the deformational styles of the Ferrarese-Romagnolo Arc, consisting of a north-vergent fault-propagation fold overlying a steeply south-dipping reverse fault (Mirandola fault). Seismic reflection profiles provided by the operators are of high quality on the western and eastern limits of the fold trend, and constrain the fold geometry, fault location, and fault dip (Figure 1.2.3). The Cavone fold includes a moderately dipping (≈ 45°) southern backlimb, and a steep (≥60°) northern forelimb. Pliocene syntectonic strata onlap the forelimb and thin onto the crest of the structure. These strata are overlain by a Quaternary section that is gently warped over the fold crest. The Mirandola fault underlies the forelimb of the fold, and based on reflection truncations dips to the south at about 60° to depths below 10 km. There is a thickened section of Triassic strata in the hanging wall of the Mirandola fault (Figure 1.2.4). This suggests that the Mirandola reverse fault reactivated a Triassic-age normal fault, consistent with its steep dip. A series of fault splays and backthrusts are present in the hanging wall of the Mirandola fault. These secondary faults appear to merge with the main Mirandola fault at depths between 7 and 12 km.

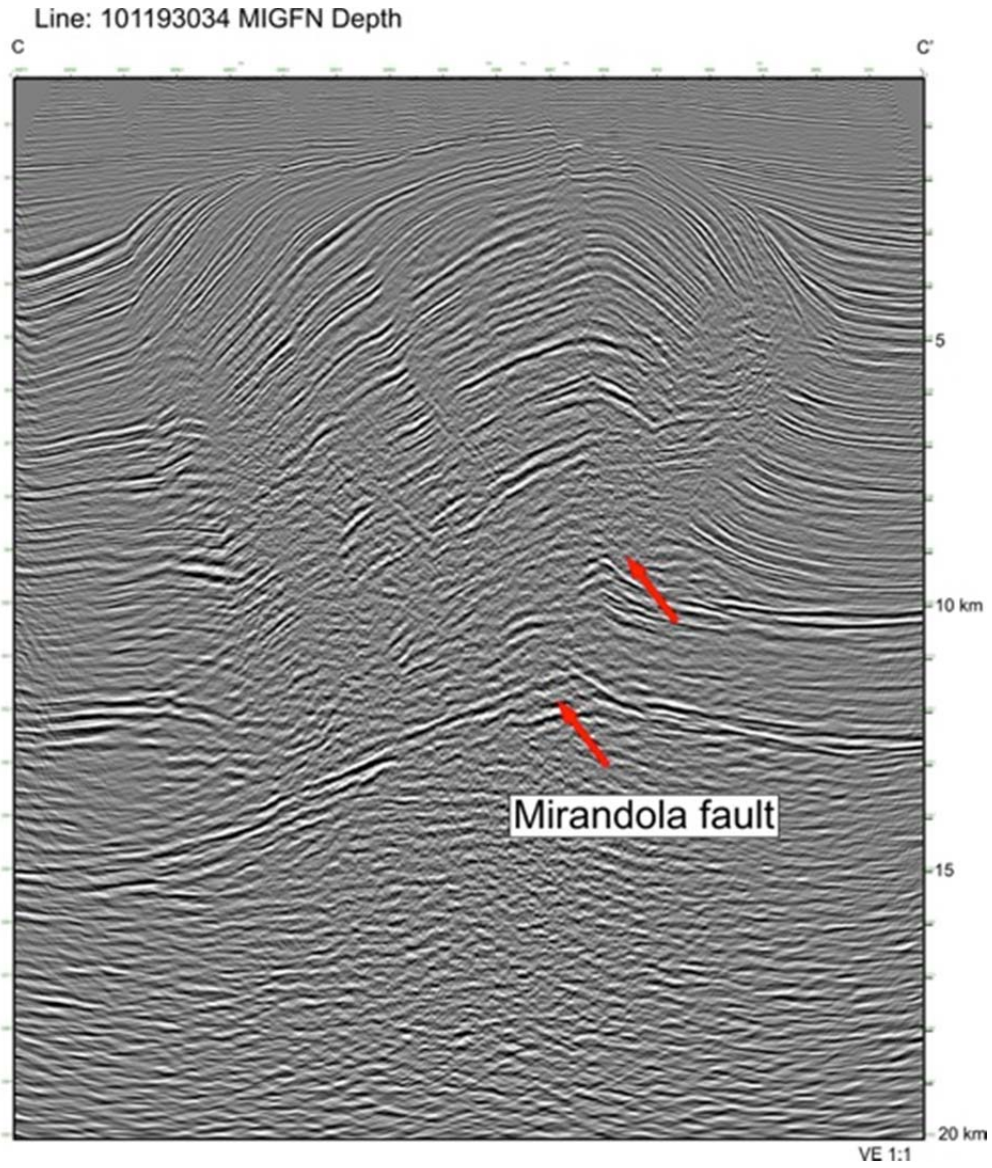

Figure 1.2.3: Migrated and depth converted seismic reflection profile C-C' from the western part of the Cavone structure, showing direct constraints on the location and dip of the Mirandola fault. Seismic section was depth converted using velocity model derived from sonic logs in the oil field.

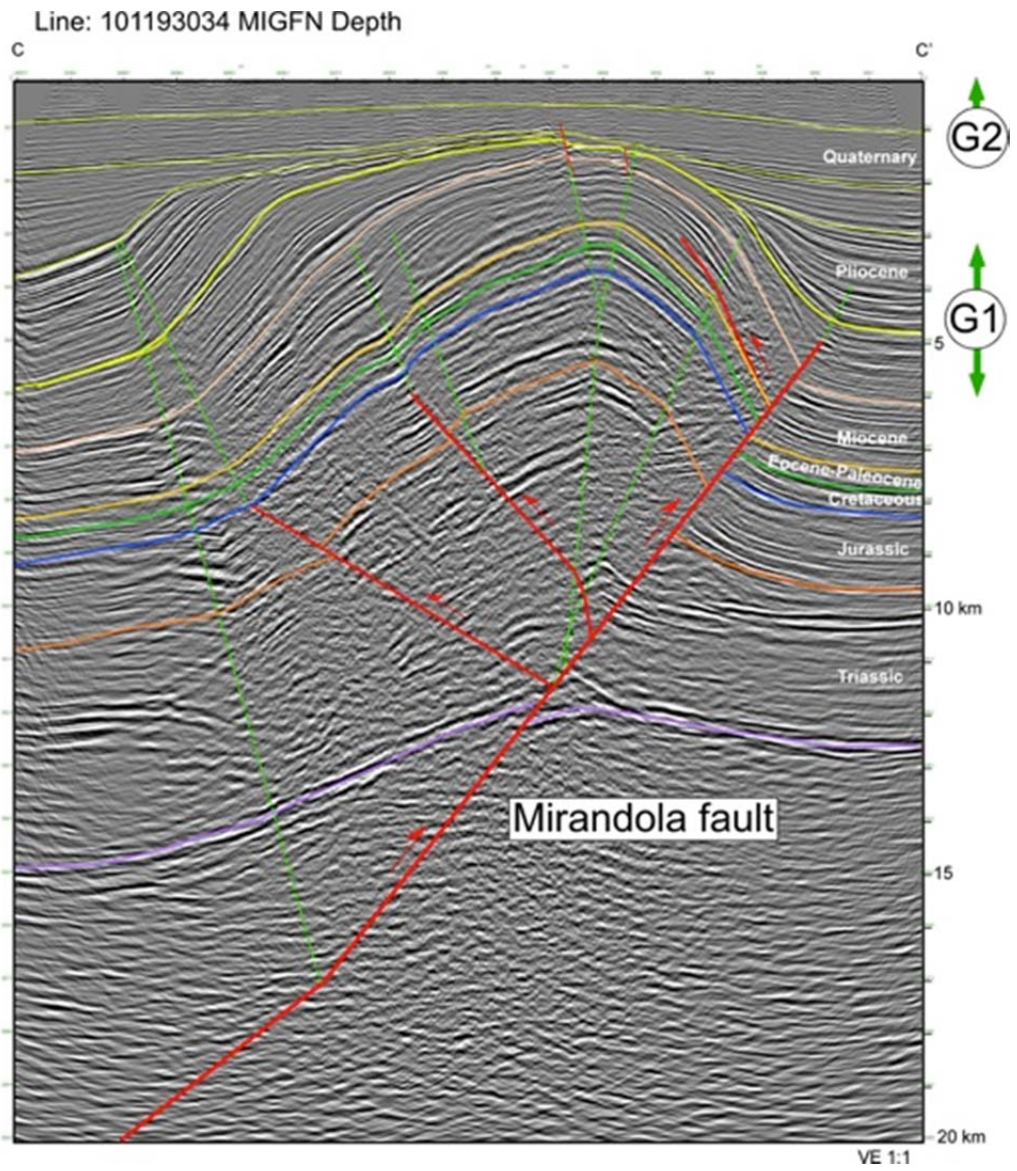

Figure 1.2.4: Interpreted version of section C-C' showing geometry of Mirandola fault and overlying fault-propagation fold.

The amplitude of the fold grows toward the center of the Cavone trend forming the structural trap for the oil field (Figure 1.2.5). Based on our interpretation, the fault has a curved shape, concave to the south, and extends for about 30 km along strike (Figure 1.2.2). Three other reverse faults (the Northern Mirandola, Middle Ferrara, and External Ferrara faults, nomenclature after Pezzo et al., 2013) step to the northeast in the footwall of the Mirandola fault in an en echelon pattern. All of the faults have overlying fault-propagation folds. The Northern Mirandola may merge with the Mirandola fault at intermediate crustal depths (5-10km), whereas the Middle and External Ferrara faults clearly extend to depth as distinct structures.

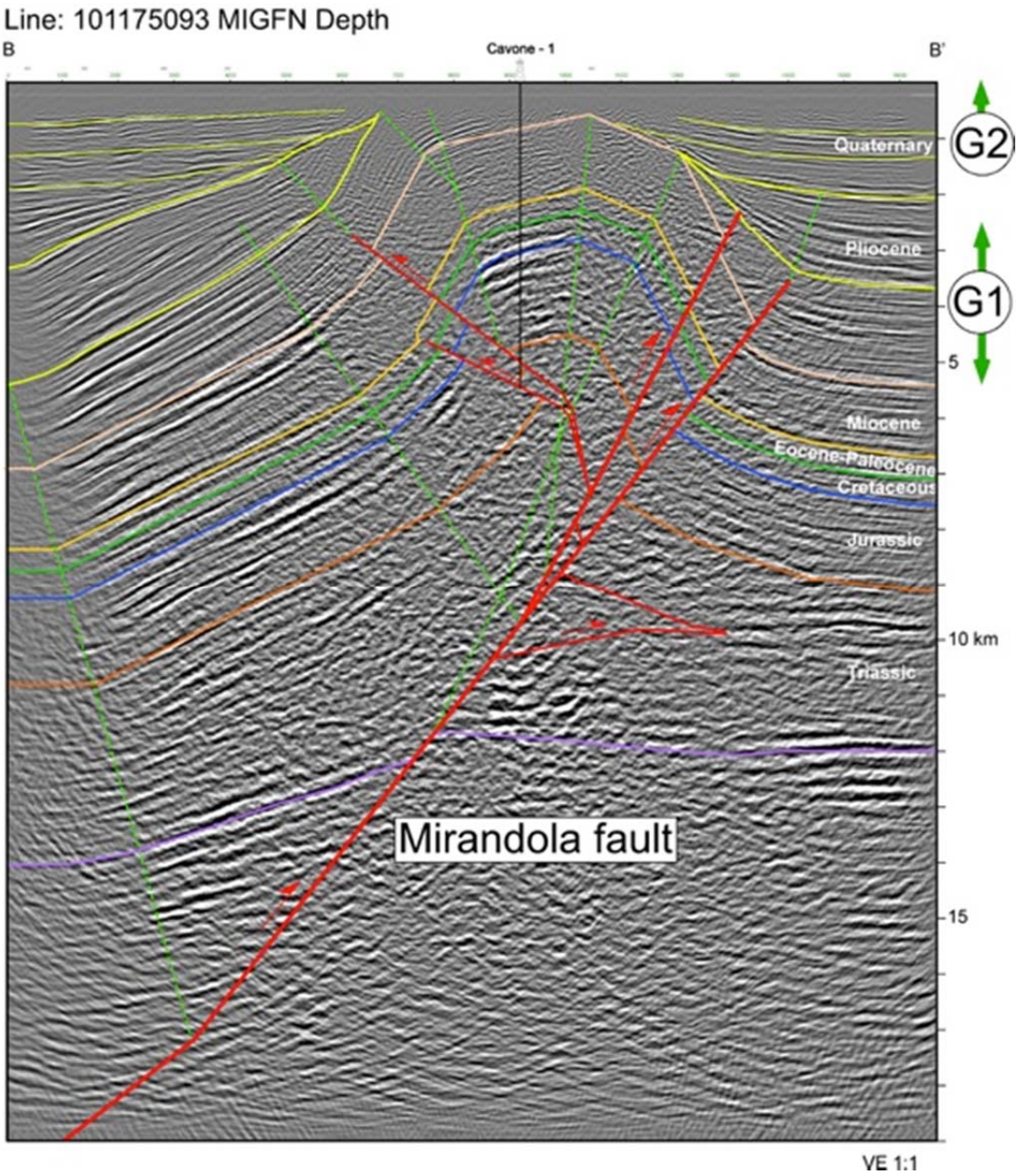

Figure 1.2.5: Migrated and depth converted interpretation of seismic profile B-B' showing geometry of the Mirandola fault and overlying Cavone fault-propagation fold. Seismic section was depth converted using velocity model derived from sonic logs in the oil field.

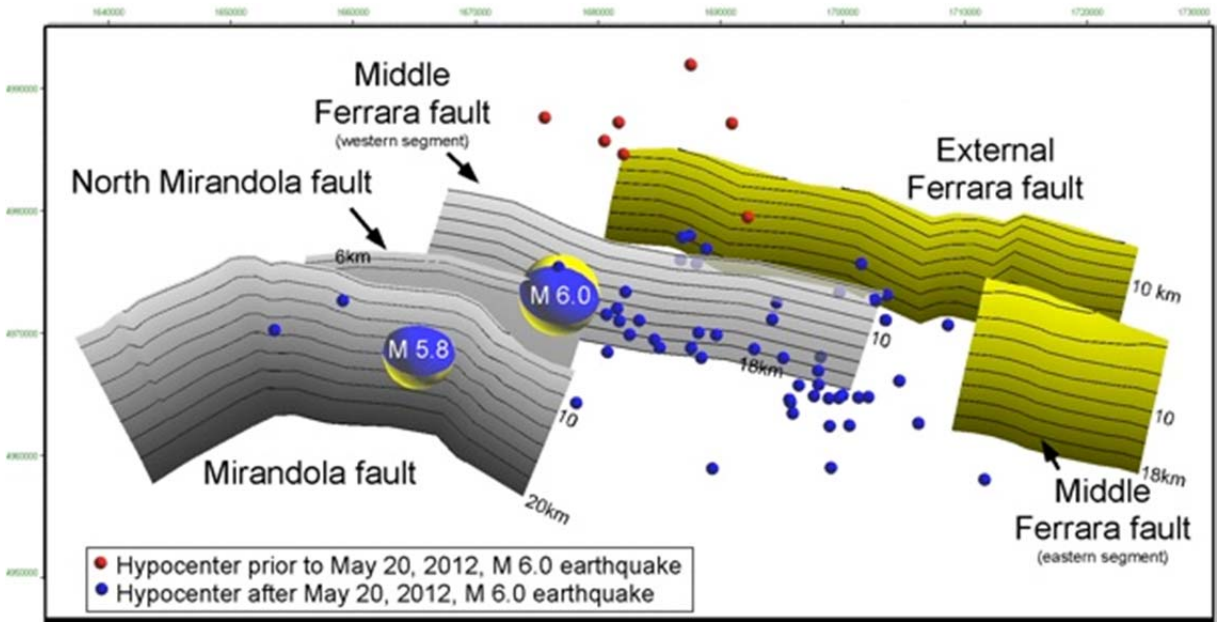

Figure 1.2.6: Base map showing locations and geometries of the major thrust systems in the study area. Epicenters are shown from the local Ferrara Municipality network prior to and after the May 20 earthquake (March 2010 to September 2013).

1.3 GEOLOGIC EVIDENCE FOR TECTONIC ACTIVITY OF STRUCTURES IN THE FERRARESE-ROMAGNOLO ARC

Given that faults in the Ferrarese-Romagnolo arc are generally blind, traditional paleoseismologic methods of trenching across fault scarps cannot resolve the fault activity. Rather, deformation and uplift of syntectonic strata above the folds that lie in the hanging walls of these thrust sheets record the fault activity and slip rate. These syntectonic strata indicate that the Mirandola-Cavone structure grew in two distinct phases of deformation (Figure 1.2.4 and Figure 1.2.5). The initial period of tectonic activity (G1) occurred in the Pliocene, as evidenced by the onlap of folded Pliocene strata onto the forelimb and backlimb of the structure. These Pliocene strata reach thicknesses of more than 5km to the north and south of the structure, but are completely absent on much of the fold crest. The Pliocene and older strata are unconformably overlain by Quaternary sediments, which extend across the fold crest and bury the structure. The lowermost Quaternary sediments also onlap the fold crest. In contrast, the overlying Quaternary strata appear to maintain their thickness as they extend across the fold crest. This implies a period of reduced activity or tectonic quiescence on the Mirandola fault. The entire Quaternary section is, however, deformed along the syncline pinned to the tip of the Mirandola fault and is warped above the crest of the fold. This implies a second phase of activity on the Mirandola fault and the Cavone fold (G2) in the mid- to late Quaternary.

This second, recent phase of tectonic activity is consistent with the study of Scrocca et al. (2007), which used patterns of deformed growth strata to define the Late Quaternary activity

of the Mirandola fault (Figure 1.3.1). This study accounted for sedimentary compaction of growth strata (a process that can produce structural relief of sedimentary horizons in the absence of tectonic activity), and defined uplift rates of 0.16 to 0.53 mm/year over the past 1.4 Ma. Moreover, other studies in the region have inferred the tectonic activity of blind thrust faults in the southern Po Plain. Burrato et al. (2003) identified several anomalous stream patterns in the Ferrarese-Romagnolo arc that were interpreted to reflect active uplift of anticlines in the hanging walls of blind faults. Three of the anomalous river profiles occurred above the Mirandola, Middle Ferrara, and External Ferrara fault systems, suggesting late Quaternary tectonic activity of these structures. Thus, both the patterns of deformed growth strata and drainage patterns provide geologic evidence of recent tectonic activity on thrust faults in the Ferrarese-Romagnolo arc.

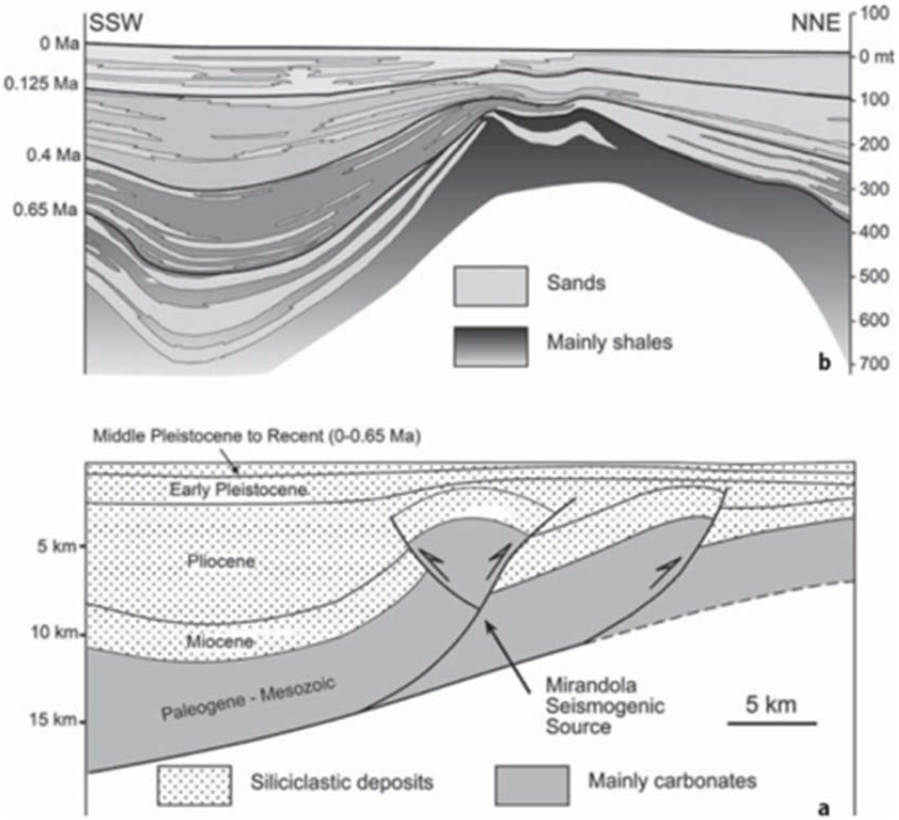

Figure 1.3.1: Cross sections across the Mirandola structure, which lies to the east of the Mirandola fault in the Ferrarese-Romagnolo arc. Structural relief of Late Quaternary strata above the crest of the fold define its recent activity, and were used to constrain fault slip rates. From Scrocca et al. (2007).

Based on our seismic mapping and velocity analysis, the Cavone structure exhibits more than 500 meters of structural relief for the base of the Quaternary section. Assuming a maximum age for the Quaternary section of 2.6 Ma, and given the fault dip of 60°, the slip rate of the

underlying Mirandola fault can be calculated using a simple rigid block translation model. With this approach, 500 m of structural relief for the base Quaternary section implies an uplift rate of 0.2 mm/yr on the Mirandola fault, within the range of uplift rates determined by Scrocca et al. (2007).

In summary, we suggest that the patterns of syntectonic growth strata define the Late Quaternary tectonic activity of the Mirandola fault, which is in agreement with previous analysis of other structures in the region. Late Quaternary activity of faults in the Ferrarese-Romagnolo arc is also consistent with the occurrence of historic earthquakes in this region that pre-date the advent of modern drilling activities (DISS, 2007).

1.4 SEISMOTECTONIC ANALYSIS

The location of the May 29, 2012 M_w 5.8 Northern Italy earthquake and aftershocks relocated as part of this study suggest that the event was sourced by the Mirandola fault (Figure 1.2.2). The relocated aftershocks are clustered between 5 to 10 km along the up-dip extent of the Mirandola fault, its splays, and backthrusts (Figure 1.4.1). The spatial correlation between the earthquakes and the Mirandola fault system is present for hypocenters relocated using both the velocity model provided by the operator of the Mirandola concession and one that we developed from well log data in the oil field. The May 29, 2012 M 5.8 hypocenter located by INGV occurs within about 2 km south of the Mirandola fault when projected into section B-B'. Given the uncertainties in this event location, it seems likely that the mainshock occurred on the Mirandola fault. Moreover, the strike and steep south dip of one of the nodal planes of the INGV focal mechanism is generally consistent with the dip and orientation of the Mirandola fault. Taken together, the general location of the M 5.8 event and its aftershocks, as well as the focal mechanism characteristics, imply that the May 29, 2012 M_w 5.8 earthquake occurred on the Mirandola fault.

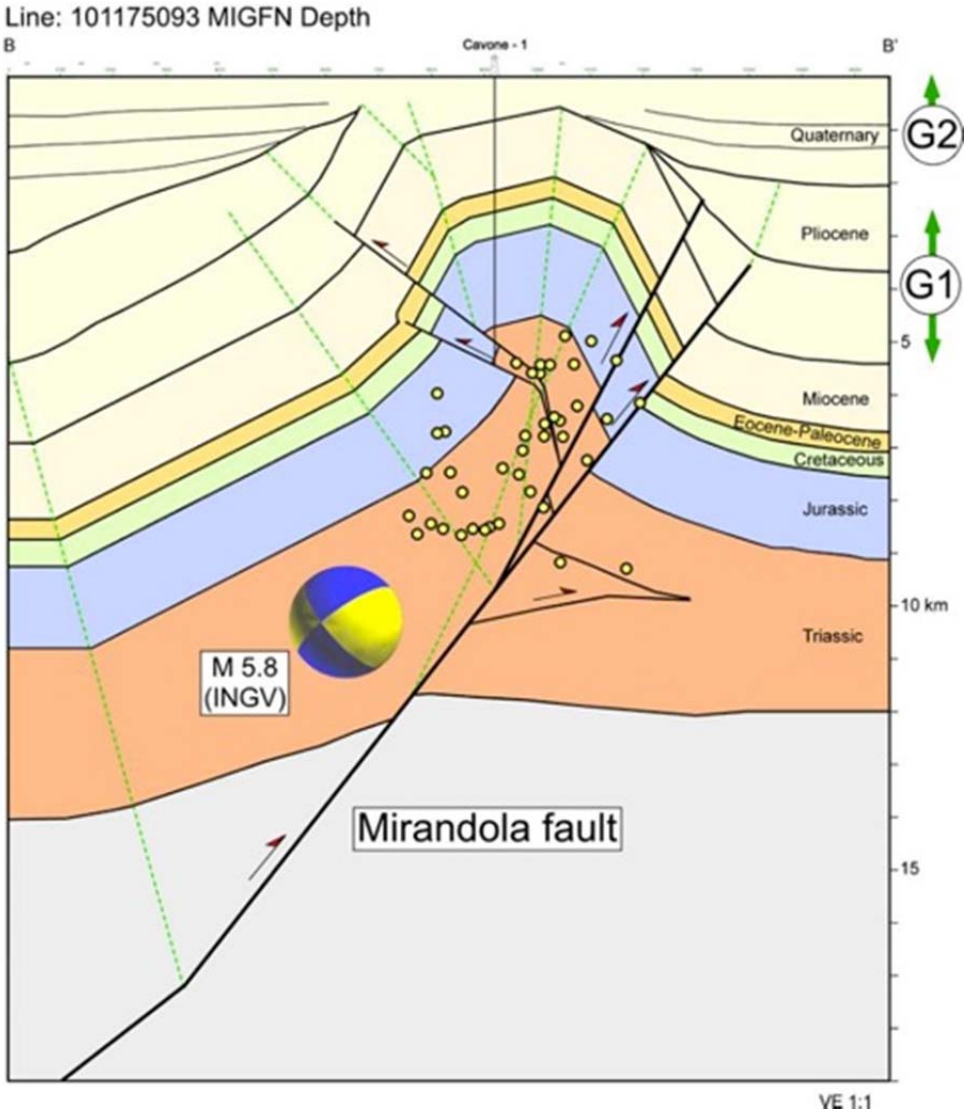

Figure 1.4.1: Geologic section B-B' with location and focal mechanism of the May 29, 2012 M 5.8 earthquake (INGV) and select aftershocks relocated as part of this study (Cavone.01.ENIwVENI.DD.eqs).

The May 20, 2012 M 6.0 Northern Italy earthquake occurred about 10 km to the northeast of the May 29 M 5.8 event (Figure 1.2.2). Based on the event location and mapped fault geometries, it is clear that the M 6.0 event did not occur on the Mirandola fault. Rather, the earthquake appears to have occurred on the western segment of the Middle Ferrara fault (Pezzo et al., 2013), based on its hypocentral depth and aftershock distribution (Figure 1.4.2). The strike and steeply south-dipping nodal plane of the M 6.0 event is also compatible with mapped geometry of the Middle Ferrara fault (Figure 1.3.2). Thus, we conclude that the May 20, 2012 M 6.0 and May 29 M 5.8 events occurred on separate, en echelon blind-thrust faults.

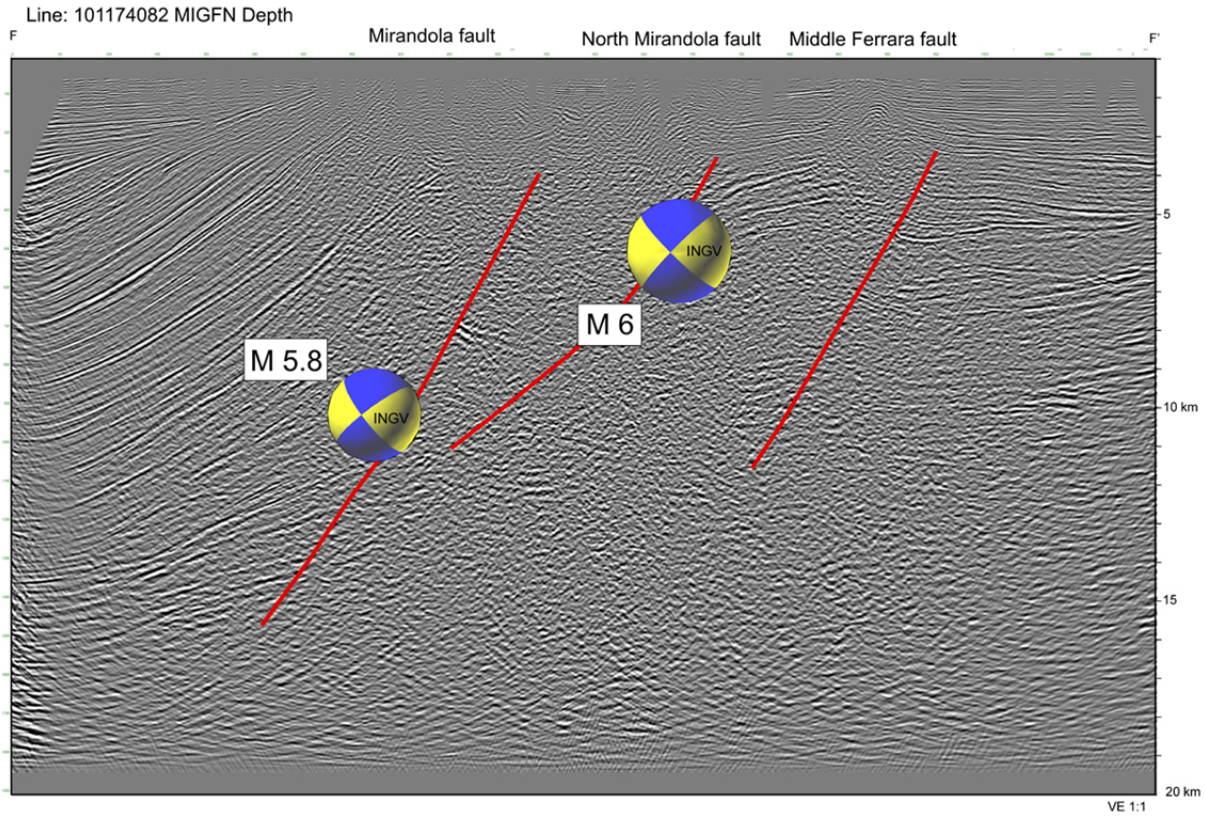

Figure 1.4.2: Migrated and depth converted seismic section F-F' showing locations and focal mechanisms of the 2012 May 20 M 6.0 and May 29 M5.8 earthquakes (INGV).

We analyzed the spatial association of the seismicity recorded by the local Ferrara Municipality network (March 2010 to September 2013) and the major fault systems. Notably, there were no events recorded by the local network prior to the May 20, 2012 (M_w 6.0) earthquake that are located within the Middle Ferrara thrust sheet. After the May 20 earthquake, there is a distribution of events within the Middle Ferrara thrust sheet that extends along strike from the mainshock (Figure 1.2.6). The seismicity data provided by INGV (Cavone.00.ISCall.eqs, January 2011 to February 2013) suggest that the aftershocks of the May 20, 2012 (M_w 6.0) earthquake occur along the entire extent of the western segment of the Middle Ferrara fault. The eastern limit of this aftershock cluster is coincident with the geometric segment boundary of the Middle Ferrara fault that we have identified in our mapping (Figure 1.4.3). This suggests that the May 20, 2012 (M_w 6.0) earthquake and its aftershocks ruptured the western segment of this fault, and that the geometric segment boundary limited the eastern extent of the rupture.

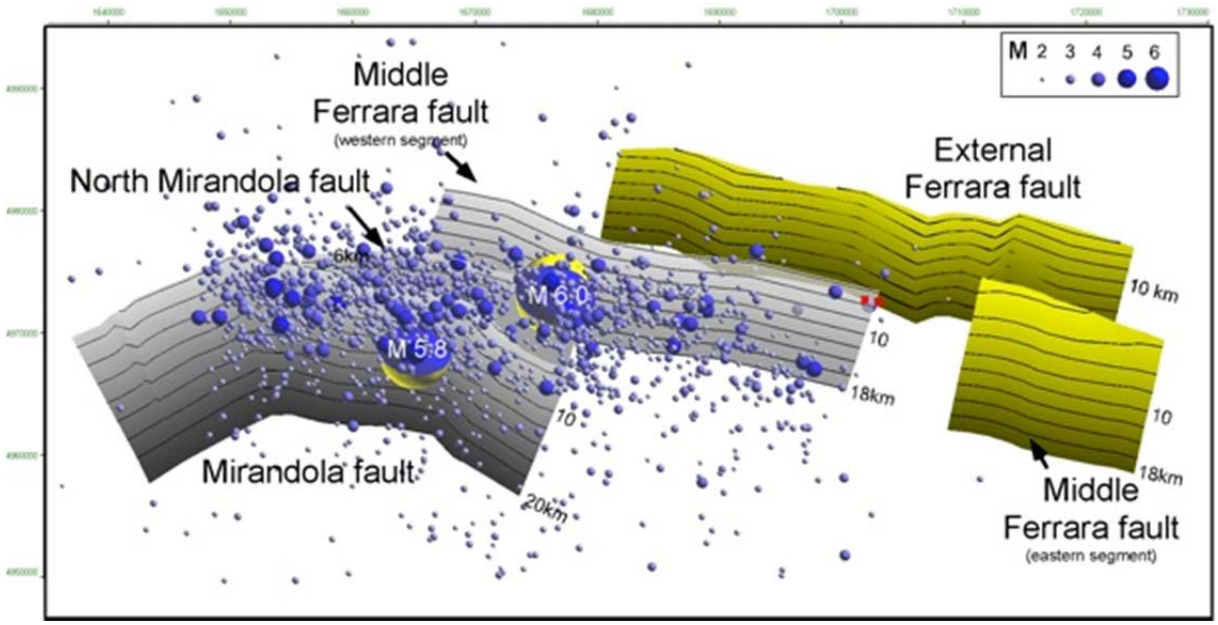

Figure 1.4.3: Base map showing epicenters from the INGV earthquake catalog (Cavone.00.ISCall.eqs, January 2011 to February 2013) relative to the major fault systems in the study area.

The 1570 Ferrara earthquake appears to have ruptured the eastern extent of the Middle Ferrara fault or the External Ferrara fault, based on the hypocentral source region defined by DISS (2007) (Figure 1.2.2). The structure in this region is also imaged by seismic reflection profiles provided by the operators of the Mirandola concession, and consists of a steeply south dipping reverse fault overlain by a north vergent fault-propagation fold (Figure 1.4.4). Similar to the Cavone-Mirandola structure, the Ferrara structure shows evidence for two phases of tectonic activity, one in the Pliocene and a second in the Late Quaternary, based on patterns of syntectonic growth strata. Thus, the structural style of the source regions for the 1570 Ferrara and 2012 Emilia earthquakes are similar (Section 1.1.1). Taken together, these events represent the westward propagation of rupture on a tectonically active, en echelon blind reverse fault system (Figure 1.2.2).

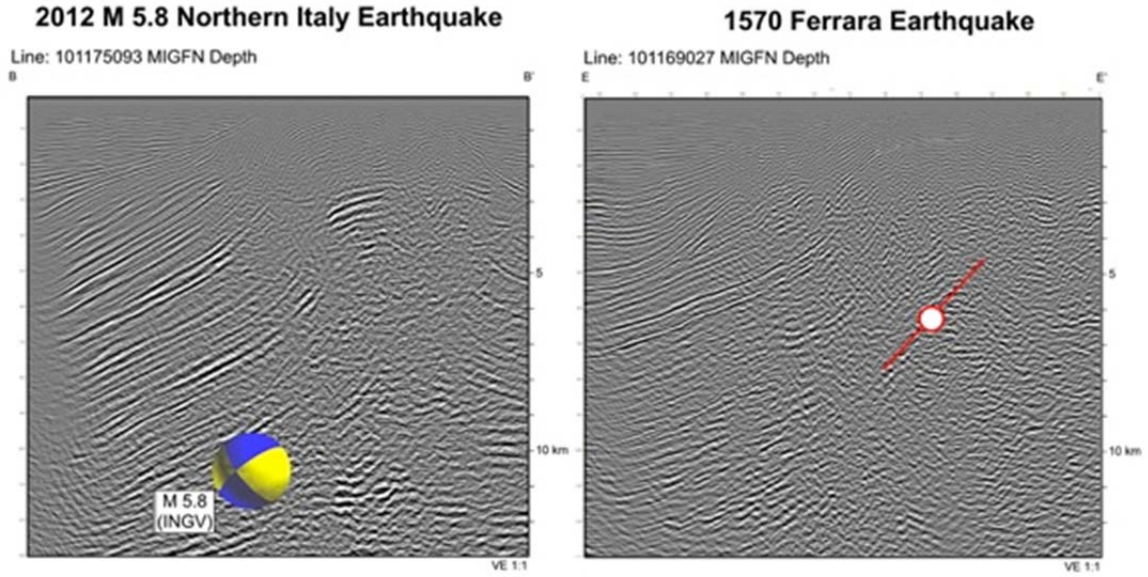

Figure 1.4.4: (left) Migrated and depth converted section B-B' showing source location of the May 29, 2012 M 5.8 earthquake (INGV) (right) Migrated and depth converted section E-E' showing source location of the 1570 Ferrara earthquake inferred by DISS (2007).

1.5 GPS CONSTRAINTS ON TECTONICS — PRE-EARTHQUAKE REGIONAL DEFORMATION RATES

Deformation of the Emilia-Romagna region has been measured using a combination of continuous and campaign GPS since 1991. Serpelloni et al. (2006) analyzed a combination of continuous and campaign data spanning 1991 – 2002 and estimated that there is < 1 mm/yr convergence across the region. Devoti et al. (2011) present a somewhat higher quality velocity field from over 300 continuous GPS stations in Italy for the time interval 1998-2009. Of particular relevance, they present both GPS velocity vectors and velocity magnitudes projected along a cross section just east of the earthquake sequence (Figure 1.5.1), showing about 1 mm/yr convergence within ~50 km of the epicentral region. Figure 1.5.1 shows that the area is undergoing deformation consistent with the entire regional pattern, with no anomalous features localized to the epicentral region.

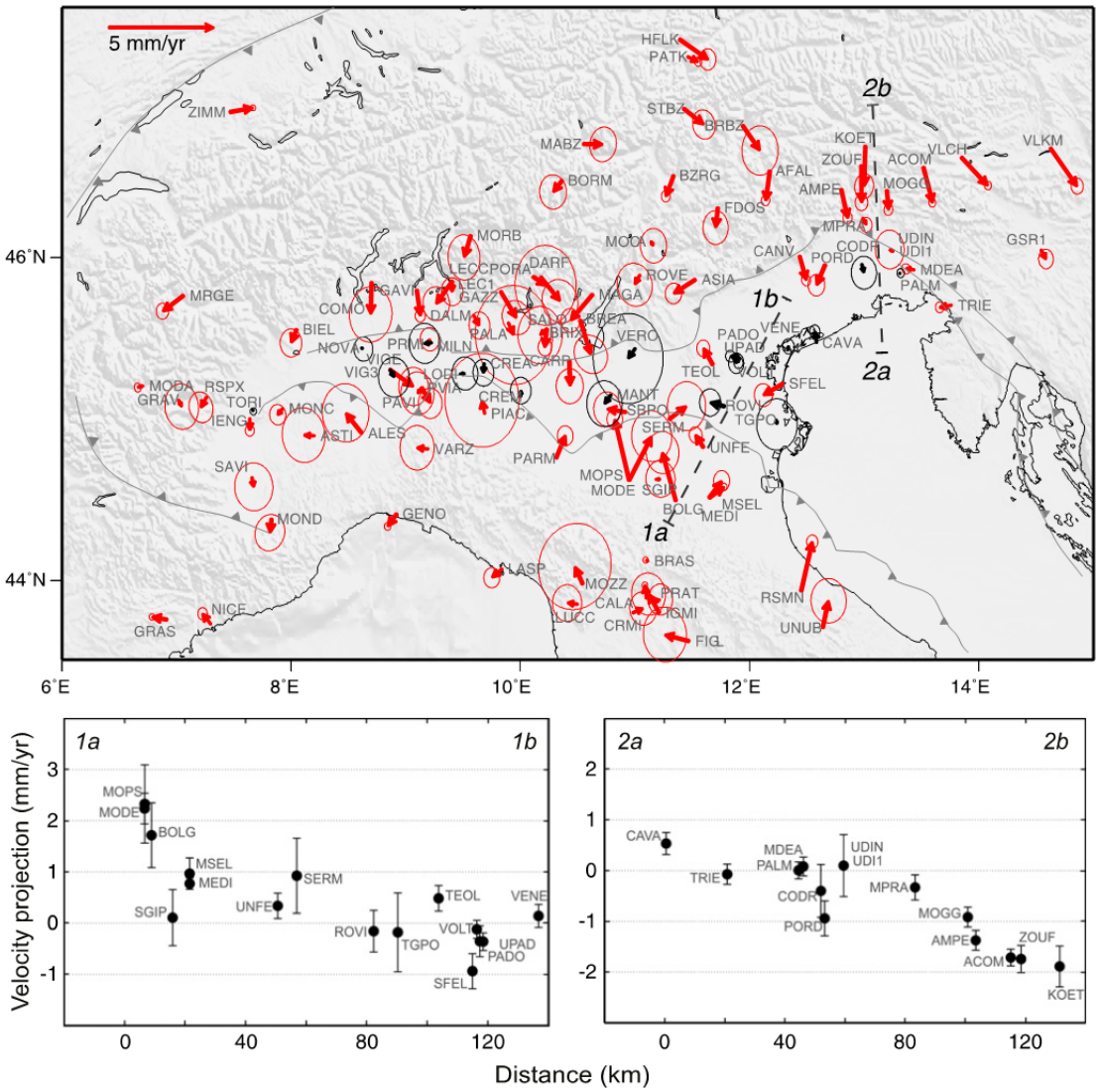

Figure 1.5.1: (Figure 6 of Devoti et al., 2011): Velocity field in northern Italy expressed with respect to a non moving Adriatic microplate defined by sites located in the Po plain (black arrows). Velocity ellipses represent 1-sigma confidence errors. The dashed lines show the traces of the velocity profiles reported on the lower panels.

The ~1 mm/yr deformation measured using GPS over the decadal time scale and the deformation recorded in the geologic record over the 1 Ma time scale are comparable. As discussed in Section 1.3, the geologic (~1 Ma) estimate of the uplift rate on the Cavone structure alone is 0.2 mm/yr, but this is only one of 3 closely spaced structures. The seismic activity shows that at least two, and perhaps all three of these structures are active. Similarly, Scrocca et al. (2007) estimate uplift rates of 0.16 – 0.53 mm/yr on the Mirandola structure.

It is of interest to calculate the rate of seismicity that would be required if all of this convergence were accommodated by earthquakes of the size of the largest events in the

Emilia-Romagna sequence. Estimates of source properties from geodetic data by Pezzo et al. (2013) lead to average coseismic displacements of 340 mm for the 20 May event, and 180 mm for the 29 May events. Maximum displacements are 1280 mm and 550 mm, respectively. Assuming that typical large earthquakes in the region have $M_w \sim 6$, and dividing these displacements by a displacement rate of 1 mm/yr leads to the estimate that, at any given longitude, the average recurrence interval should be hundreds of years. These estimates are commensurate with the historically determined rate of earthquake occurrence in the region.

1.6 CONCLUSIONS OF SEISMOTECTONIC AND GEODETIC ANALYSES

- *Based on the consistency of the mainshock hypocenter, focal mechanism, aftershock distribution, and mapped fault geometry, we conclude that the western segment of the Middle Ferrara fault sourced the May 20, 2012 (M_w 6.0) earthquake. This earthquake is located approximately 20 km from the Cavone wells. Moreover, the May 20 earthquake is separated from the Cavone well by two thrust sheets.*

- *Based on the aftershock distribution, it appears that the eastern limit of rupture for the May 20, 2012 (M_w 6.0) earthquake was controlled by a segment boundary in the Middle Ferrara fault.*

- *The Mirandola fault sourced the May 29, 2012 M 5.8 earthquake. Thus, the May 20 M_w 6.0 and May 29 M 5.8 events occurred on different faults.*

- *The Mirandola fault and adjacent structures show evidence of late Quaternary tectonic activity based on growth strata and deflected stream patterns. Based on patterns of Quaternary growth strata, the Mirandola fault has been active for at least the past 650 ka Scrocca et al. (2007). If all of the structural relief of the Quaternary horizons across the Cavone fold occurred in M 6.0 events, it would require that several thousand such events occurred on the Mirandola fault over the past 650 ka.*

- *The ~1 mm/yr convergence measured using GPS over the decadal time scale and the convergence recorded in the geologic record over the 1 Ma time scale summed across structures are comparable. This agreement suggests that the rate of earthquake activity in this region has been comparable to the current rate for ~ 10^6 years.*

- *The 1570 Ferrara, 2012 M_w 6.0, and 2012 M_w 5.8 earthquakes represent a westward propagating rupture sequence on three distinct, en echelon blind reverse faults in the Ferrarese-Romagnolo arc.*

- *The rate of earthquake activity calculated, given the convergence rate observed with GPS, and assuming that the fault slip and area of the M_w ~ 6 events in the May 2012 sequence are typical, is comparable to the historical rate.*

2. SEISMICITY IN THE EMILIA-ROMAGNA REGION AND THE PO VALLEY

This section summarizes instrumentally-recorded regional seismicity prior to and following the Emilia-Romagna 2012 earthquakes, focusing on activity occurring in the neighborhood of the Cavone well #14, which has been injecting water into the subsurface since 1993. To a certain extent this summary duplicates already-published investigations (e.g., Lavecchia et al., 2012; Scognamiglio et al., 2012). However, the present study also evaluated seismic records and locations using phases recorded at nearby stations operated by the operators in the Cavone oil field, information that has not been published previously.

An important issue concerns the maximum distance from an injection well where it is plausible that earthquake triggering might occur. In the literature describing induced/triggered earthquakes the vast majority are reported at distances less than 5 km from the injection location. However, a few unusual sequences have events located at greater distances; e.g., cross sections in Hsieh and Bredehoeft (1981) and Herrmann et al. (1981) show some Rocky Mountain Arsenal earthquakes at 7 km distance. In Paradox Valley, Colorado, U.S.A., apparently-triggered earthquakes with magnitudes up to M4.4 are situated at distances up to 17 km from the injection well (Ake et al., 2005; Block et al, 2014). In Paradox Valley, injection began in 1991, triggering earthquakes near the well almost immediately. Subsequently there has been a progression of earthquakes at progressively greater distances from the well; in 1995 they occurred at distances as great as 4 km; then 8 km distance by 1998, 12 km by 2001; 16 km by 2002, and 17 km by 2007. Near Jones, Oklahoma, U.S.A., a series of earthquakes 2008-2013 includes events situated at distances as great as 35 km from injection wells (Keranen et al., 2013, 2014). However, the Oklahoma situation is unusual because injection volumes are extraordinarily high, averaging ~500,000 m^3/mo since 2009. Although injection volumes at Cavone #14 have not exceeded 18,000 m^3/mo, and triggering at distances beyond a few km seems highly unlikely, for completeness in this section we will consider seismicity at distances up to 40 km from the injection well.

A second important issue concerns the accuracy of locations reported in catalogs. For background information about regional seismicity since 1964 and the Emilia-Romagna 2012 sequence, we rely on epicenters reported by the International Seismological Centre (ISC). The ISC combines information reported by various different organizations, including INGV, concerning seismicity. Thus for most regions the ISC catalogs and epicenters are as complete and accurate as any source, unless a focused investigation has been undertaken well after events have occurred.

However, often for many events reported in catalogs, both reported focal depths and the locations of events relative to one another are unreliable. Relative locations among clusters of

events are most accurate when events are relocated using a common set of nearby stations surrounding the cluster. Focal depths are most accurate for events where well-recorded readings for both P and S phases are available at stations with a few km of the epicenter. In most regions station coverage varies from year to year and the data quality differs among events.

For these reasons, we have relocated selected earthquakes near Cavone #14 occurring between 2001 and June 2012; these are especially well-recorded events, many recorded by seismograph stations managed by the Operator providing data not available to the ISC. For these events we augmented phases reported by the ISC with data recorded by local stations, when these data were available. For these relocated hypocenters we have credible information about focal depths. In contrast, a significant fraction of the hypocenters reported in the ISC Catalog have depths fixed arbitrarily at zero, 5 km, or 10 km, and there is considerable scatter among the remainder (see Figure 2.1.1).

In addition, we evaluate earthquakes occurring between August 2013 and June 2014 that were recorded by the Operator's network, near or within this network, and located by their seismologists (see Section 2.3). Nearly all of these events had magnitudes of M2.0 or smaller and were not reported by the ISC; however, the epicenters and focal depths obtained by seismologists are credible because these events occurred near and within the local network.

A description of the co-seismic and post-seismic displacements in the region is included in this Section, as well as modeling of the static Coulomb stress changes from the May 20 earthquake to understand its role in triggering the May 29 event.

2.1 REGIONAL SEISMIC ACTIVITY PRIOR TO MAY 2012

Section 1.1 1 described the seismic history of the Po Plain and Emilia-Romagna region, where the most noteworthy earthquake was felt early in the morning on 17 November 1570 causing the collapse of many balconies and chimneys in Ferrara with an estimated magnitude Me 5.5. The extent of the felt area for this event is similar to that reported for the May 20th, 2012 earthquake (see Figures 1.1.3 and 1.1.4).

Other regional historical events include earthquakes in 1411 (Me 5.1) and 1346 (Me 4.9), also listed as occurring near the city of Ferrara. Eastward of Ferrara three earthquakes occurred, two in 1922 (Me 3.7, 2.9) and the 1931 (Me 4.8) in the Ferrarense region. To the west of Ferrara, i.e. toward the location of the Emilia-Romagna May 2012 earthquake sequence, several earthquakes are reported: near the town of Cento in 1916 (Me 3.7), further west near Finale Emilia two events in 1908 (Me 4.3) and more recently in 1963 (Me 4.1) occurring within 10 km of the M_w 6.0 May 20, 2012 epicenter. Earthquakes in 1910 (Me 3.9) and 1912 (Me 3.2) near Mirandola occurred within 10 km of the May 20 and within 5 km of the May

29, 2012 epicenters. In addition, a review of the historical seismicity in the region by Castelli et al. (2012) identified an event occurred near the town of Mirandola in 1761 for which no estimated magnitude is given.

Instrumentally recorded earthquakes in the region surrounding Cavone well #14 are also numerous; between 1964 and April 2012 the International Seismological Centre (ISC) reports more than 1200 epicenters having magnitudes M 2.5 or greater within the region mapped in Figure 2.1.1. Most of the events within 40 km of Cavone well #14 (Figure 2.1.2) are aftershocks of two events. One was the M4.7 2 May 1987 earthquake, which occurred well before injection commenced at Cavone well #14; the other was the M5.3 15 October 1996 earthquake; one occurred about 30 km southeast, and other 20 km southwest, of Cavone well #14. The 1987 earthquake had no foreshocks reported in the month prior to its occurrence; none of its aftershocks were closer than 7 km from Cavone well #14. Similarly, the 1996 earthquake did not have foreshocks, and only a few small aftershocks were located within 10 km distance.

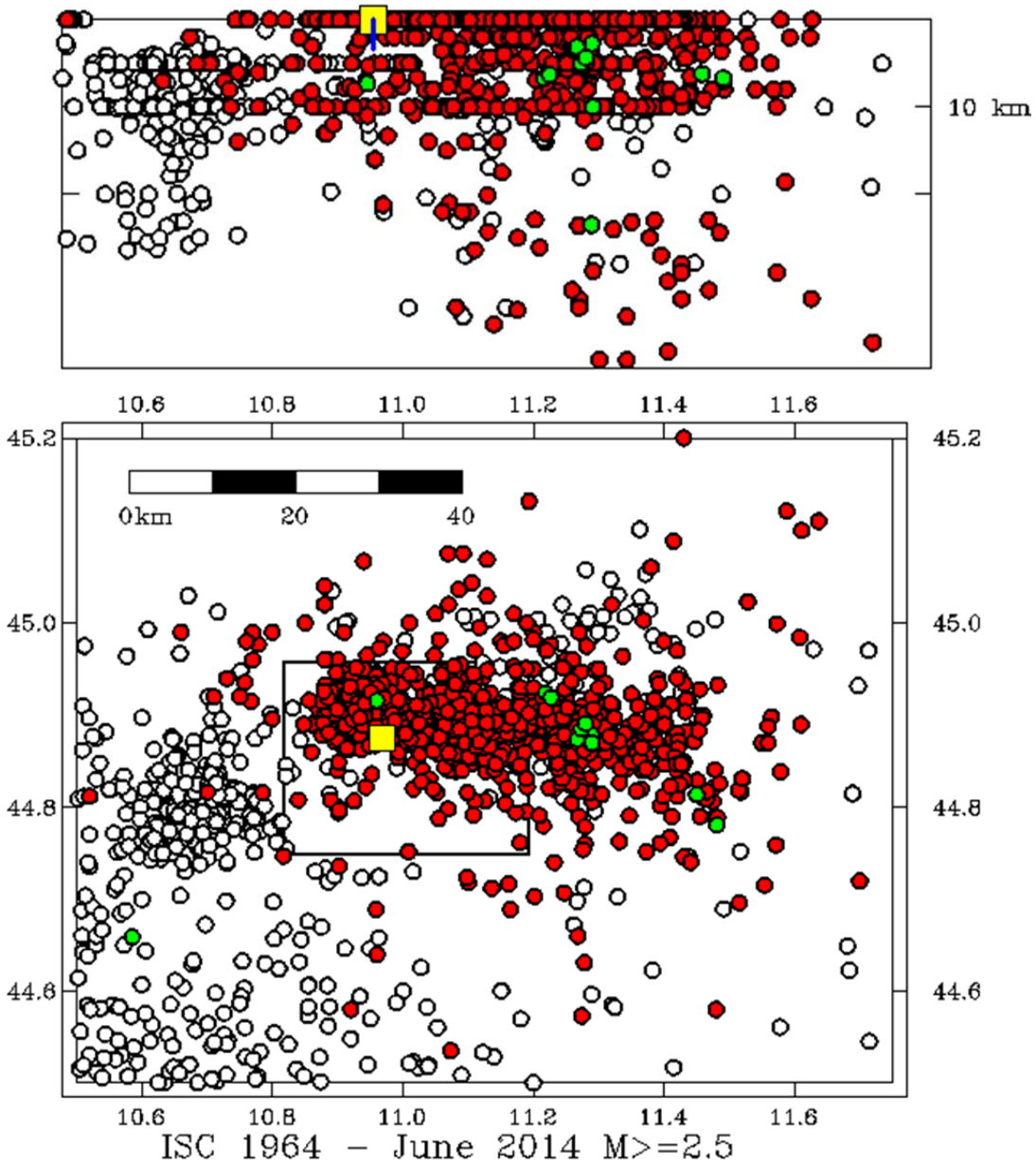

Figure 2.1.1: Map and east-west cross section of earthquakes (circles) having magnitudes of M2.5 and larger occurring between 1964 and June 2014 as reported by the International Seismological Centre (ISC). White circles: earthquakes 1964 – April 2012; red circles: earthquakes May-June 2012; green circles: earthquakes July 2012 – June 2014. Yellow square is Cavone well #14. Rectangle indicates area included in Figure 4.2.1. Cross section only includes locations between 44.7°N and 45.1°N.

The number of seismograph stations near Cavone well #14 has changed considerably between 1964 and the present time. The lack of nearby stations undoubtedly explains why there are almost no catalogued earthquakes having M<4 reported prior to 1976. Subsequently in the 1980's, regional stations were installed; in 2005 INGV made modifications to the regional

network, and undoubtedly many earthquakes having magnitudes of M2.5 and smaller have been detected and catalogued, whereas many similar events would not have been reported previously.

In addition, there have been seismographs operating near the Cavone field, although not continuously, beginning as early as 1980. Between 2000 and June 2012 several seismic stations were in operation at various locations within the Cavone oil field. Numerous events have been located, often supplementing field dedicated-station data with seismograms from regional INGV stations. There were network problems following the 2012 earthquakes and no useful data is available between mid-June 2012 and July 2013. Between August 2013 and the present there have been four local seismograph stations recording earthquakes occurring near Cavone well #14; we discuss locations determined using these data in Section 2.3.

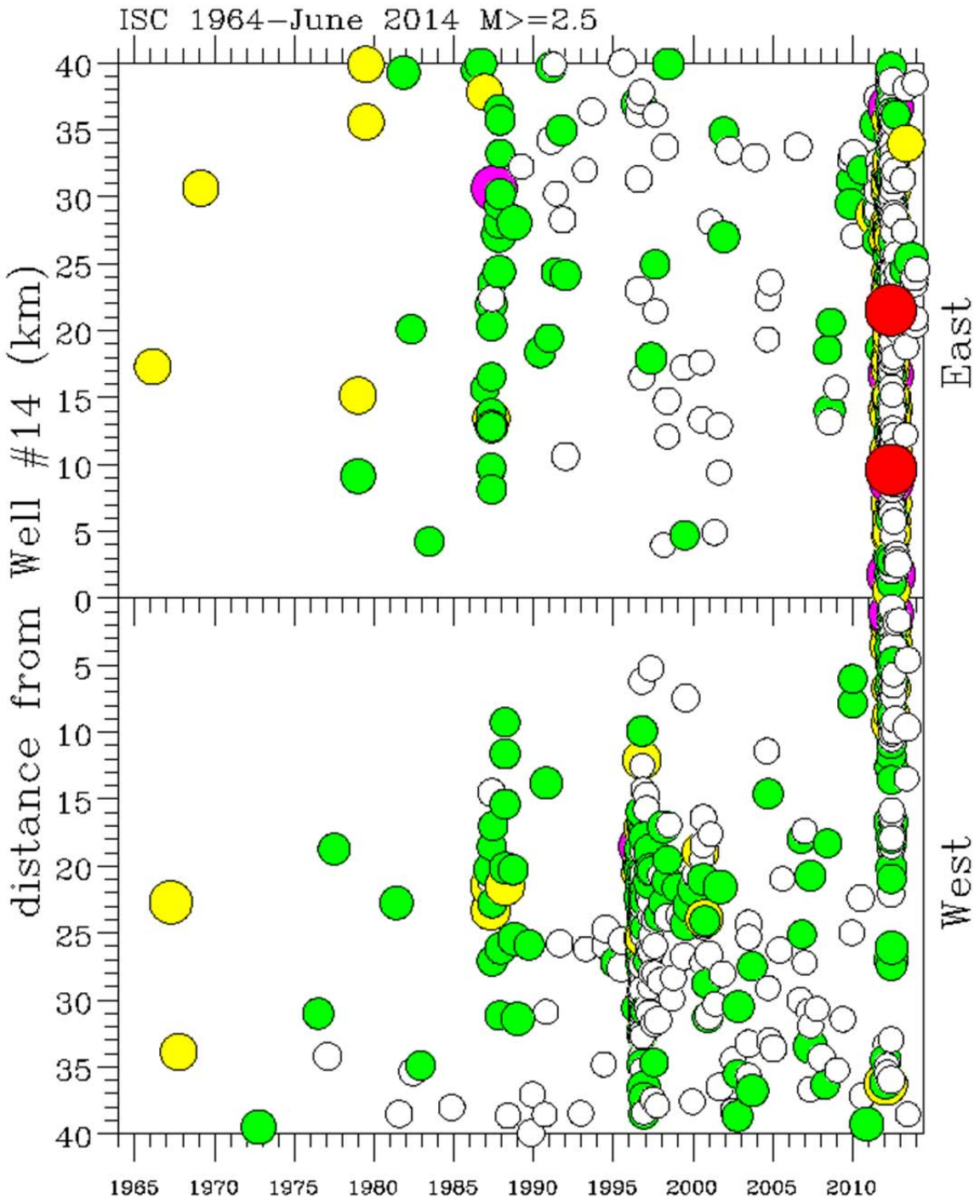

Figure 2.1.2: Space-time plot of ISC-reported epicenters (circles; earthquakes with magnitudes of 2.5 and larger as in Figure 2.1.1) occurring between 1964 - June 2014. Vertical axis shows distance between epicenters and Cavone well #14; upper part of plot shows earthquakes east of well; lower part shows earthquakes west of well. Colors/sizes indicate reported magnitudes; white: M<3; green: 3 < M < 4; yellow: 4<M<5; pink: M>5; red: 20 May and 29 May 2012 largest earthquakes.

The number of ISC-catalogued earthquakes having M<3 in this region increased significantly in the 1980's, reflecting the installations of regional network stations by INGV. Inspection of the ISC-reported phase arrivals for earthquakes reported within 10 km of Cavone well #14 (including some with M < 2.5; see Figure 2.1.3) indicates that many do not have well-determined epicenters and most have unreliable focal depths (i.e. their locations were determined using phase arrival information from two or fewer stations within a distance of 100 km).

Because the routine locations reported by the ISC and INGV are sometimes unreliable, we have relocated a select group of events near Cavone well #14 (Figures 2.1.4 and 2.1.5). The phase data used for these relocations are a combination of P and S arrivals reported by the ISC, supplemented by P and S arrivals recorded at four stations (station codes ROCE, SGIA, ROVE and CORR) operated privately in the Cavone area. The Operator provided phase arrivals for 126 earthquakes occurring 2000-2012; of these 67 occurred between 2001 and 2011, and 59 occurred in May or June 2012 during the Emilia-Romagna sequence. Of the 2001-2011 earthquakes, 28 satisfied the requirement that the largest epicenter-to-station azimuthal gap among the recording stations was 200° or less. Essentially, these requirements constrain the location process, minimize systematic errors caused by incorrect assumptions about heterogeneities in the regional crustal structure, and make it possible to obtain credible epicenters and focal depths. . To determine the relocated epicenters we used the so-called double-difference location method (Waldhauser and Ellsworth, 2000). The double-difference method is designed to obtain very accurate relative locations among a group of events from a restricted geographical area. By comparing the relative arrival times at individual stations for nearby events, it is able to minimize problems caused by errors or blunders in phase readings, and by the absence of readings at particular stations, even if the assumed crustal velocity model is inaccurate or if crustal velocity is heterogeneous. The resolution of the resulting locations generally is superior for identifying clusters, lineations or planar groups of earthquakes.

The majority of the 28 relocated hypocenters (green circles in Figures 2.1.4 and 2.1.5) that occurred years prior to the Emilia-Romagna 2012 sequence are within about 8 km of Cavone well #14. The proximity to the well is unsurprising since the selection procedure (i.e., selecting events recorded by local stations) favors activity in or near the Cavone field. The focal depths range between 4.6 km and 10.3 km. In the approximately west-facing cross section (Figure 2.1.5 bottom), they appear situated along a southward-dipping plane that is roughly coincident with one nodal plane of the 20 May 2012 earthquake. All but two of the relocated earthquakes occurred in the years 2004-2009.

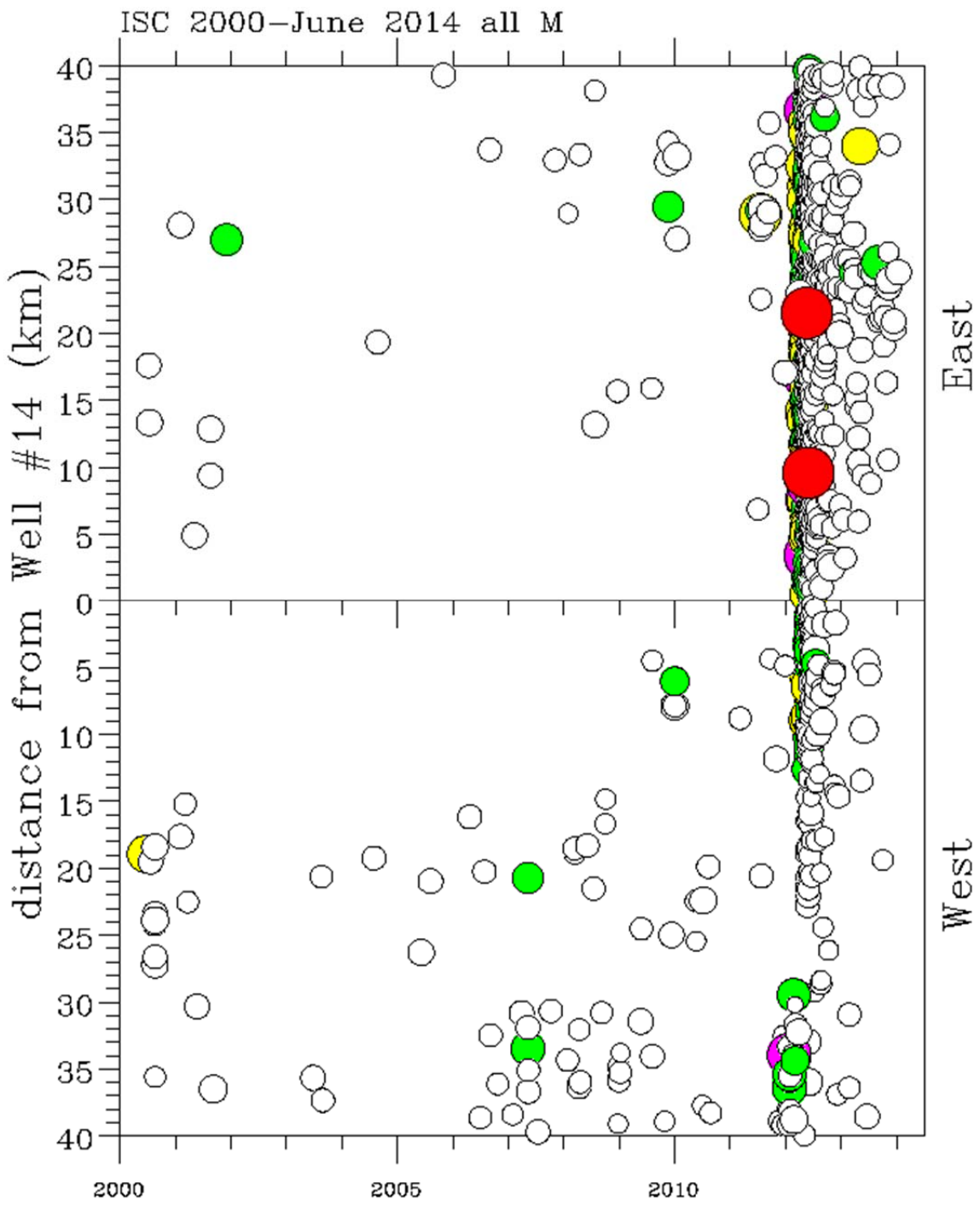

Figure 2.1.3: Space-time plot of all ISC-reported epicenters (circles; plot includes events with M < 2.5) occurring between 2000 and June 2014. Vertical axis shows distance between epicenters and Cavone well #14; upper part of plot shows earthquakes east of well; lower part shows earthquakes west of well. Colors/sizes indicate reported magnitudes; white: M<3; green: 3 < M < 4; yellow: 4<M<5; pink: M>5; red: 20 May and 29 May 2012 largest earthquakes.

Table 2.1.1: ISC locations for significant earthquakes discussed in this report occurring prior to and during the 2012 Emilia-Romagna sequence.

Date	***Origin time***	***Latitude °N***	***Longitude °E***	***Depth (km)***	***Magnitude***	***Distance from Cavone#14***	***Agency***
02 May 1987	2042	44.8082	10.7124	14.1	m_b 4.7	22 km	ISC
15 Oct 1996	095	44.7740	10.7811	6.7	m_b5.3	19 km	ISC
18 May 2012	1940	44.9027	11.2094	-	m_b2.9	19 km	ISC
19 May 2012	1709	44.8946	11.2215	-	m_b2.5	20 km	ISC
19 May 2012	2313	44.9054	11.2046	-	m_b4.2	19km	ISC
19 May 2012	2342	44.9014	11.2271	-	m_b2.2	21 km	ISC
20 May 2012	0203	44.9000	11.2400	10.0	M_W6.0	22 km	ISC
29 May 2012	0700	44.851	11.086	10.2	M_W5.8	10 km	ISC

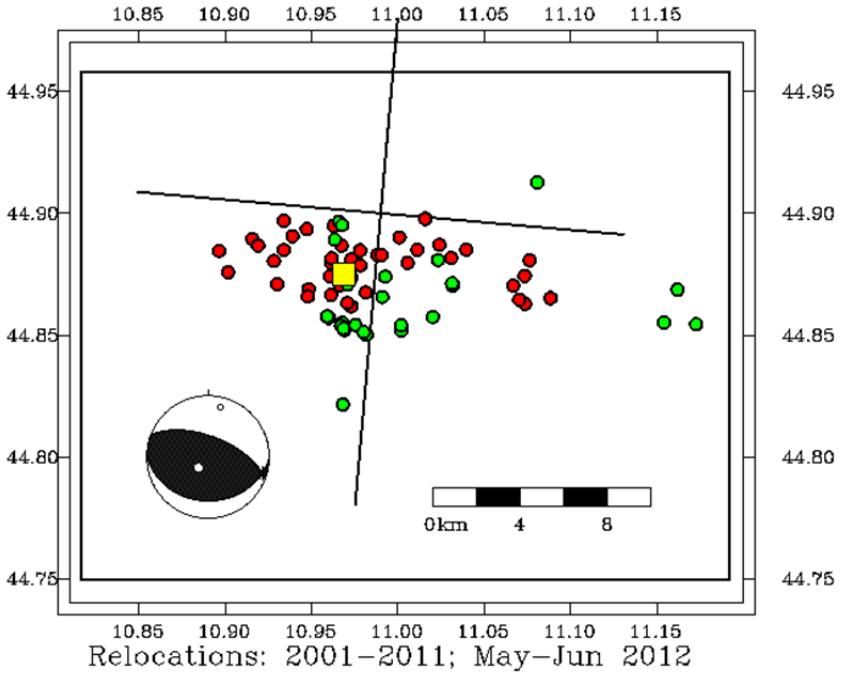

Figure 2.1.4: Map of relocations for selected earthquakes (circles) around Cavone well #14 (yellow square). Green circles: 28 events occurring 2001 to 2011; red circles: 41 events occurring May-June 2012. Plotted focal mechanism for 20 May 2012 earthquake is from theGlobal GCMT catalog. Thick crossed lines indicate orientations of cross sections shown in Figures 2.1.5. Thick lines forming a rectangle indicates the region mapped in Figure 4.2.1.

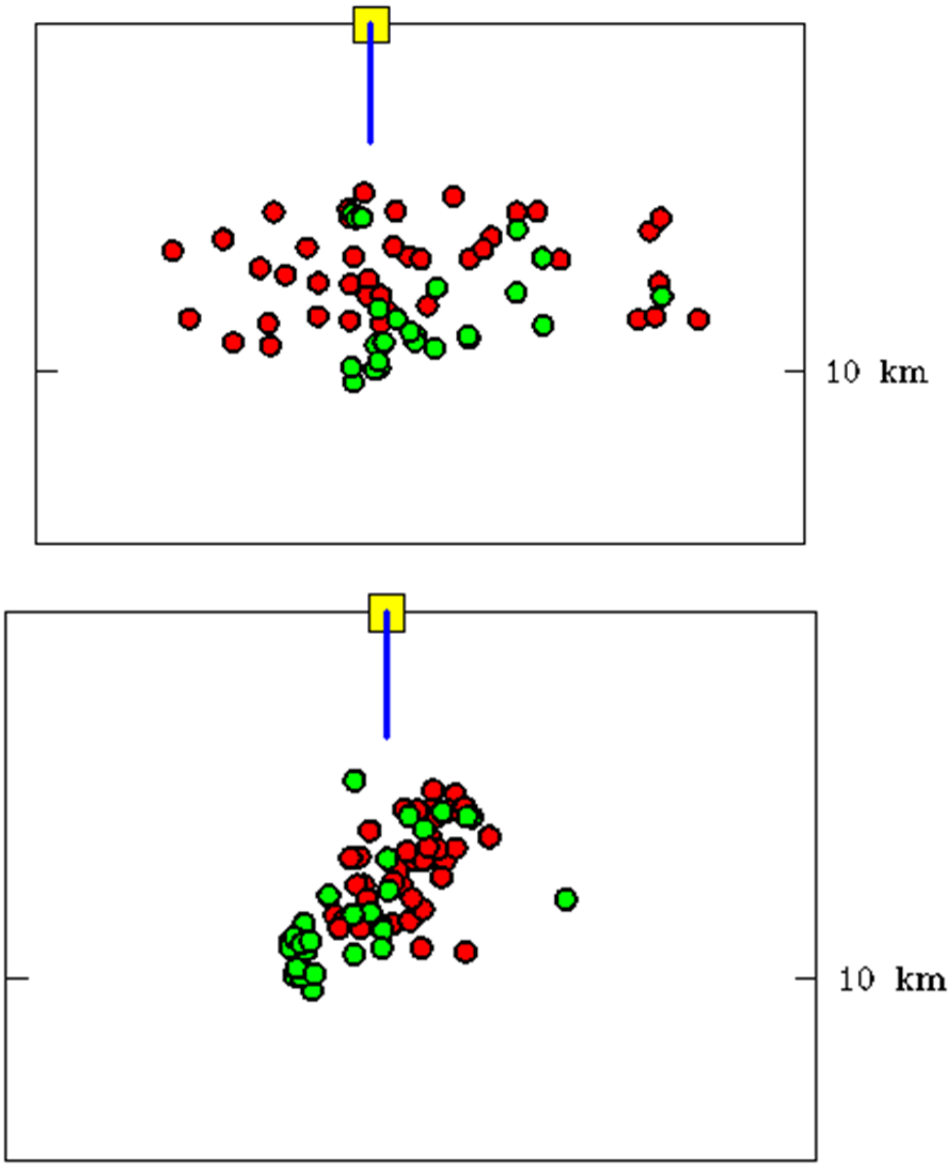

Figure 2.1.5. Cross sections for selected relocated earthquakes (circles) around Cavone well #14 (yellow square and blue line). Green circles: 28 events occurring 2001 to 2011; red circles: 41 events occurring May-June 2012. Note that hypocentral depths for both groups range mostly between 5 km and 10 km.

2.2 THE MAY 2012 EMILIA-ROMAGNA SEQUENCE: ISC LOCATIONS

The Emilia-Romagna earthquake sequence has properties of a cascading series of foreshocks and aftershocks common with tectonic earthquakes. It began with a m_b 2.9 event on May 18. This event was followed on May 19 by three earthquakes with m_b of 2.5, 4.2, and 2.2 respectively. The two principal events in the May 2012 Emilia-Romagna sequence had magnitudes M_W of 6.0 and 5.8 respectively, and occurred 20 May 2012 and 29 May 2012 (Table 2.1.1). Source modeling of the May 20 and 29 events by Cesca et al., (2012) and Piccinini et al., (2012) indicate a complex source for the May 20 earthquake and possible static triggering of the May 29 event (Ganas et al., 2012,).

The 20 May M_W 6.0 event occurred at 0203 with an epicentral distance less than 3 km from the 19 May m_b 4.2 foreshock and about 22 km from Cavone well #14. This event triggered a vigorous aftershock sequence (Figure 2.3.1) with numerous epicenters clustered east of the well at distances of ~8-25 km (Figure 2.3.2). During the 20-28 May time period virtually all the activity remained more than 8 km from the well.

The second M_W 5.8 earthquake sequence occurred at 0700 29 May 2012 (Figures 2.2.1 and 2.2.2), beginning about 10 km east of well #14. The ISC-reported aftershock locations included numerous events near Cavone well #14. There were also numerous events towards the east that appear to be continuing aftershocks of the 20 May event. After 29 May aftershocks extended westward up to 10-15 km from the well. In addition, there were several earthquakes with magnitudes between 3 and 4 at distances 15-30 km west of the well.

As discussed in Section 2.1, to obtain accurate locations and credible (i.e. reliable) focal depths, we relocated 41 selected earthquakes in the May-June 2012 sequence (red circles in Figures 2.1.4 and 2.1.5). The phase data used for these are a combination of P and S arrivals reported by the ISC, supplemented by data recorded at the four localCavone stations. The selected events all were recorded by stations surrounding their epicenters such that no azimuthal gaps exceeded 120°. The relocated hypocenters occupy an approximately 15-km long planar east-west region situated beneath Cavone well #14. Focal depths ranged from 4.8 to 9.6 km.

Table 2.2.1 lists all earthquakes with $M \geq 4.0$ that occurred during May and June of 2012 in the Emilia-Romagna region. Locations and magnitude estimates, given by different agencies are listed in this table. For events with several locations or magnitude estimates our preferred solution has been indicated with ***bold italic*** font. For moderate size events such as these, moment tensor solutions from regional recordings (rCMT) provide better centroid depth estimates than those obtained with recordings from stations located around the globe (gCMT).

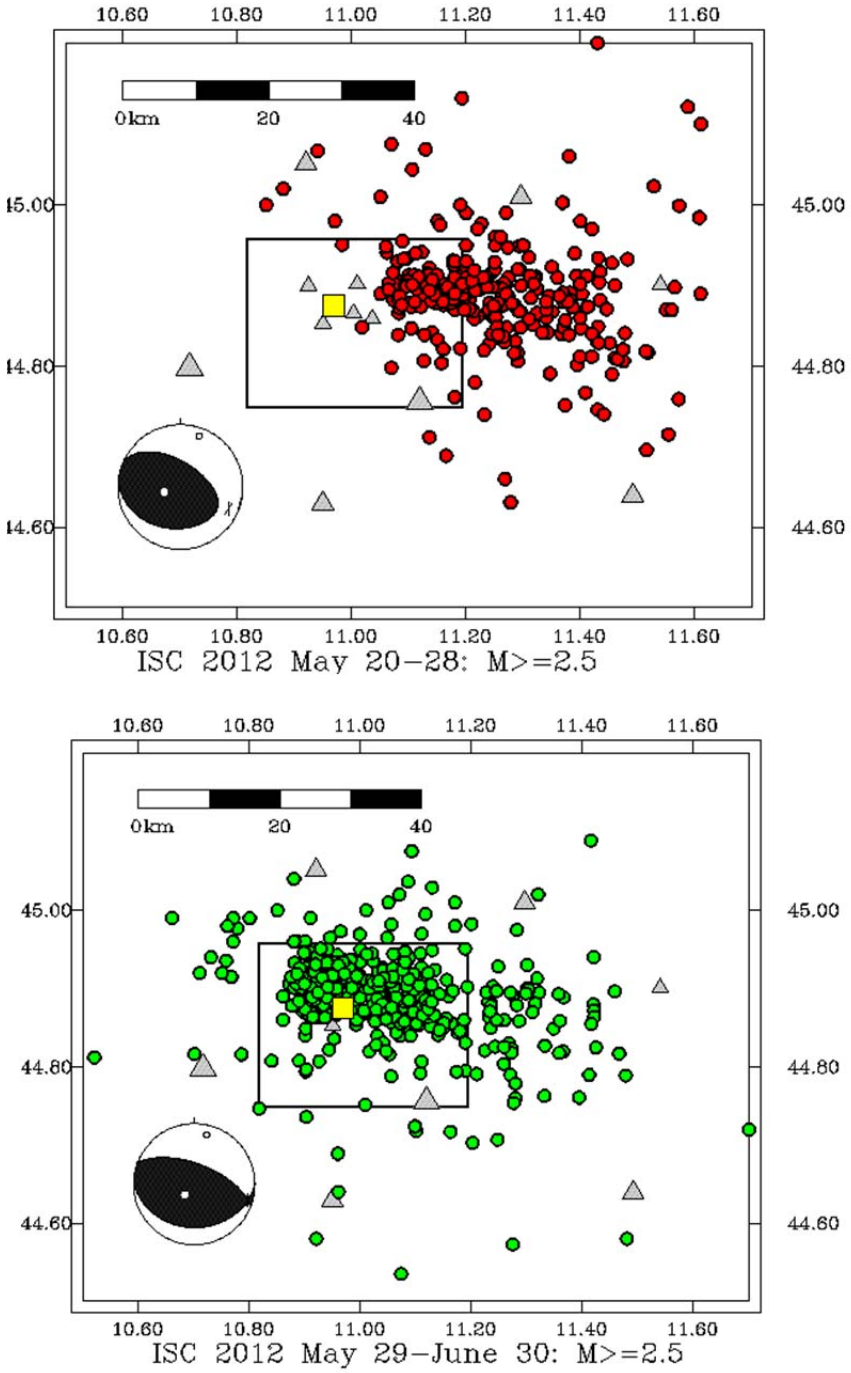

Figure 2.2.1. Maps with epicenters and aftershocks of large earthquakes occurring 20-28 May 2012 0203 (top: red circles) and 29 May-30 June 2012 (bottom: green circles). Plotted epicenters have magnitudes of M2.5 and larger and are as reported by the ISC. Yellow square is Cavone well #14. Triangles are seismograph stations. Rectangle indicates region of the geomechanical model shown in Figure 4.2.1. Plotted focal mechanisms for both events are from the Global GCMT catalog.

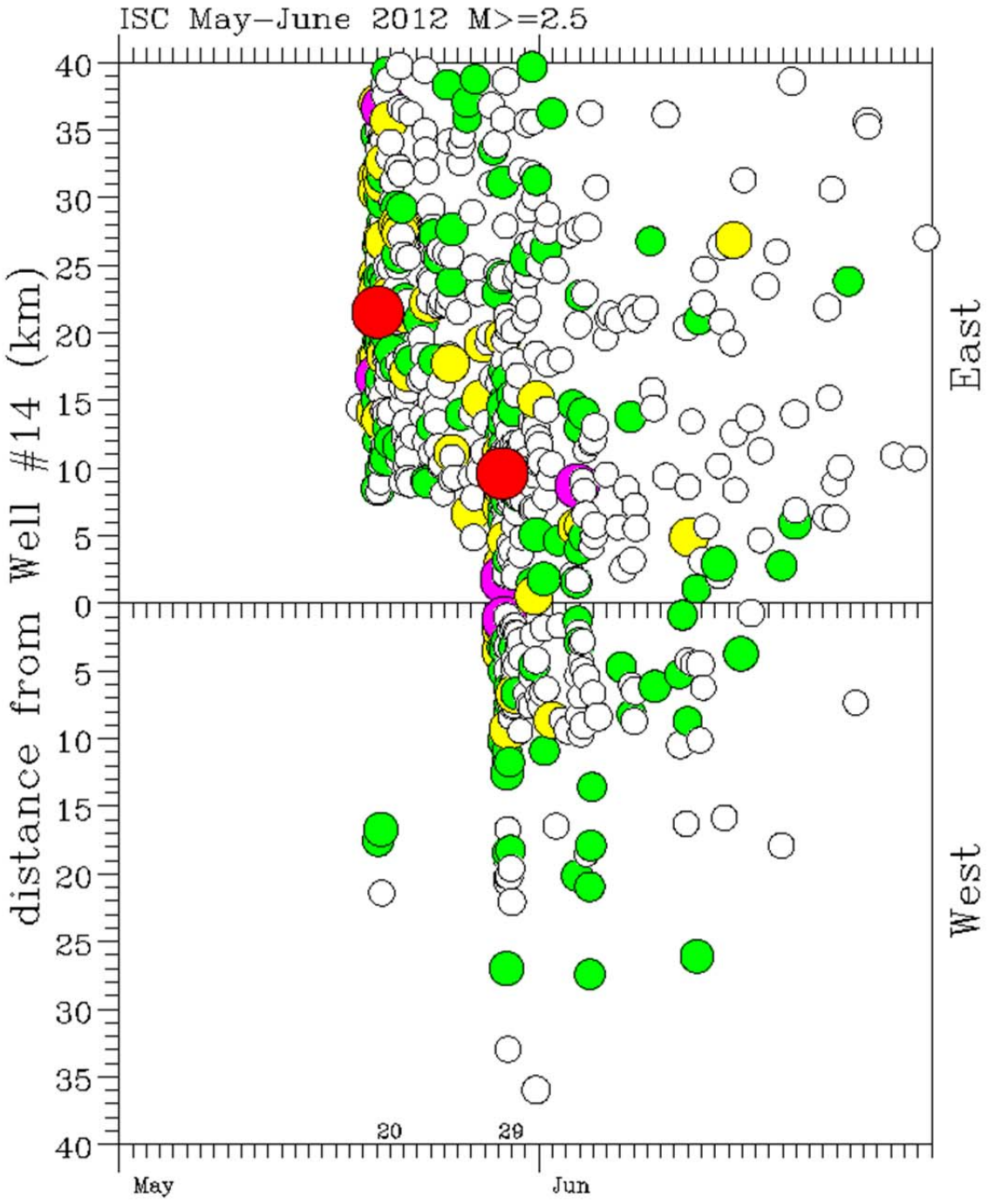

Figure 2.2.2: Space-time plot of ISC-reported epicenters (circles; plot includes events with M < 2.5) in May-June 2012. Vertical axis shows distance between epicenters and Cavone well #14; upper part of plot shows earthquakes east of well; lower part shows earthquakes west of well. Colors/sizes indicate reported magnitudes; white: M<3; green: 3 < M < 4; yellow: 4<M<5; pink: M>5; red: 20 May and 29 May 2012 largest earthquakes.

Table 2.2.1: Earthquakes with M ≥ 4 occurred in the Emilia-Romagna region during May-June 2012

Location (hypocenter / centroid)							**Moment Tensor Solution**			
					Magnitudes			Nodal Plane 1	Nodal Plane 2	**Author**
2012/ **M/D**	HH:MM:SS.	Lat. N	Lon. E	Depth	Ml	**M best/ *Mw***	Mw	Strike/Dip/Rake	Strike/Dip/Rake	
01/25	***08:06:37.09***	***44.871***	***10.510***	***29.0***	***5.0***					INGV-bollsi
				33.0			4.91	76/63/-120	307/40/-46	rCMT-INGV
	08:06:36	44.854	10.538	26.0			4.81	82/80/-118	335/30/-20	rCMT-SLU
05/19	***23:13:27.00***	***44.898***	***11.258***	***6.2***	4.1					INGV-sisbas
						4.0	3.98	84/44/78	280/47/101	rCMT-INGV
				5.0			3.96	100/40/90	280/50/90	rCMT-SLU
05/20	***02:03:52.00***	***44.889***	***11.228***	**6.3**	5.9					ROM
				5.0			5.85	103/46/93	279/45/87	rCMT-INGV
				5.0		***6.0***	5.94	105/45/95	278/45/85	rCMT-SLU
	02:03:56.2	44.89	11.44	12.0 – fix			6.1	88/35/60	304/61/109	gCMT-usgs
05/20	***02:06:30.00***	***44.886***	***11.189***	***7.7***	***4.8***					INGV-sisbas
05/20	***02:07:31.00***	***44.883***	***11.370***	***5.0***	***5.1***					INGV-sisbas
05/20	***03:02:50.00***	***44.860***	***11.095***	***10.0***	4.9					INGV-sisbas
				5.0		***4.8***	4.85	88/27/81	279/64/95	rCMT-INGV
				5.0			4.82	105/40/100	272/51/82	rCMT-SLU
	03:02:51.1	44.95	11.32	12.0 – fix			5.1	94/22/49	316/74/105	gCMT-usgs
05/20	***13:18:02.00***	***44.831***	***11.490***	**4.7**	5.1					INGV-sisbas
				5.0	5.0	***5.0***	4.96	111/41/90	290/50/85	rCMT-INGV
				5.0			4.97	118/40/96	290/50/85	rCMT-SLU
	13:18:04.1	44.81	11.49	12.0 – fix			5.1	100/32/66	308/61/104	gCMT-usgs
05/23	**21:41:18.00**	**44.868**	**11.251**	***4.8***	4.3					INGV-sisbas
				6.0		***3.9***	3.88	91/48/88	274/42/92	rCMT-INGV

				6.0			3.92	97/45/95	270/45/85	rCMT- SLU
05/29	***07:00:03.00***	***44.851***	***11.086***	***10.2***	5.8	***5.8***				INGV-sisbas
	07:00:06.9	44.92	11.15	12.0 – fix			5.9	91/29/72	291/63/99	gCMT-usgs
05/29	***07:09:54.00***	***44.926***	***11.036***	***10.4***	***4.1***					INGV-sisbas
05/29	***08:25:51.00***	***44.901***	***10.943***	***3.2***	***4.5***					INGV-sisbas
05/29	***08:27:23.00***	***44.854***	***11.106***	***10.0***	***4.7***					INGV-sisbas
05/29	***08:40:58.00***	***44.892***	***10.962***	***5.3***	***4.2***					INGV-sisbas
05/29	***09:30:21.00***	***44.892***	***11.053***	***1.2***	***4.2***					INGV-sisbas
05/29	***10:55:57.00***	***44.888***	***11.008***	***6.8***	5.3	***5.4***				INGV-sisbas
	10:55:58.8	44.90	11.02	12.0-fix			5.5	91/29/72	291/63/99	gCMT-usgs
05/29	***11:00:02.00***	***44.873***	***10.950***	***11.0***	***4.9***					INGV-sisbas
05/29	***11:00:25.00***	***44.879***	***10.947***	***5.4***	5.2					INGV-sisbas
	11:00:26.7	44.84	10.95	12.0-fix		***4.9***	4.9			gCMT-usgs
05/31	***19:04:04.00***	***44.891***	***10.980***	***8.7***	***4.2***					INGV-sisbas
06/03	***19:20:43.00***	***44.899***	***10.943***	***9.2***	5.1					INGV-sisbas
	19:20:47.7	45.12	10.95	12.0 – fix		***5.0***	5.0	107/11/99	278/79/88	gCMT-usgs
06/04	***06:55:49.00***	***44.926***	***10.980***	***5.0***	***4.0***					INGV-sisbas
06/12	***01:48:36.00***	***44.880***	***10.888***	***10.8***	***4.3***					INGV-sisbas

INGV – Instituto National Geophysics and Volcanology, Italy; sisbas – Sienna Seismological Institute

bolsi – Bologna Seismological Institute

USGS - United States Geological Survey; gCMT – Global Cetroid Moment Tensor

SLU – Saint Louis University, Missouri; rCMT- Regional Centroid Moment Tensor

2.3 REGIONAL SEISMIC ACTIVITY JUNE 2012 – JUNE 2014

Since May 2012 aftershocks of the 20 May and 29 May 2012 earthquakes have continued into 2013 and 2014 (Figure 2.3.1). The frequency of reported earthquakes between June 2012 and June 2013 was significantly higher than between 2005 and 2011 (Figure 2.1.3). However, as is typical of aftershock sequences, the rates of seismic activity have been declining since June 2012 (e.g. Figure 2.5.5). The duration of an aftershock sequences is controlled by tectonic stressing rates (Dieterich 1994, Toda et al., 2002), wherein lower stressing rates result in longer duration aftershock sequences. Based on a plausible recurrence time of ~1000 years for large thrust events at any given longitude along the Ferrarese-Romagnolo arc (Section 1.5) and the aftershock duration relation of Dieterich (1994), the aftershocks to the May 2012 earthquake are expected to continue for several decades,, but at greatly decreased rates. As aftershock rate decreases, so too does the probability of large aftershocks. However, there is a small, but finite, possibility of large aftershocks. In 2013 and 2014 none of the ISC-reported events within 20 km of well had magnitudes larger than M3, and since July 2013 no ISC-reported events occurred within 10 km of Cavone well #14.

For the time period between August 2013 and June 2014, the best information about seismicity near the Cavone well comes from locations by Operator's seismologists using data collected by the field-operated network (Figures 2.3.4, 2.3.5, 2.3.6 and 2.3.7). Between July 2012 and July 2013 the Cavone network did not collect useful data , but the network was repaired and has been operating since August 2013.

Between 10 August 2013 and 20 June 2014, 75 hypocenters have been located using the local-network data. All but nine of these earthquakes had magnitudes of M2 or smaller; all but one had magnitudes smaller than M2.6. The exception was an earthquake occurring 19 June 2014 and assigned M3.4 by Operator's seismologists (44.8702°N, 11.0247°E, 14 km depth); although the ISC has reported a preliminary location for this event (44.92°N, 11.28°E, no depth assigned), the ISC location was ~20 km east of the Operator's location, well outside of the boundaries mapped in Figure 2.3.4.

The majority of the local network reported hypocenters had focal depths between about 4 km and 10 km, and most form an elongated cluster (Figure 2.3.5, bottom) that is roughly coincident with the planar structure visible in the relocated hypocenters occurring between 2001 and June 2012 (Figure 2.1.5, bottom). Over time the events show no evident relationship with Cavone well #14 (Figure 2.3.7), i.e. there is no evidence that they move closer to, or further away from, the well.

During August 2013-June 2014 time period, both the ISC catalog and INGV reported hypocenters within the area mapped in Figure 2.3.4 (ISC: 3 earthquakes; INGV: 45 earthquakes). These included events not located by the Operator (one ISC event and 38 INGV

events). Only one of the INGV-reported events had a magnitude exceeding M3 (4 September 0703 M3.3).

However, several kinds of evidence suggest that the local network reported locations are reliable. There are fewer outliers among the local-based location than those reported by INGV and, the Operator did locate two of the three earthquakes reported by the ISC— in both cases the local network-based and ISC locations differed by ~8 km, but the local one are likely to be superior because the Cavone stations were closer to the epicenters. Finally, as mentioned previously, the local network-based locations occupy a region that is similar to that of the 2001-June 2012 relocated events (compare Figures 2.1.5 and 2.3.5).

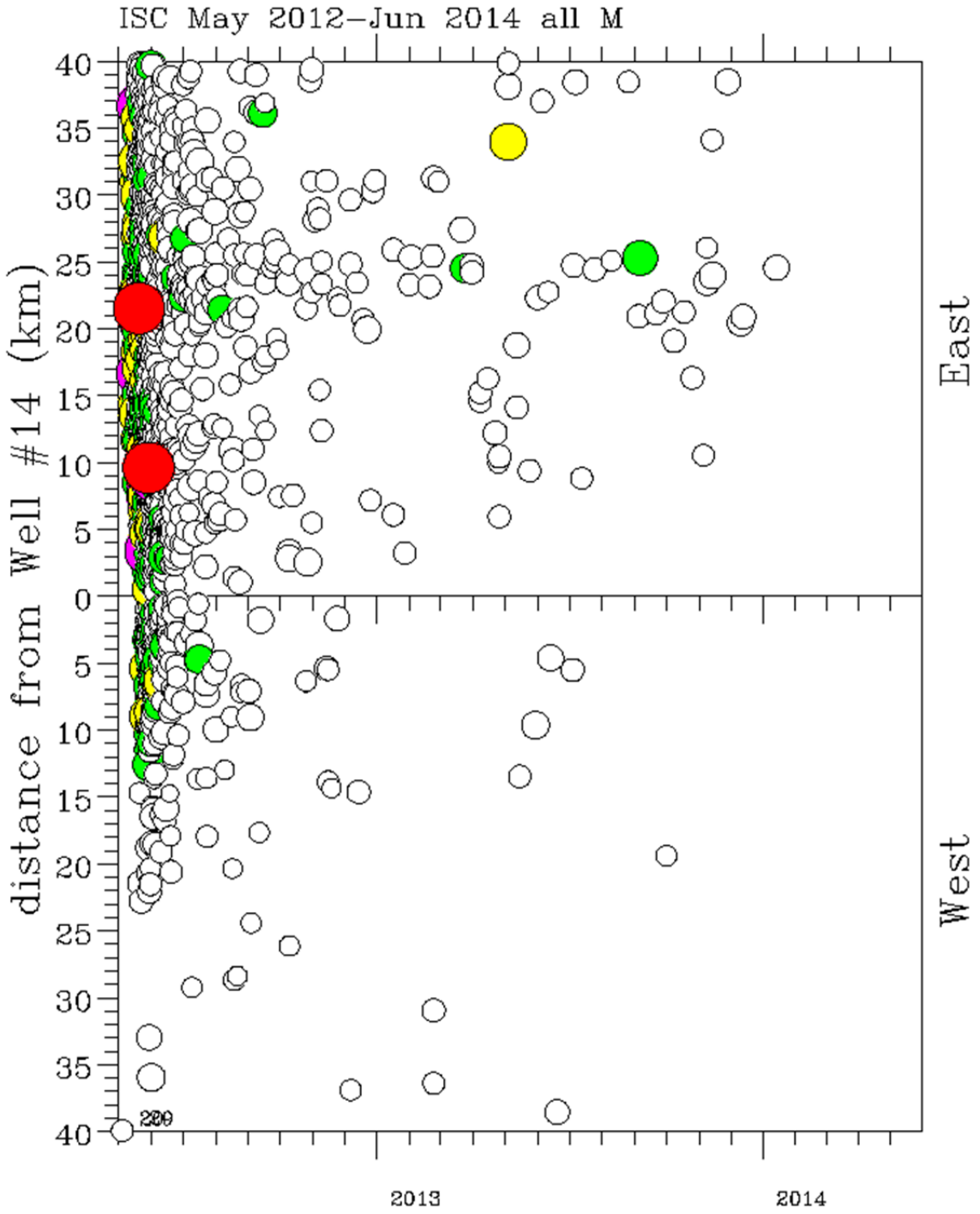

Figure 2.3.1: Space-time plot of ISC-reported epicenters (circles; plot includes events with M < 2.5) in May 2012-June 2014. Vertical axis shows distance between epicenters and Cavone well #14; upper part of plot shows earthquakes east of well; lower part shows earthquakes west of well. Colors/sizes indicate reported magnitudes; white: M<3; green: 3 < M < 4; yellow: 4<M<5; pink: M>5; red: 20 May and 29 May 2012 largest events.

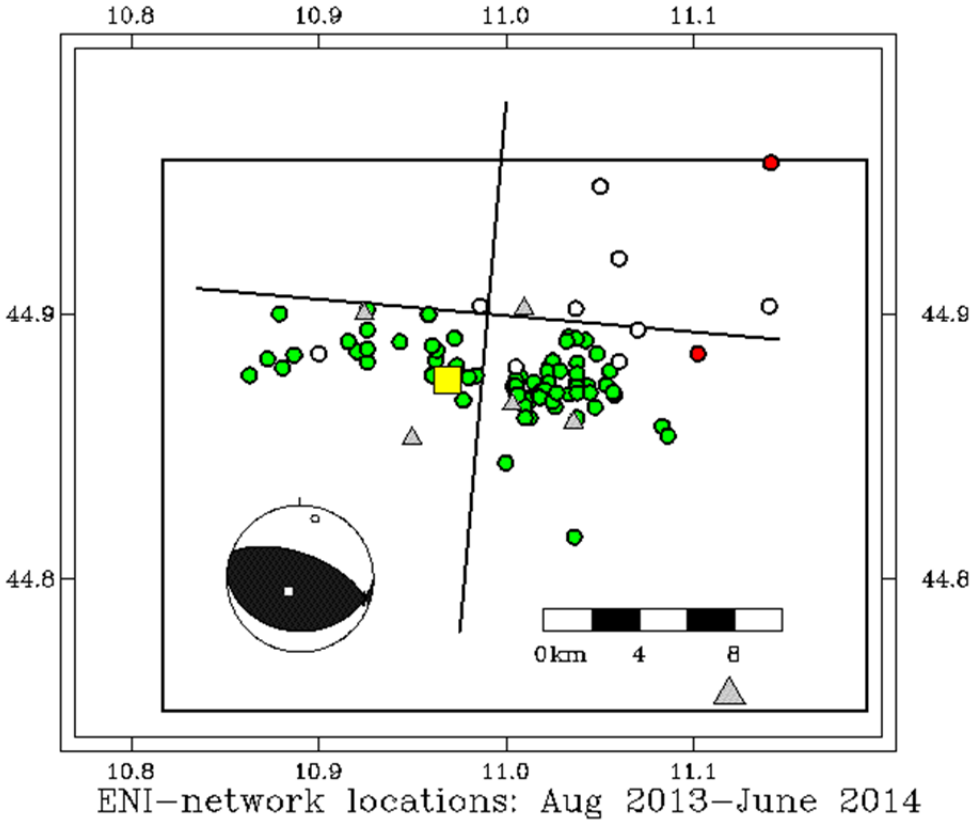

Figure 2.3.2. Map of epicenters (circles) located near Cavone well #14 (yellow square) between August 2013 and June 2014. Green circles: locations from local-operated seismic network; white circles: locations from INGV temporary survey; red circles: two events reported by the ISC and also located by the field Operator. Triangles are seismic stations. Plotted focal mechanism is from the Global GCMT catalog for the 29 May 2012 earthquake.

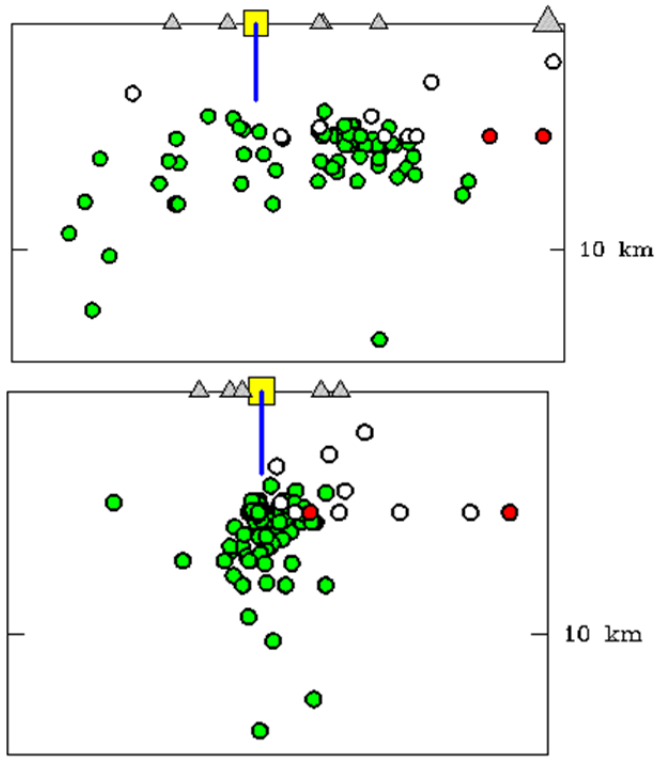

Figure 2.3.3. Cross sections for events mapped in Figure 2.3.4.. Green circles: locations from local-operated seismic network; white circles: locations from INGV temporary survey; red circles: two events reported by the ISC and also located by the Operator. Triangles are seismic stations. Yellow square and blue line are Cavone well #14.

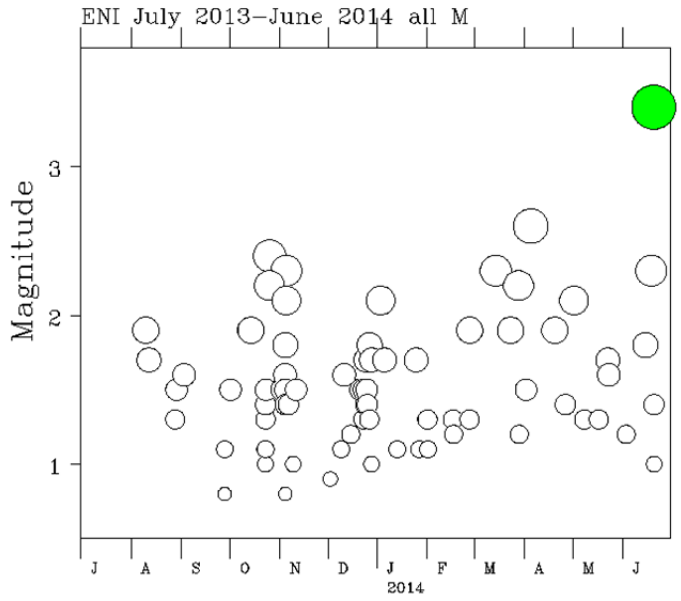

Figure 2.3.4. Magnitude-time plot for locations of events recorded by the local network and mapped in Figure 2.32. Green circle is earthquake occurring 19 June 2014 22:43 and assigned M3.4 by the Operator's seismologists.

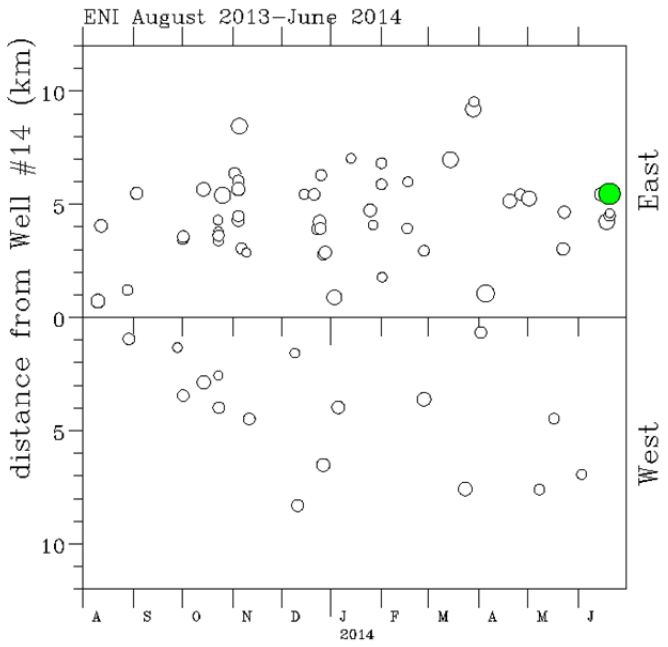

Figure 2.3.5: Space-time plot of earthquakes recorded by the local network and mapped in Figure 2.3.2. Green circle is earthquake occurring 19 June 2014 22:43 and assigned M3.4 by the Operator's seismologists.

2.4 COSEISMIC DEFORMATION AND ESTIMATES OF EARTHQUAKE SOURCE PROPERTIES

Pezzo et al. (2013) have published a detailed study of the coseismic deformation for the Emilia-Romagna earthquakes, including GPS data, and InSAR observations from both Radarsat-1 and COSMO-SkyMed. They also estimated source properties by inverting the geodetic data using the Okada (1985) expressions for deformation from dislocations in a uniform elastic halfspace. Geodetic coverage for these events was very good, as described by Serpelloni et al. (2012), and Pezzo et al (2013) were able to determine relatively detailed source models.

Figure 2.4.1 provides a good summary of their InSAR observations of deformation, the predicted deformation from their models, and the residual deformation not predicted by the models. Repeat observations by COSMO Sky-Med (top row) between 19 May 2012 and 23 May 2012 provide excellent constraints on the deformation on the eastern edge of the 20 May rupture zone, showing a range in change of line-of-site (LOS) of up to 14 cm. Similarly, repeat observations by COSMO Sky-Med (bottom row) between 27 May 2012 and 04 June 2012 provide excellent constraints on the deformation over the entire rupture zone of the 29 May events, showing a range in change of line-of-site (LOS) of up to 22 cm. Finally, by subtracting these from Radarsat-1 repeat observations on 12 May 2012 and 04 June 2012,

they were able to put together an estimate of the deformation over the entire rupture zone for the 20 May earthquake (middle row). They also obtained estimates of the coseismic deformation at up to 13 GPS sites (third column).

Profiles of observed and modeled changes in LOS along the profiles indicated in Figure 2.4.1 are shown in Figure 2.4.2 along with the projections of the model fault planes. The overall fit of models to data in these two figures is very good. The main discrepancy is that the models are somewhat smoother than the data. This discrepancy may be the result of assuming a uniform elastic halfspace, rather than a more realistic elastic model that is better tied to the geology and seismology. But, for the purposes of this study, these models are probably sufficient.

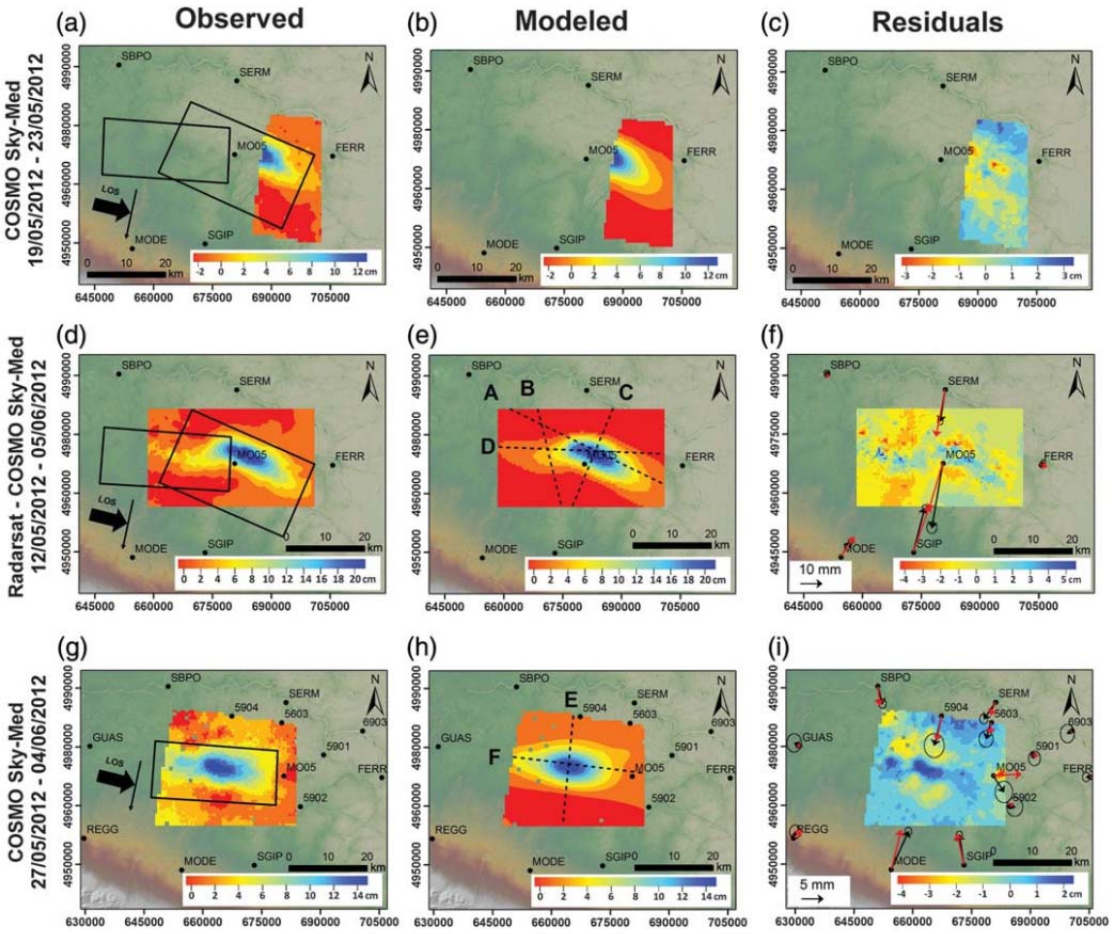

Figure 2.4.1: (Figure 3 of Pezzo et al., 2013) (a, d, g) Observed, (b, e, h) modeled, and (c, f, i) residual displacement maps of two unwrapped COSMO-SkyMed interferograms and one Radarsat minus COSMO-SkyMed map relating to the 20 May (a-f) and 29 May (g-i) earthquakes. Satellite paths and line-of-sight (LOS) directions are shown in (a, d, g); black boxes, surface projections of the modeled faults; black dashed lines, traces of the profiles shown in Figure 2.4.2. In (f, i) we show the GPS (red) modeled and (black) observed displacements for the 20 and 29 May events, respectively.

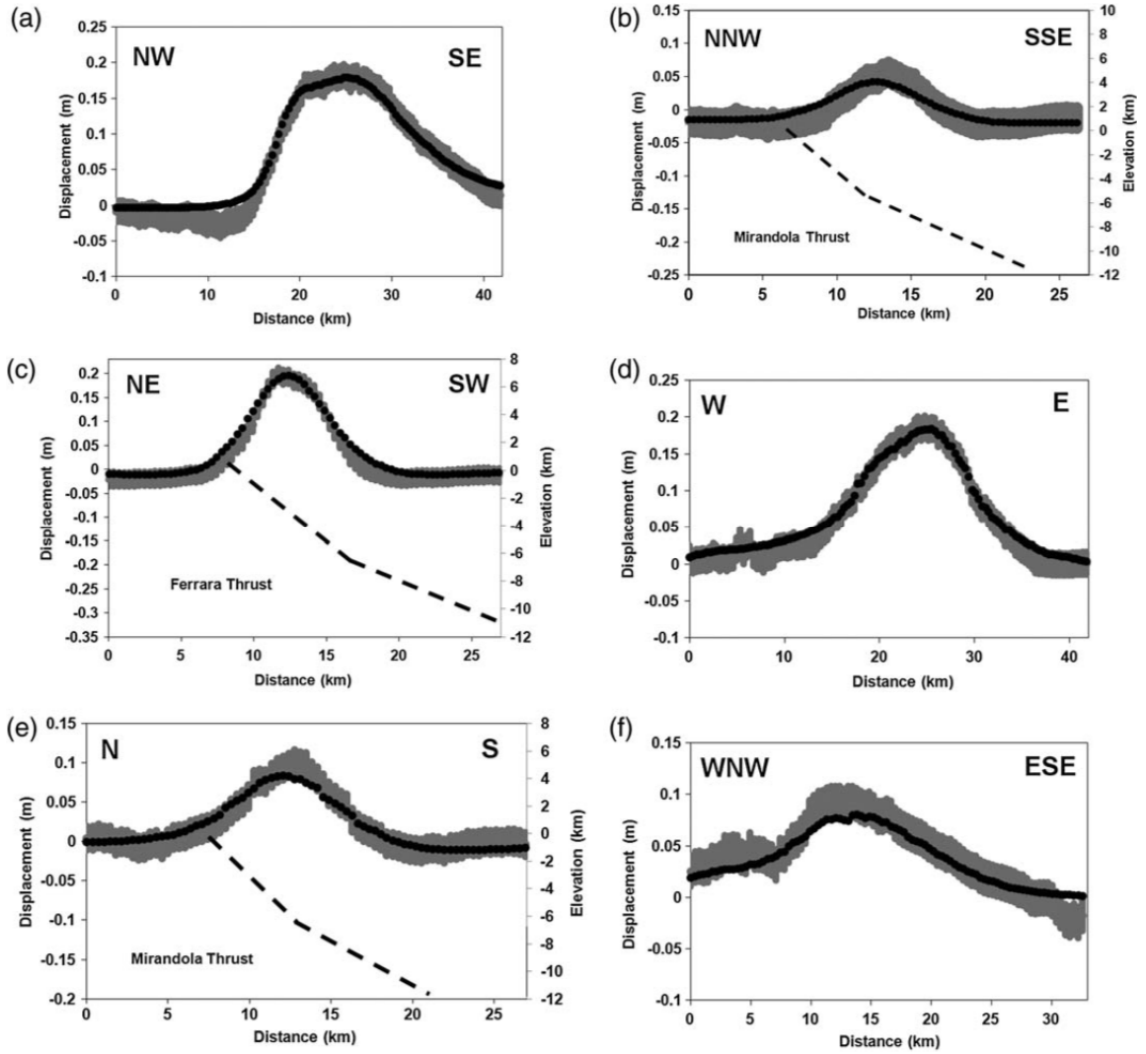

Figure 2.4.1: (Figure 5 of Pezzo et al., 2013) Gray (observed) and black (modeled) displacement profiles (a-d) for the 20 May and (e and f) 29 May seismic events. A mean error bar of 1.5 cm is associated with the SAR data. Black dashed lines illustrate the modeled fault planes. The profile traces are shown in Figure 2.4.1e,h.

The earthquake source models of Pezzo et al. (2013) were estimated using a two-step approach. First, the nonlinear problem of estimating fault location, extent, and orientation was solved using one single dislocation with uniform slip for each of the two events. Second, for each event, the fault was parameterized to conform to the geologic structure, using a more steeply dipping shallow fault and a more gently dipping deeper fault (see Figure 2.4.2). Each of these faults was discretized into 1.5 x 1.5 km squares, with the (assumed smooth) slip distribution estimated using a damped linear inversion. A perspective view of their preferred solutions is shown in Figure 2.4.3. The eastern plane corresponds to the main rupture plane of the 20 May event, while the western plane corresponds to the main rupture plane of the 29 May events. Note, however, that slip (perhaps aseismic) is inferred to have occurred of the

western plane at some time before 27 May in response to the 20 May event but preceding the 29 May events.

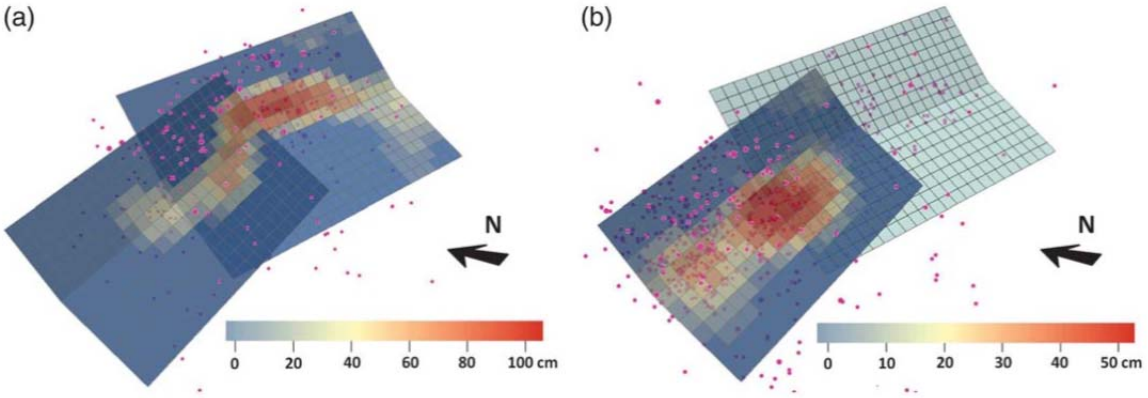

*Figure 2.4.2: (From Figure 6 of Pezzo et al., 2013) (a) and (b) The slip distribution (1:5 × 1:5kmpatches) along the 20 and 29 May sources, respectiv*ely. Purple spheres represent the hypocenters (http://iside.rm.ingv.it; ML > 2 during the following *time spans: (a) 17-28 May 2012 and (b) 29 May- 11 June 2012.*

For the 20 May event, the maximum displacement (~ 1,200 mm) occurs at 5 km depth on the northeast fault (Ferrara thrust). There is also some slip on the inferred fault plane of the 29 May event. For the 29 May event, the slip model shows two main peaks. The maximum slip (540 mm) occurs in the central part of the fault at a depth of ~ 6 km. There is a secondary maximum (~300 mm) on the western side at ~ 5 km depth.

The 5 km depth where maximum slip is estimated to have occurred is comparable to the 6 km hypocentral depth for the 20 May event inferred from seismology. However, the 5-6 km depth where maximum slip is estimated to have occurred for the 29 May event substantially shallower than the ~ 10 km hypocentral depth inferred from seismology. This might indicate that this rupture grew in magnitude as it propagated upward from depth. Alternatively, the geodetic estimates may be too shallow because of the assumption of a uniform elastic halfspace in the model used to produce them.

2.5 COULOMB STRESS CHANGES AND TRIGGERED EARTHQUAKES

One of the most important discoveries in the study of naturally occurring (tectonic) earthquakes is the realization that a substantial fraction of earthquakes are triggered not just by the slow buildup of tectonic stresses, but by more rapid stress changes generated by previous earthquakes (Stein, 1999, 2003; for a recent review, see Freed, 2005). An example from southern California is the triggering of the June, 1992, M 7.3 Landers earthquake by the April, 1992 M=6.1 Joshua Tree earthquake. This in turn triggered the M 6.3 Big Bear, California 3½ hours later Figure 2.5.1). An example from Turkey is the triggering of the

October, 1999 M 7.1 Düzce earthquake by the M=7.4 Izmit earthquake 3 months earlier. There are many other examples. Incorporation of this transient stressing into models of fault loading has become an important part of the development of a new generation of real-time earthquake forecasting models.

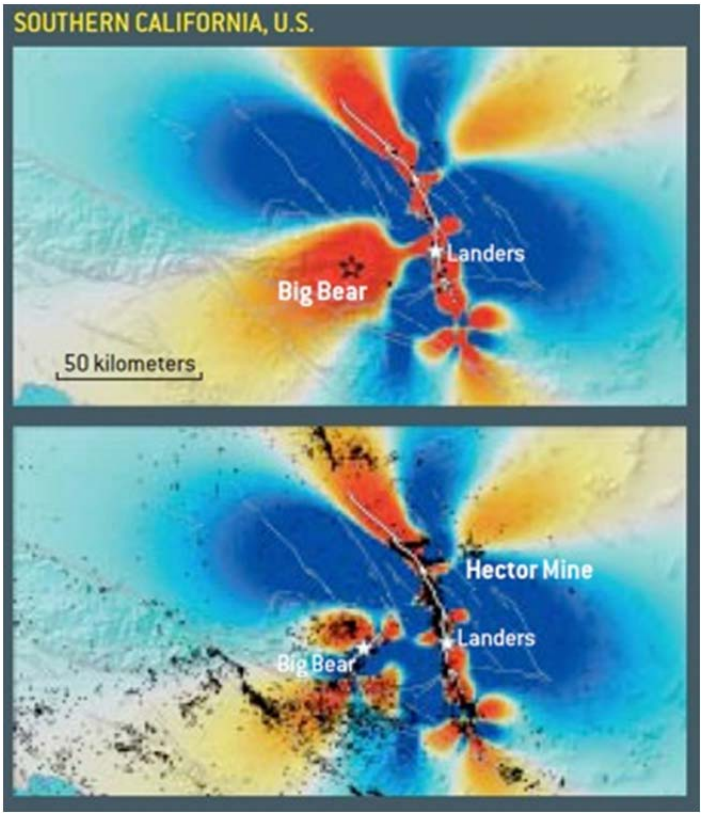

Figure 2.5.1: A magnitude 7.3 earthquake in the southern California desert near Landers in 1992 increased the expected rate of earthquakes to the southwest, where the magnitude 6.5 Big Bear earthquake struck three hours later (top). Stresses imparted by the combination of the Landers and Big Bear events coincided with the regions where the vast majority of tremors occurred over the next seven years, culminating with the magnitude 7.1 Hector Mine quake in 1999 (Bottom) (Stein, 2003).

Earthquakes typically occur by rapid shear failure, with the rocks on either side of a fault slipping in opposite directions. The classic view, correct to first order, is that failure occurs when the shear stress on the fault plane, τ, increases to a value given by the Mohr-Coulomb failure criterion:

$$\tau_f = \mu_s(\sigma - p) \qquad \text{Eq. 1}$$

Here μ_s is the static coefficient of friction, σ is the normal stress on the rupture plane (compression positive), p is the pore fluid pressure. Equation (Eq. 1) assumes that the breaking strength of the fault is negligible for active faults such as those under consideration here. Once the fault begins to slip, the fault typically weakens, with the coefficient of friction dropping to a dynamic value, μ_d. Faults on the verge of slip are called "critically stressed." The Mohr-Coulomb criterion works well in the laboratory on small specimens (e.g., Byerlee, 1978; Lockner and Beeler, 2003) and appears consistent with the limits of stress measured in the crust if pore pressure effects are included (e.g., Townend and Zoback, 2000).

Changing of any of the parameters in (Eq. 1) should move a fault closer to or further from failure. Unfortunately, none of these parameters are known with sufficient accuracy to predict when a given fault or fault segment is about to reach the failure stress, τ_f. However, we can estimate when the changes in conditions on a fault increase or decrease the probability of fault slip. This effect is quantified by defining the Coulomb stress change, $\Delta\tau_c$, also known as the Coulomb Failure Function, CFF, as:

$$\Delta\tau_c = \Delta\tau - \mu_s (\Delta\sigma - \Delta p) - \Delta\tau_0 \qquad \text{Eq. 2}$$

(Note that for a poroelastic material, changes in mean normal stress, $\Delta\bar{\sigma}$, and pressure are coupled. For example, for undrained conditions, $\Delta p = B\Delta\bar{\sigma}$, where B is Skempton's coefficient. Because of this, changes in normal stress may vary over time as the material drains.) On faults where $\Delta\tau_c$ is positive and $\tau_f - \tau \leq \Delta\tau_c$, earthquakes should move closer to or reach failure, while in regions where $\Delta\tau_c$ is negative, faults should move further from failure. Typically the response is not instantaneous, but falls off according to Omori's law. Phenomena like fluid flow or the second order frictional effects described below may explain the time delay between forcing by $\Delta\tau_c$ and induced earthquakes. Quasi-static models of near-field Coulomb stress changes, $\Delta\tau_c$, (ignoring pore-fluid pressure changes) have been applied to tectonic earthquakes (e.g., Hardebeck et al., 1998; Stein, 1999; Toda et al., 2002; Toda et al., 2005; Toda et al., 2012).

The fact that earthquakes are triggered in the far-field, where static stress changes are tiny, provides strong evidence that dynamic triggering can also be important (e.g., van der Elst and Brodsky, 2010, 2013; Husen et al., 2004; Wang et al., 2004; West et al., 2005), and may induce 15%-60% of the triggered events in the near-field (van der Elst et al., 2013). Proposed mechanism(s) to explain dynamic triggering include increases in pore-fluid pressure facilitated by shaking-induced permeability increase (Brodsky et al., 2003; Elkhoury et al. 2006a; Manga et al., 2012) and dynamic weakening of fault gouge, leading to a decrease in coefficient of friction (Johnson and Jia, 2005; Parsons, 2005; Taira et al., 2009). Convertito et al. (2013) suggest that most of the aftershocks in the Emilia-Romagna earthquake sequence were dynamically triggered by the shaking generated by preceding events in the sequence. Although this hypothesis is interesting, we do not pursue it further in this study because our

focus is on evaluating whether the stress changes caused by production, which are quasi-static, might have played a role in inducing the sequence.

The time delay in triggered seismicity may occur because the coefficient of friction, μ, is a function of fault slip rate and slip history in a way that makes the response to stress time-dependent in a very interesting way (e.g., Dieterich, 1994; Marone, 1998; Scholz, 1998). The essential ingredients of "rate-state friction" are that the coefficient of friction, μ, is not a constant, but has a small but important dependence upon both the fault slip rate, V, and the evolving "state" of the fault, θ, where θ is a measure of contact age (Dieterich and Kilgore 1994). There are several empirical descriptions of rate-state friction (e.g., (Marone 1998); the one that we use to illustrate here is due to Dieterich (1979a), (see also Dieterich, 1979b; Linker and Dieterich 1992), expressed as:

$$\mu = \mu_0 + a\ln(V/V_0) + b\ln\left(\frac{V_0\theta}{D_c}\right); \qquad d\theta = \left[\frac{1}{V} - \frac{\theta}{D_c}\right]d\delta - \left[\frac{\alpha\theta}{b\sigma}\right]d\sigma; \quad V = \dot{\delta} \qquad \text{Eq. 3}$$

Here a and b are parameters that describe the effects of slip velocity, V, and evolving state, θ, V_0 is a reference velocity, D_c is the characteristic slip distance over which θ evolves, and α is a parameter in the range 0.25 – 0.50 (Linker and Dieterich, 1992). If a fault slipping at an imposed velocity V_1 has its slip velocity increased instantaneously to V_2, the coefficient of friction, μ, (of order 0.6 for earth materials) is instantaneously increased by $a\ln(V_2/V_1)$. The coefficient of friction then relaxes by $b\ln(V_2/V_1)$ as the state evolves over a distance D_c to reach a new steady value of μ, reduced by $(a\text{-}b)\ln(V_2/V_1)$ from its initial value. When $b > a$, "dynamic friction" is less than "static friction," and the behavior is called "velocity weakening" (e.g., granite or wood). However, if $a > b$, increasing V increases the steady-state value of μ, and the fault slides stably, or "velocity strengthening" (e.g., serpentinite or Teflon on steel).

The friction parameter (a-b), determines whether slip is unstable, resulting in earthquakes, or stable, leading to fault creep. (a-b) is sensitive to many parameters, including mineralogy, temperature, and pressure. Although fault slip is commonly thought to result in seismic events, whether fault slip occurs by stick-slip events or by stable sliding depends on whether μ decreases or increases with sliding velocity, as well as the effective stiffness of the system. Thus the fraction of total fault slip that is accommodated via tremors is not known a priori.

Regardless of whether stress and/or pressure changes are static or dynamic, rate-state friction leads to a time delay between changes in stress (or stressing rate) and changes in the rate of seismic activity. Dieterich (1994) and Kanamori and Brodsky (2004) provide comprehensive discussions, showing how the temporal evolution of slip can be calculated for any given stressing history. For purposes of illustration, suppose that there is a constant background stressing rate, $\dot{\tau}_r$, in a region and that the distribution of slip rates on faults is such that it

leads to a constant seismicity rate, r_0. Figure 2.5.3 (from Toda et al., 2002) shows how fault systems respond to variations in stress and stressing rate. Because fault friction evolves with slip, responses to stress and stressing rate changes are not instantaneous, but occur over a finite time. Thus rate-state friction enables us to understand the time delay between forcing and seismic activity.

In the context of the Emilia-Romagna earthquake sequence, there are two hypotheses that should be considered. The first is that the events are tectonic in origin, with the May 2012 sequence a cascade of aftershocks. Figure 2.5.2.c and d show how "aftershocks" can occur during an interval after a sudden stress change. The second is that the sequence is the result of a change in stressing rate associated with production, e.g., in the Cavone field. In that case, Figure 2.5.3 a and b show how the tectonic rate of seismicity would change given the change in Coulomb stressing rate caused by the production. The other important parameter is the background stressing rate associated with the tectonic strain accumulation. For a tectonic deformation rate of ~1 mm/yr over a distance of ~ 50 km (Figure 1.5.1) and a Youngs modulus of ~ 8 10^5 bars, a typical stressing rate is ~0.02 bars/yr.

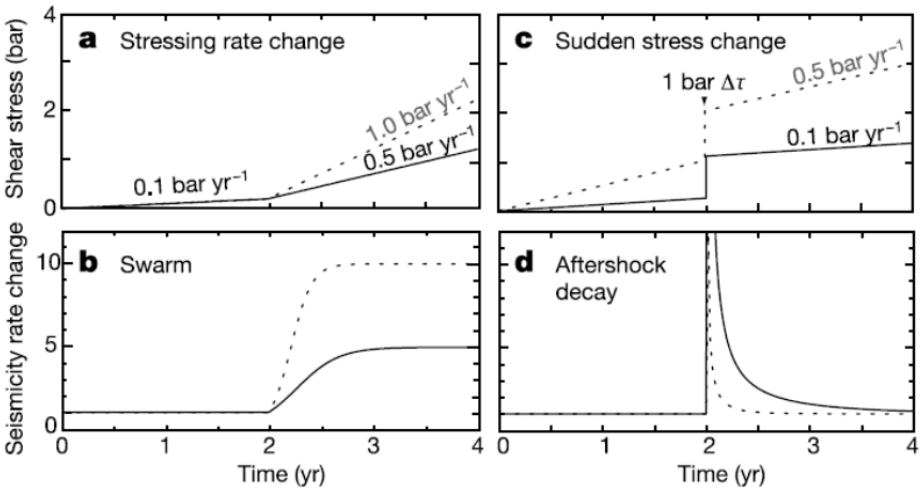

Figure 2.5.2: (From Toda et al., 2002) The rate/state effect of stress on seismicity. A change in the stressing rate (a) causes a swarm (b). A sudden stress change, $\Delta\tau$ (c), causes an aftershock sequence that decays inversely with time (d). Comparison of dashed and solid curves shows that the higher the stressing rate, the more quickly the seismicity rate reaches equilibrium.

As shown in Table 2.2.1, the Emilia-Romagna earthquake sequence began with 4 foreshocks within two days of the M_W 6.0 event on 20 May 2012. Then, after a series of aftershocks, the M_W 5.8 event and another large event almost as large occurred. This raises the questions of how large was the change in Coulomb stress at the 20 May hypocenter from the 19 May foreshock and how large was the change in Coulomb stress at the 29 May aftershock hypocenter from the 20 May mainshock. We have used the USGS Coulomb3.3 software (Lin and Stein, 2004; Toda et al., 2005) to calculate the change in Coulomb stress in the region of the mainshock of 20 May 2012 from the m_b4.2 foreshock the day before (Figure 2.5.3),

assuming that their focal mechanisms were the same. The locations in Table 1.1.1 indicate that the hypocenters of these two events were very close, with the foreshock nominally < 2.5 km WNW and 0.1 km shallower than the mainshock. The warm colors indicate stress changes that would bring a reverse fault closer to failure. The stress change from the foreshock is several bars and of the direction to trigger the mainshock, although the stress varies on distances small compared to the uncertainties in the relative locations of the events. Because changes in Coulomb stress > 0.1 bars are consistent with levels used elsewhere in the context of the Coulomb triggering hypothesis (Hardebeck et al., 1998), it is very plausible that the 20 May mainshock was triggered by the 19 May foreshock. Alternatively, the dynamic stresses from the foreshock at the hypocenter of the mainshock are large enough that dynamic triggering might well have been the cause of the mainshock.

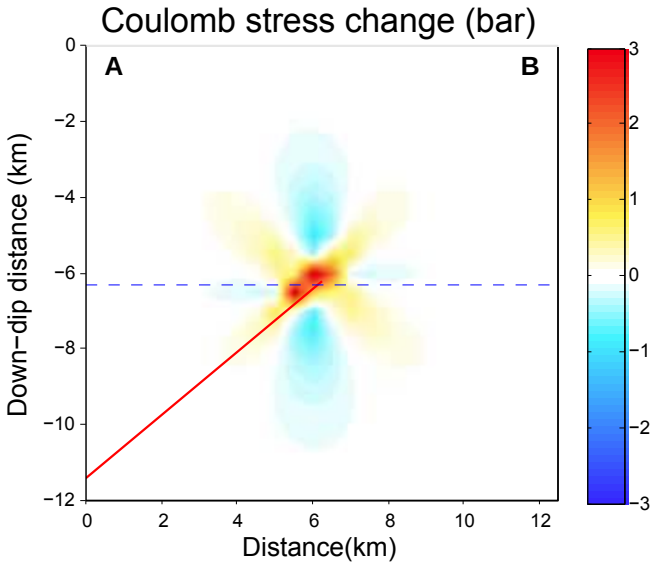

Figure 2.5.3 Coulomb stress changes induced by the May 19 foreshock near the hypocenter of the May 20 main shock. The plot is a cross section on a plane passing through the hypocenter of the 20 May main shock and perpendicular to the strike of its fault plane. The hypocenter of the mainshock is at the intersection of the red line and the dashed blue line near the middle of the figure. Point B is NE of the hypocenter, with point A to the SW. Warm colors indicate stress changes tending to initiate earthquakes on reverse faults with dips of 40°, the dip of the fault plane of the main shock (red line). The maximum stress change is 3.2 bars.

Pezzo et al. (2013) investigated whether the static changes in stress associated with the 20 May mainshock were large enough to explain the occurrence of the largest 29 May aftershock. Their results (Figure 2.5.4) are quite definitive and support earlier study by Ganas et al., (2012). The changes in Coulomb stress exceed 6 bars in the eastern sector of the fault plane of the aftershock – larger than changes that have been used to explain other tectonic earthquakes. Thus the 29 May aftershock is explained in the most straightforward way as the result of stress changes from the 20 May event.

In fact, the entire Emilia-Romagna sequence has the signature of a classic cascade of earthquakes. Figure 2.5.5 shows the daily number of aftershocks as a function of magnitude through this sequence. This plot can be explained as the sum of three sequences of aftershocks of the type predicted by rate-state friction in Figure 2.5.2d. The activity began with the foreshocks of 18 and 19 May, which triggered the mainshock on 20 May. The rate of earthquakes increased immediately after the mainshock, then decayed (first sequence) until the 29 May aftershock. The 29 May aftershock was large enough to trigger a second burst in aftershock activity, with the rate declining until 3 June (second sequence). At that time, an additional large aftershock triggered a third sequence of increase, followed by decrease in seismicity rate.

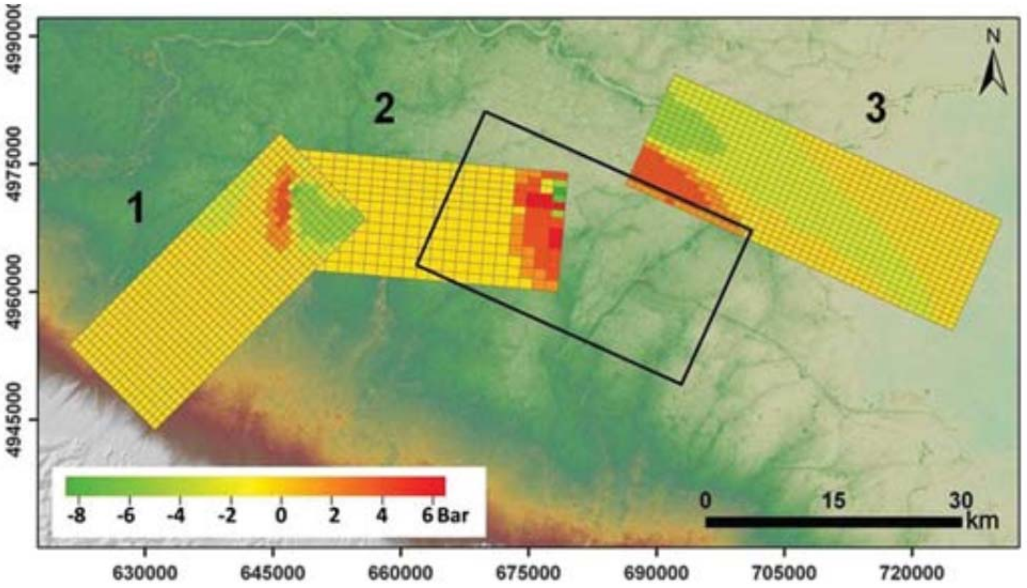

Figure 2.5.4: (Figure 7 from Pezzo et al., 2013): Results of the CFF analysis for three different fault planes. Black rectangle: the source of the 20 May seismic event was used to calculate the Coulomb stress changes on the 29 May plane (fault 2). The patch size is 1:5 × 1:5km. Both 20 and 29 May faults were used to calculate the ΔCFF on the western lateral ramp of the Mirandola thrust (fault 1), defined according to geological data (Boccaletti et al., 2010), and on the external thrust of the Ferrara fold belt (fault 3; Boccaletti et al., 2010). For faults 1 and 3 the patch size is 1 × 1km.

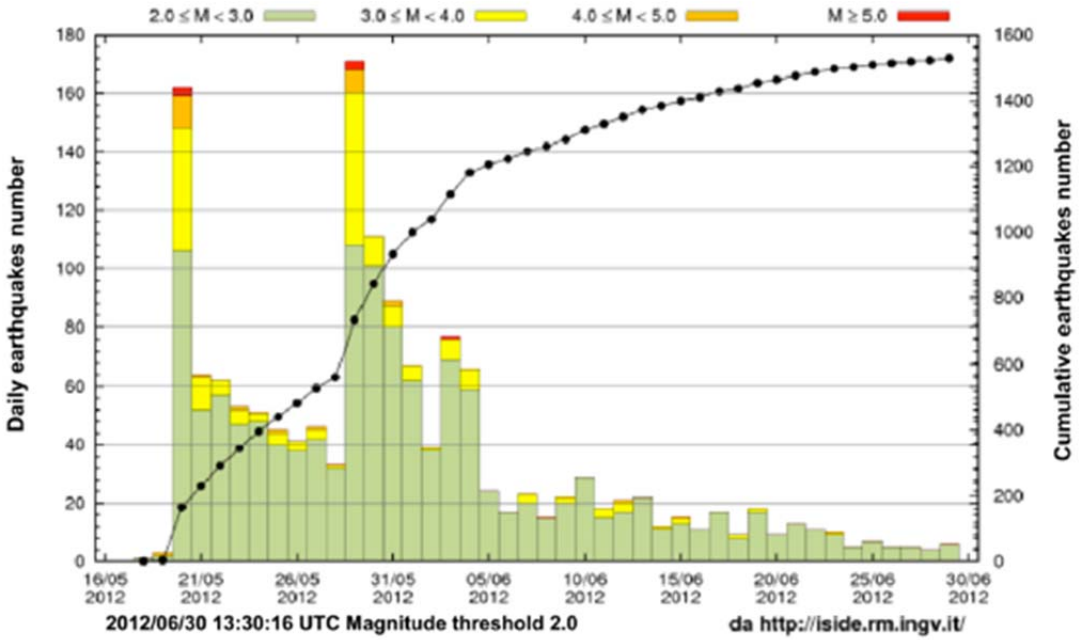

Figure 2.5.5: Plot of the daily number of earthquakes of various magnitudes through the Emilia-Romagna earthquake sequence. Three sudden increases in activity, followed by more gradual decreases of the type shown in Figure 2.5.2d are evident.

2.6 CONCLUSIONS ABOUT SEISMICITY IN REGION NEAR CAVONE WELL #14

- *Between 1964 and today regional seismograph network coverage has changed several times for the region surrounding Cavone well #14; since about 2005 this has allowed the detection and location of increased numbers of small earthquakes (M < 2.5) that would not have been detected previously.*

- *A four-station seismograph network operated locally around the Cavone field has allowed Operator's scientists to locate many small earthquakes (M<2.0) that are not in the ISC catalog.*

- *The historic record shows that the region within 40 km of Cavone well #14 has experienced severely damaging earthquakes, most notably in 1570 and 2012 and probably in 1761 near the town of Mirandola.*

- *As reported in the ISC catalog, the seismic activity since 1964 is dominated by aftershocks from a M4.7 earthquake in 1986, a M5.3 in 1996, and the M6.0 and M5.8 earthquakes on 20 May and 29 May 2012.*

- *The 20 May 2012 earthquake rupture began about 20 km east of Cavone well #14 and the aftershock sequence extended to within 8 km east of the well. The 29 May earthquake rupture began about 10 km east of Cavone well #14 and aftershocks extended westward to*

at least 12 km west of the well. A few additional events, either aftershocks or events caused by stress changes associated with the 29 May earthquake, occurred at distances of 15-30 km west of the well.

- *To obtain accurate focal depths for representative earthquakes in this region, we relocated selected earthquakes using data recorded by both local-network and regional seismographs. These selected, very-well-recorded earthquakes, occurring between 2001 and June 2012, had focal depths between ~5-10 km and were situated along a south-dipping plane that coincided approximately with the probable rupture surfaces of the May 2012 earthquakes.*

- *The 20 May 2012 earthquake resulted in changes in Coulomb stress at the hypocenter of the 29 May 2012 aftershock that are estimated to be large enough (6 bars) to have triggered this aftershock. In the literature, changes in Coulomb stress over an order of magnitude smaller than this value have been convincingly demonstrated to trigger aftershocks.*

- *Aftershocks of the May 2012 earthquakes continue today. Between June 2013 and June 2014, the Operator's scientists have located 75 earthquakes within ~10 km of Cavone well #14. Most of these events are small (M<2), and only three also were reported in the ISC catalog.*

3 MECHANISMS FOR INDUCED SEISMICITY AND THEIR APPLICABILITY TO THE CAVONE FIELD

Several mechanisms have been proposed for inducing earthquakes both by fluid injection and by fluid production. The fluid injection mechanism is well understood and firmly established through numerous published laboratory, theoretical, and field studies. The majority of widely accepted cases of induced seismicity resulting from oil field operations are by this mechanism. Two different mechanisms have been proposed for inducing earthquakes by removal of subsurface fluids through volume or mass changes. The first is based on the stresses that arise near reservoirs that result from poroelastic interactions as pore fluids are removed and the reservoir compacts Segall (1985; 1989; Grasso 1992). The second assumes an isostatic recovery, in the form of an earthquake, is needed to rebalance the short-term isostatic stresses following removal of mass from a reservoir (McGarr, 1991). Finally a mechanism, which is primarily relevant to geothermal fields, arises from removal of heat from the subsurface and the resulting thermo-elastic stressing (by contraction of the reservoir formation). In the following we review each of these possible mechanisms in the context of the Cavone field.

3.1 EARTHQUAKES BY FLUID INJECTION

3.1.1 MECHANISM

An earthquake is the result of sudden unstable slip of a fault, which is driven by the shear stress acting on the fault surface. An earthquake occurs when shear stress exceeds the fault strength. In the most basic form, the relationship between fault stresses, fault strength, and fluid pressure at the onset of slip is given by the Coulomb criterion for fault slip

$$\tau = \mu(\sigma - P) \qquad \text{Eq. 4}$$

where τ and σ are is the shear and normal stress, respectively, acting on the fault surface, μ is the coefficient of fault friction and P is the pore fluid pressure. This is also given in Eq.1 . Typically, μ has values of about 0.5-0.7. The quantity $\sigma_{eff} = (\sigma - P)$ is the effective normal stress. This relationship has been extensively validated in numerous laboratory tests and field case studies (e.g., Byerlee, 1978; Lockner and Beeler, 2003). Except for the brief moments during earthquakes, a seismogenic fault is normally in a stable stationary state ($i.e.,\ \tau < \mu(\sigma - P)$). From equation (3.1.1) it is seen that a fault can be brought to an unstable condition (an earthquake) through an increase of shear stress τ, a decrease of the normal stress σ, an increase of fluid pressure P, or some combination of the three.

The effect of fault slip in an earthquake is to decrease the shear stress, τ, which restores the fault to a stable condition. Hence, sustained tectonic earthquake activity is understood to arise primarily from regional increases of τ. Also, changes of σ certainly play a role in dip-slip earthquakes. Some natural earthquakes particularly earthquake swarms, are thought to possibly involve increases of fluid pressure, perhaps from sudden upward migration of deep fluids.

Complete analysis of effects of pore pressure changes on earthquake occurrence can be rather complex because increases of pore-fluid pressure, in addition to reducing effective normal stress, also directly alter both τ and σ in Eq. 4 through poroelastic effects. The poroelastic effect is discussed in Section 3.2. Because the direct stress changes from poroelasticity are small compared to fluid pressure changes, poroelastic effects are usually ignored when considering possible cases of triggered or induced seismicity by fluid injection. This assumption is conservative because stress changes from poroelasticity usually act to stabilize faulting in rock volumes where fluid pressure increases — that is an increase of P results in a small increase of σ, which slightly reduces the destabilizing effect of increasing pressure in Eq. 4.

Equation 4 has significant implications for injection operations at producing fields. Oil or gas extraction, in the absence of injection, reduces pore fluid pressures in and around the reservoir. Because of this, at Cavone there are competing effects injection-related increases in pore fluid pressure, and production-related decreases in pore fluid pressure. To potentially cause earthquakes, injection operations must increase pore fluid pressures above the ambient conditions that existed prior to initiation of production operations. In general therefore, injection operations that maintain fluid pressures at or below pre-production levels are thought to be incapable of inducing earthquakes through a reduction of effective normal stress.

This important principal was first verified by field experiments at the Rangely, Colorado (USA) oil field (Raleigh et al., 1976) and subsequently validated by studies of induced earthquakes in other regions. At Rangely, a sequence of earthquakes along a fault that cut through the oil field began after the start of water flooding operations. Those operations increased the fluid pressures in the vicinity of the fault to 290 bars. The pre-production fluid pressure was 170 bars. Field and laboratory measurement were made of the quantities in equation 3.1.1 and it was determined that a fluid pressure of 257 bars was required to activate the fault. Field experiments that varied the formation pressures demonstrated that the earthquakes could by turned on and off at the predicted pressure threshold.

Exceeding pre-production fluid pressures is a necessary, but not sufficient, criterion for inducing earthquakes by fluid injection. As the Rangely, Colorado example illustrates, there must also be a fault that is suitably oriented with respect to a pre-existing stress field, and the stresses acting on the fault must be of sufficient magnitude to enable earthquake slip at some threshold fluid pressure. In the vicinity of the Cavone field, in addition to the major thrust faults that sourced the May 2012 earthquakes, there are unmodeled secondary faults that might act as sources for smaller earthquakes.

3.1.2 CHARACTERISTICS OF INDUCED AND TRIGGERED SEISMICITY BY FLUID INJECTION

Because fluid pressure data and subsurface stresses generally are quite uncertain, many claimed instances of triggered seismicity have been put forward primarily through comparisons with the characteristics of well-established cases of induced seismicity. *The following characteristics of injection-induced earthquakes are generalizations, not hard and fast rules.*

1) Space-time patterns. Induced earthquakes by fluid injection generally take the form of locally elevated rates of seismicity that begin after injection operations have commenced. Injection-related earthquakes typically follow a pattern, wherein the points of initiation (hypocenters) of earthquakes in the sequence are both temporally and spatially correlated with the magnitude of the pressure increases on the causative faults. Most earthquakes that are allegedly induced by fluid injection occur within a few km of an injection well, where the injection pressures are greatest. Finally, in cases where injection rates vary with time, corresponding changes in the rates of induced earthquakes are observed. In those cases where injection-related earthquakes occur at distances exceeding ~5 km from a well, they typically begin within a few km of the well and migrate to greater distances. The rare cases where allegedly injection-related earthquakes occurred at distances exceeding ~10 km have generally been in situations where injection has been ongoing for a decade or more (e.g., Paradox Valley in Colorado, U.S.A., see Ake et al., 2005; Block et al, 2014).

   Although injection has been ongoing for more than 20 years in the Cavone field, no pattern of outward earthquake migration from the primary injection well #14 has been observed so far. Indeed, in the vicinity of Cavone, earthquakes migrate at depths > 5 km toward the field (but not into the reservoir) following the 20 May 2012 earthquake. Based on the ISC data (Section 2.2) prior to 2012 most events following the start of injection at well #14 with epicenters within 20 km of that well (Figure 2.1.2) appear to be aftershocks of the M5.3, 15 October 1996 earthquake. That earthquake occurred at a distance of about 20 km southwest of Cavone #14 well and 2-3 km deeper than the reservoir. The along-strike occurrence of the 29 May earthquake west of the 20 May event appears to fit the common pattern of stress triggering by Coulomb stress transfer from the 20 May 2012 to the section of the fault that slipped in the 29 May 2012 earthquake (Pezzo et al., 2013) (Section 2.5).

   Following the May 2012 earthquakes the seismic activity in the vicinity of the Cavone field is strongly dominated by aftershocks. The relocations of selected well-recorded aftershocks in the 2012 Emilia-Romagna sequence (Figures 2.3.3, 2.3.4, 2.3.5) confirm that a few of the epicenters of the ruptures in the 20 May and 29 May sequences extended to within a few km or less of the Cavone #14 well. They also

indicate that in the vicinity of the well the aftershock activity occurred at depths greater than 1-2 kilometers below the 3.4 km deep bottom of the well.

2) Magnitudes of induced earthquakes The magnitudes of injection-related earthquakes often progressively increase with time as the region of excess fluid pressure expands. This effect is understood to arise because the magnitude of an earthquake is directly related to area of the fault that slips. Hence, the larger the region along a fault brought to a critical state by fluid injection, the larger the earthquake.

   A related effect is an apparent correlation of the total volume of injected fluids with the maximum earthquake magnitude (NRC, 2012; McGarr, 2014). Figure 3.1.2 is a compilation of data on injection volume and maximum magnitudes of induced earthquakes from the NAS/NRC Committee on Induced Seismicity Potential in Energy Technologies (NRC, 2012). The figure has been modified from the original to show only cases of seismicity linked to injection for secondary recovery and waste-water disposal. The two largest Emilia-Romagna earthquakes of May 2012 have been added to the plot using the injection volume at Cavone up to April 2012 (Section 3.1.3). Also, a data point has been added for the 2011 Oklahoma earthquake, which is proposed to have been induced in a recent publication (Keranen et al., 2013, 2014).

   Several uncertain variables may affect the relationship between injected volume and maximum rupture area of induced earthquakes. However, even allowing for large uncertainty, the Oklahoma earthquakes stand apart from previously identified cases of injection-induced seismicity — the magnitudes of the events are approximately 1.7 to 2.0 magnitude units larger than expected based on previous cases of induced seismicity with comparable injection volumes. The difference of 1.7 to 2.0 magnitude units corresponds to rupture areas that are 50 - 100 times larger than expected from the injection volumes in other established cases of injection-related seismicity. Assuming the area of the fault that ruptures in an earthquake is embedded in self-similar volumes of rock with elevated fluid pressures, the discrepancy of 1.7 to 2 magnitude units corresponds to injection volumes that are larger than the actual injection volume by factors of 350 to 1000, respectively. In the case of the Oklahoma earthquakes this inconsistency can be explained by some unique features of the reservoirs and earthquake faults (Keranen et al., 2013, 2014) — fluids were directly injected into small volume fault-bounded reservoir compartments (inferred to have high fluid pressures) that directly pressurized sections of the faults.

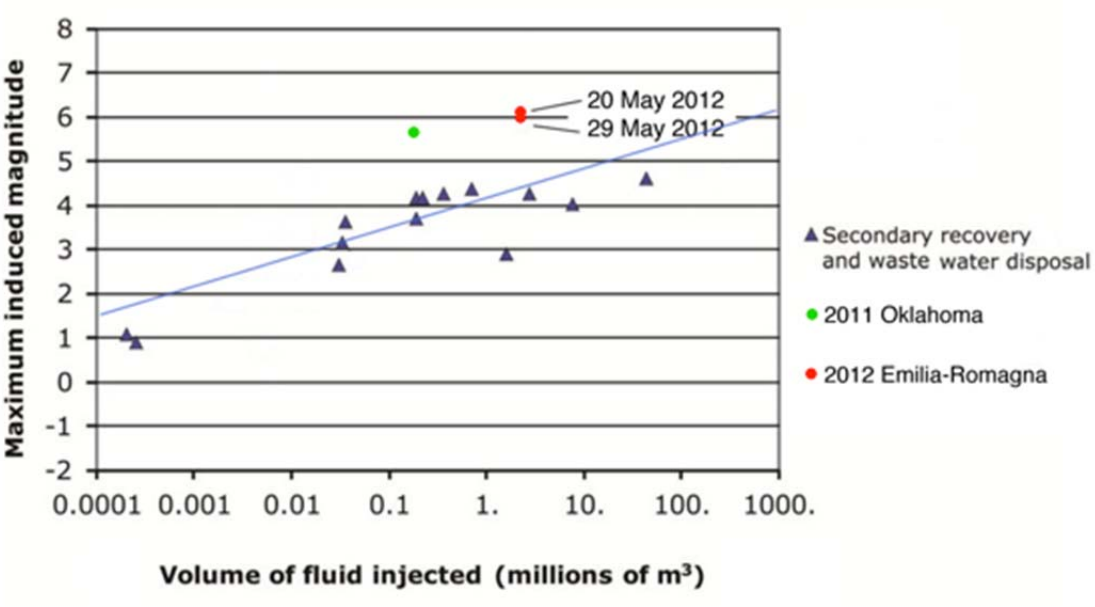

Figure 3.1.2: Compilation of data on the maximum induced seismic event magnitude vs. volume of fluid injected. These are worldwide data for both well-established and somewhat less certain cases of induced seismicity. This figure is modified from NRC (2012) to show only earthquakes linked to fluid injection for secondary recovery and waste disposal. The volume of injected fluid need to pressurize (by some fixed amount) the volume of crust that embeds an induced earthquake rupture, scales by $V \propto 10^{1.5M}$*, which has a slope of 2/3 on this plot (blue line).*

The ISC catalog locations (Section 2) do not provide evidence of a progressive increase of earthquake magnitudes in the vicinity of the Cavone reservoir following the beginning of injection operations. Additionally the application of the statistical regression of Figure 3.1.2 assumes that the required physical conditions for inducing earthquakes by fluid injection (*i.e.* increased fluid pressure, section 3.1.1) have been satisfied. However, below in Section 3.1.3 we examine fluid pressures at Cavone and strongly conclude that the average fluid pressures in the vicinity of the field decreased because production exceeded injection volumes.

3) Magnitude-frequency parameter *b*. A speculative, but as yet un-quantified, correlation of unusual *b*-values with induced earthquakes has been noted in some publications. The earthquake magnitude-frequency parameter *b* is a measure of the decreasing frequency of earthquakes with increasing magnitude. The *b* parameter varies somewhat, but on average takes values near 1.0 for tectonic earthquakes worldwide. Some sequences of induced earthquakes, have larger values approaching *b*~2.0 (NRC, 2012). The frequency distribution of earthquake magnitudes is thought to be controlled by the heterogeneity of conditions on the faults that produce the earthquakes — hence, the larger value of *b* for some induced earthquake sequences may result from steep along-fault gradients of the effective stress that arise from steep un-equilibrated fluid pressure gradients.

The distribution of event magnitudes for the period 1982 –April 2012 is close to b=1.0, and the aftershocks of the 20 May and 29 May sequences had b values of ~0.80. These values are typical for tectonic earthquakes, but some induced earthquake sequences also have similar values. Thus, the observed frequency-magnitude distribution of earthquakes in the vicinity of Cavone does not provide support either for, or against, a hypothesis of induced earthquakes. However, if an unusually high b-value is observed in the future, it might be taken as supporting evidence for an injection-related origin.

3.1.3 CAVONE PORE FLUID PRESSURES AND INJECTION VOLUMES

In considering the possibility of inducing an earthquake by fluid injection, we need to address the questions: Does the pore fluid pressure at the time and hypocentral location of an earthquake exceed the ambient pre-production pressure at this location, and therefore provide a potential causative link between the operations and the earthquakes? Or, alternatively, does production lead to a net decrease in pressure, thereby reducing the tendency of faults to slip? In addition to pressure changes, changes in the tensor stress caused by expansion or contraction of the reservoir may also be important; changes in the stress tensor may lead to changes in normal and shear stresses on potential rupture planes even in regions where the fluid pressure does not change.

Calculation of changes in pore fluid pressure and stresses in the region encompassing a reservoir requires a geomechanical model addressing both fluid flow and the resulting deformation. Relevant material properties such as permeability, porosity, and elastic moduli, as well as forcing from fluid injection or extraction must be included in the model formulation. Material properties are typically heterogeneous and measured directly only in a few locations, if at all. This makes *precise* inference of fluid pressures and stresses an intractable problem in practice. However, while precision is not possible, it is possible to place useful bounds on the fluid pressure changes and strains associated with injection and production.

Section 4 of this report describes in some detail our development of both analytical and numerical models of pressure and stress changes associated with production of hydrocarbons and injection of waste water in the region of the Cavone reservoir. In Section 4.1 we address information available about material properties from cores, injection tests , and measurements of pressure over the lifetime of the field. We also discuss how to extrapolate this near-surface information to regions of potential hypocenters.

In this section we summarize the results of an analytical model that provides reasonable upper bounds on the distribution of pressure changes at hypocentral depths at the time of the May 2012 earthquake sequence. Because the information is not practical to obtain, it is not possible to include details of spatial variations in properties in a regional model. However, because dimensions of open sections of wells are small compared to the distances and depths to these

earthquake sources, the results do not depend in an important way on these details. The analysis we present here represents injection and production zones as point sources and sinks in a halfspace overlain by an impermeable layer. We use the analytic solution of Wang (2000) modified for a half-space overlain by an impermeable layer. Because permeability can vary much more than viscosity, porosity, or compressibility, we hold the latter three parameters fixed at 0.4 mPa s, 3%, and 1.3 10^{-9} Pa^{-1}, respectively, and vary the permeability *k* between 0.1 mD and 3 mD.

Production and injection statistics for the wells in the field through June 2014 are given in Table 3.1.1. The top five producers, ranked by total volume of fluid produced, are wells Cavone 2 (temporarily closed), 13 (temporarily closed), 7, 17, and 4 (temporarily closed). Cavone 14 dominates the injection volume, with much smaller amounts injected at Cavone 11 and 5 (both permanently closed). From the monthly production values provided to us, we determined that between March 1980, and June 2014, almost 3.1 $x10^6$ m^3 of oil was produced in the Cavone field. Between January, 1993, and June 2014, over 3.1$x10^6$ m^3 of water was injected, with almost 3.2$x10^6$ m^3 of water produced. The net volume produced after subtracting the volume injected is 3.1 $x10^6$ m^3.

Because of its topical interest, we carried out an analysis of pressures at Cavone at the time of the May 2012 earthquakes. Between March 1980, and May 2012, over 2.9 $x10^6$ m^3 of oil was produced in the Cavone field. Between January, 1993, and May, 2012, 3.0$x10^6$ m^3 of water was injected, with 3.0$x10^6$ m^3 of water produced. Thus the net volume produced after subtracting the volume injected is 2.9$x10^6$ m^3. Figure 3.1.3 shows the results of the calculation of fluid pressures with this 3-D analytical model at the time of the May 29, 2012 earthquake. Calculated pressures at Cavone 14 and at the hypocenter are given in Table 3.1.2 for permeability ranging from 0.1 to 3 mD. The pressures at Cavone 14 are close to the observed values discussed in Section 4.1 for k=0.27 mD, somewhat too high for k = 0.2 mD and too low for k=0.3 mD.

Table 3.1.1 Production and injection time intervals and volumes (m^3)

Well	Start date	End Date*	Total oil production	Total H2O production	Total production	Total injection
Cavone 1	Jul-82	Jul-88	4,289	463	4,752	
Cavone 2	Mar-80	Dec-12	535,090	853,528	1,388,618	
Cavone 3	Mar-83	Jan-90	8,846	15,613	24,458	
Cavone 4	Jul-80	May-12	234,079	181,597	415,675	
Cavone 5	Mar-94	Sep-97			0	85,773
Cavone 7	Jun-82	Jun-14	506,975	241,372	748,347	
Cavone 8	Jun-81	Jun-14	86,700	253,622	340,323	
Cavone 9	Dec-80	Jun-14	640,466	329,911	970,377	
Cavone 10	Jun-83	Sep-93	8,908	1,798	10,706	
Cavone 11	Aug-82	Feb-98	22,697	8,761	31,458	254,056
Cavone 12	Nov-82	Oct-87	8,067	4,192	12,259	
Cavone 13	Jul-84	May-12	474,414	604,500	1,078,914	
Cavone 14	Jan-93	Jun-14			0	2,788,899
Cavone 15	Jun-87	Apr-95	15,904	31,441	47,345	
Cavone 16	Oct-87	Jun-04	70,871	142,363	213,234	
Cavone 17	Dec-87	Jun-14	293,247	405,123	698,371	
Cavone 19	Sep-87	Aug-02	121,412	23,643	145,055	
Cavone 21	Aug-88	Nov-89	1,805	4,723	6,528	
S. Giac. 1	Mar-01	May-12	18,243	82,770	101,013	
Total			3,052,013	3,185,420	6,237,433	3,128,729

* Data through 30 June 2014, with Cavone 7, 8, 9, 14, and 17 continuing activity.

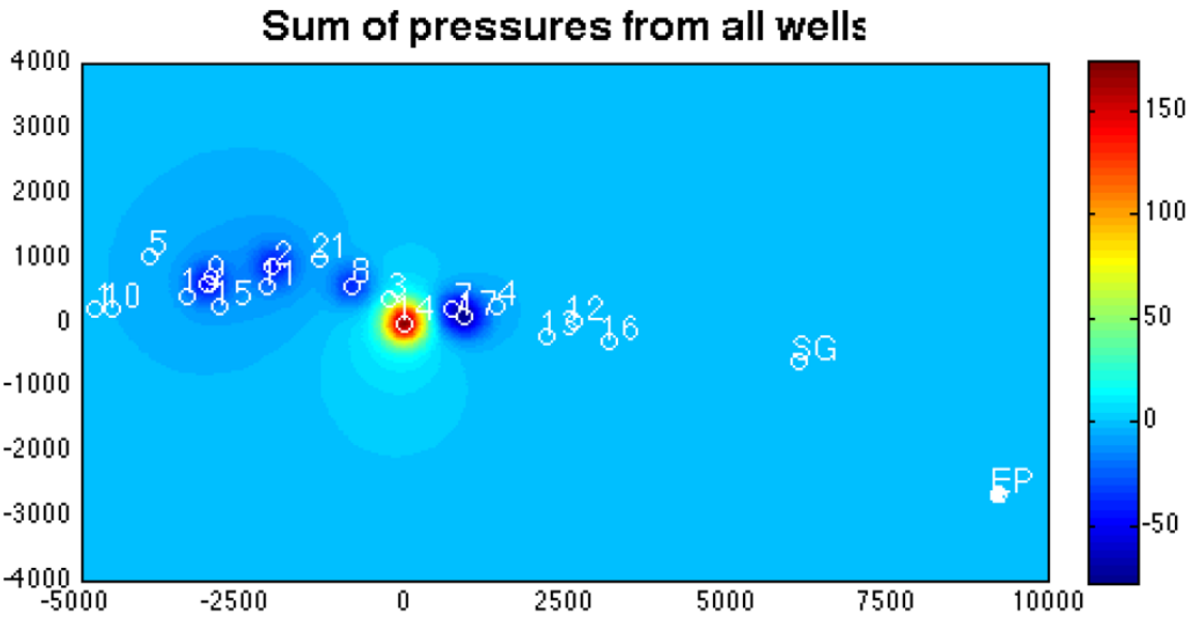

Figure 3.1.3: Calculated pressure field, May 29, 2012, at the top of the Cavone reservoir, assuming a uniform permeability of 0.2 mD. Well locations are given by the white circles, with the epicenter (EP) of the M_w5.8 29 May aftershock given by the asterisk. Axes are meters E and N of Cavone 14. Pressure is in bars.

Table 3.1.2: Calculated pressure changes at Cavone wells and 29 May hypocenter

Permeability (mD)	**P @ Cavone 14** (bars)	**P @ Cavone 2** (bars)	**P @ hypocenter** (bars)
0.1	815	-205	-0.3
0.2	282	-52	-0.4
0.3	151	-35	-0.3
1.0	22.1	-6.6	-0.1
3.0	3.0	-1.9	-0.04

Table 3.1.2 shows that, although the calculated pressure change at the wells is quite sensitive to the assumed permeability value, the pressure change at the hypocenter is not very sensitive at all. The pressure change is always negative because production is greater than injection, and therefore the net fluid flux driving pressure changes is negative. The magnitude of the pressure decrease at the hypocenter of the 29 May aftershock is always < 1 bar, while for the 20 May event, which was further away, the amplitude of the pressure decrease is always < 0.04 bars. For a given fluid flux, pressure at the well increases as permeability decreases. But the fall-off of pressure with distance is more rapid for lower permeability. The 29 and 20 May hypocenters are ~ 10 -30 km from the field; at these distances, the two effects approximately cancel, making the estimates of the small magnitude of the pressure drops

robust. Based on flow modeling, there is no reason to expect that production at the Cavone field triggered either event.

3.1.4 DID INJECTION AT CAVONE AFFECT THE COULOMB STRESS TRIGGERING OF THE 29 MAY 2012 EARTHQUAKE?

Although the currently available evidence indicate the 20 and 29 May earthquakes were not directly triggered or induced by operations at the Cavone oil field (section 2.5), we examine a possibility wherein pressure changes may have indirectly altered the time of occurrence of the 29 May earthquake. The question is this: Did injection of fluids at the Cavone field affect the triggering of the 29 May earthquake by Coulomb stress interactions from the 20 May 2012? This somewhat complicated scenario is based on the following points. 1) Available evidence indicates a tectonic origin for the 20 and 29 May 2012 earthquakes. 2) As discussed in section 2.5, the 20 May earthquake triggered the 29 May earthquake by Coulomb stress transfer. 3) Because the time delay between the 20 May and 29 May earthquakes depends on conditions at the hypocenter of the 29 May earthquake, it might be argued that small man-made perturbations of stress or fluid pressure altered the triggering in a way that substantially advanced the time of the second earthquake near the Cavone field. Because the direct change of stress due to production of fluids is negligible (section 3.2) the following considers only the effect of the change of effective normal stress by hypothetical pore fluid pressure changes at the hypocenter of the 29 May earthquake.

The space-time pairing of the two largest earthquakes in Emilia-Romagna sequence (M_w 6.0 20 May 2012 and M_w 5.8 29 May 2012) is a common characteristic of tectonic earthquakes (Kagan and Jackson, 1991) resulting from transfer of stress from the first earthquake to the fault where the next earthquake occurs. Pezzo et al. (2013) calculate a Coulomb stress transfer from the 20 May earthquake of about 6 bars on the Mirandola fault in the area where the 29 May earthquake nucleated (Section 2, Figs 2.5.4). That 6 bar Coulomb stress perturbation greatly exceeds any possible perturbation from injection or production of fluids. Because the 29 May earthquake rupture extended along the Mirandola fault to regions where the May 20 Coulomb stress change was negligible, west of the hypocenter, there can be little doubt the fault was critically stressed by tectonic processes prior to 20 May 2012. This together with continuing tectonic stressing of the region means the earthquake would have occurred at some time in the not-too-distant future if the triggering event (the 20 May 2012 earthquake) had not occurred.

In considering earthquake triggering (including aftershocks) the time delay between a triggering event and the occurrence of an earthquake can be understood as a time-dependent failure property of earthquake faults (Dieterich, 1994). As discussed previously in section 2.5 the rate- and state-dependent friction equations Eq. 3 effectively represent the time-dependent characteristics of fault slip and occurrence of earthquakes. Using these equations and solutions for earthquake nucleation based on the equations of Dieterich (1992, 2007) it is possible to evaluate the effects of hypothetical pressure changes from injection operations at

the Cavone field on the time of occurrence of the earthquake on the Mirandola fault. The appropriate calculation tracks the evolution of nucleation conditions (nucleation slip speed) at the 29 May hypocenter on the Mirandola fault. The procedure is to first work backward in time and through the Coulomb stress step of 20 May earthquake to infer nucleation slip speed immediately before the 20 May earthquake. Next the nucleation slip speed is adjusted to remove the effects of hypothetical pore fluid pressure perturbations, and then conditions are evolved forward through the stress step of the 20 May earthquake to find a new time of occurrence of the earthquake on the Mirandola fault.

A positive change of fluid pressure reduces the effective normal stress on the fault, which promotes fault slip. Hence, subtracting the effect of a positive pressure gives the later time when the earthquake would have occurred have occurred with no pressure increase (fluid pressure causes a positive clock advance for the earthquake). The opposite is true for production-related decreases of fluid pressure at the hypocenter — in the absence of a pressure change the earthquake occurred earlier (negative clock advance). The clock advance or delay for the earthquake on the Mirandola fault as a function of hypothetical pressure changes is illustrated in Figure 3.1.4.

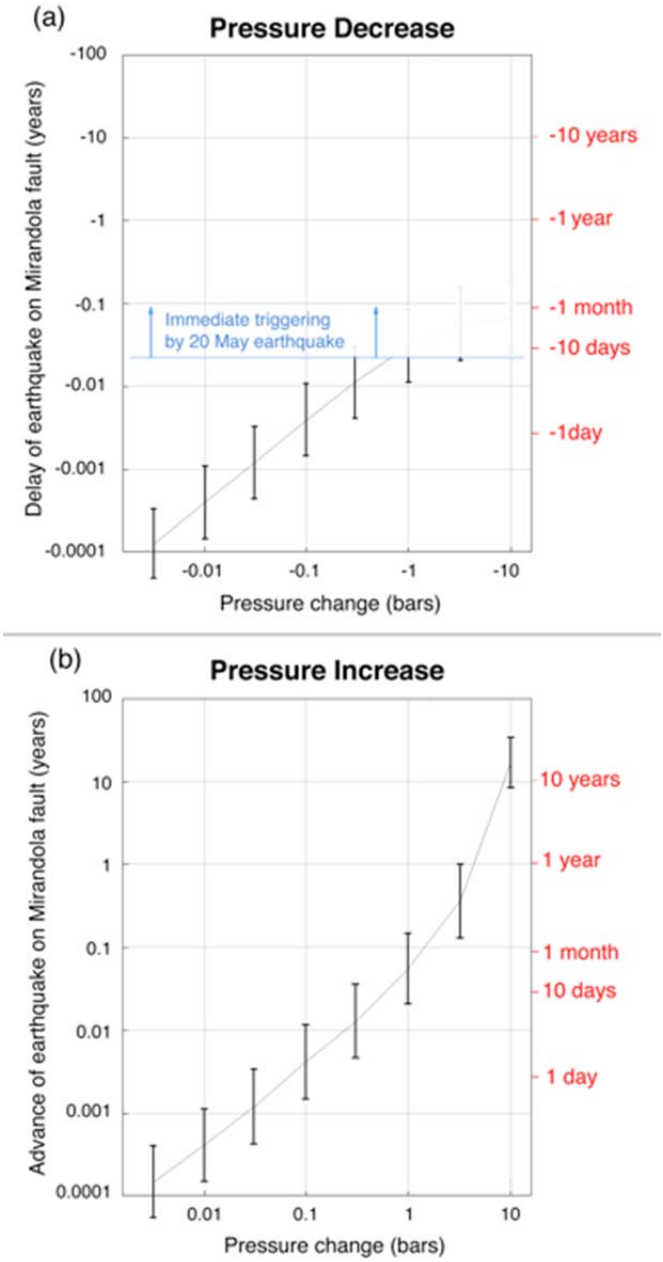

Figure 3.1.4: Clock advance or delay for the 29 May 2012 earthquake on the Mirandola fault due to hypothetical pore fluid pressure changes at the earthquake hypocenter. This calculation assumes a triggering stress in the range of 5-7 bars by the 20 May 2012 mainshock (Pezzo et al., 2013). The vertical bars give limits of clock changes obtained using a plausible range of values for the uncertain parameters used in the calculation. a) Effects of a decrease in fluid pressure due to oil production. A decrease of pressure means that production delayed the time of the earthquake (negative clock change). Delay greater than 9 days are not possible because the 20 May earthquake would have immediately triggered earthquake slip on the Mirandola fault. b) An increase of fluid pressure advances the time of the earthquake.

The results are sensitive to parameters used in the calculations. The vertical bars in Figure 3.1.4 give bounds for the clock change using a plausible range of values for the uncertain parameters. Because fluid production exceeded injection volumes at Cavone, it is much more likely that fluid pressures decreased somewhat at the hypocenter of the May 29, 2012 (M_w 5.9) and earthquake, which would have acted to delay the time of the triggered 29 May earthquake. A 0.1bar fluid pressure decrease would have delayed the earthquake by 0.53-3.9 days. Because the earthquake on the Mirandola fault was triggered by the large 5-7 bar Coulomb stress change from the 20 May earthquake, the most that a production-related

pressure increase could have delayed the earthquake is the ~ 9 day interval between the 20 May and 29 May earthquakes. Hence, if pressure decreased by ~1 bar, or more, due to production, then without production this calculation indicates the 20 May earthquake would have immediately triggered earthquake slip on the Mirandola fault.

As indicated by the preliminary pressure model, is appears highly unlikely that fluid pressure increased at the 29 May hypocenter due to injection. However, even if possible, a hypothetical 0.1 bar pressure increase at the hypocenter would have caused the Cavone earthquake to occur 0.6-4.2 days earlier than it would have without injection. A 1 bar pressure increase advances the earthquake clock by about 7.5 - 40 days.

3.2 INDUCED EARTHQUAKES BY POROELASTIC INTERACTIONS

Total fluid production at Cavone is about twice the volume of re-injected fluid. Hence, mechanisms for induced seismicity based on net fluid production may be relevant to Cavone operations. Using the theory of poroelasticity, Segall (1985, 1989) shows that net removal of fluids from a reservoir formation will result in volumetric changes that directly stress the region surrounding the reservoir (changes the τ and σ terms in equation 3.1.1). Segall (1989, 1992) and Grasso (1992) suggest this mechanism may be involved in a number of instances of seismicity near, or beneath large oil and gas fields worldwide.

The tectonic setting of the Cavone field and relative locations of May 2012 earthquakes are similar in many respects to several of the cases presented by Segall and Grasso. That is, the Cavone field is situated in a tectonically active fold and thrust fault complex and the earthquakes occurred near the field, but at somewhat greater depths. For a horizontal reservoir the region beneath a producing oil field is put into horizontal compression, while the regions at the same depth as the reservoir are put into horizontal extension. Hence, the applicability of the poroelastic stress for the Cavone field and thrust mechanism earthquakes (including the large May 2012 events) depends upon their locations relative to the oil field.

With this mechanism the Coloumb stress changes that induce earthquakes are directly related to volumetric changes of reservoir compaction. Those stresses are roughly proportional to pressure changes in the reservoir. Generally, the poroelastic stresses favoring thrust faulting beneath a reservoir are less than ~5% reservoir pressure decrease. Like all stress perturbations driven by a local source, these effects decay rapidly with distance from the source. For example, with the seven cases examined by Grasso (1992) the maximum stress change at the depths of the earthquake ranges from 0.4% to 2.8% of reservoir pressure change. Because the magnitudes of these stresses are very small compared to the stress relaxation that occurs at the time of earthquakes (on the order of one percent or less of the earthquake stress drop), Grasso (1992) and Segall (1992) both conclude this mechanism can be effective in inducing earthquakes only if the region is already essentially at the critical stress to produce an earthquake. Hence, this mechanism appears to be a contributing factor to the stressing of the

fault that might advance the time of occurrence of a tectonic earthquake, not the dominant cause. In the case of the May 2, 1983 Coalinga M=6.4 earthquake Segall (1985) estimates that poroelastic effects possibly advanced the time of the earthquake by 1-2 years or 10-20 years (depending on assumptions of the tectonic stress rates).

3.2.1 COULOMB STRESS CHANGES FROM PRODUCTION OF THE CAVONE RESERVOIR

The net production volume at Cavone (total production less re-injected water) is approximately ~$3x10^6 m^3$ as of May 2012, which is much smaller, by factors ranging from 1/67 to 1/400, than production volumes for the cases examined by Grasso and Segall. Consequently the poroelastic stress changes around Cavone are expected to be much smaller than the already small stress changes in the examples cited by Grasso and Segall.

Analytical calculations of the stress changes induced by production of reservoirs and their effects on triggering earthquakes (e.g., Segall, 1989; 1992) are typically done by integrating the so-called Geertsma source (Geertsma, 1973a) – the Greens function for contraction of an infinitesimal element over the volume of the reservoir. Although it is not well recognized, the Geertsma source is identical to the well-known "Mogi source" used in the volcanological community. Coulomb3.3, the USGS software package for calculating changes in Coulomb stress, includes the Mogi source as an option.

As previously discussed, the net production volume of fluids at Cavone to May 2012 was $3x10^6$ m^3 at a reservoir depth of ~ 3 km. The appropriate volume to use in the calculation of Coulomb stress change is the resulting change in volume of the reservoir, which is given by the product of Skempton's coefficient *B* times the change in fluid volume. For a typical sandstone $B \sim 0.5$ (Wang, 2000), suggesting a change in reservoir volume of 1.5 10^6 m^3.

The leading order terms in stress for a Geertsma/Mogi fall off as $1/R^3$, where R is the distance between the volume source and the fault. For the 20 May main shock, R > 20 km, so the details of reservoir geometry are unimportant and one can assume that the reservoir behaves as a point source. At the hypocenter of the 20 May main shock the Coulomb stress changes on the fault plane are positive as the result of slightly decreasing the normal stress. The maximum Coulomb stress change in the cross section through the hypocenter is < 0.005 bars, while the Coulomb stress change at the hypocentral depth (5 km) is less than a millibar! Changes in stress from the tides (e.g., Lambert et al., 2009) and even the loading of the atmosphere are larger than this, leading to the strong conclusion that poroelastic stress changes associated with production of the Cavone reservoir are negligible for triggering the mainshock.

Closer to Cavone field, the magnitude of the normal stress change on the fault increases. However, the sign changes, giving a reduction in Coulomb stress on the fault plane of the 29

May aftershock. This is because contraction of the reservoir leads primarily to a decrease in shear stress on thrust faults to the north of the field, promoting normal, not reverse slip. This means that the production of the Cavone field tended to limit the size and/or delay the of the 29 May aftershock.

3.3 INDUCED EARTHQUAKES BY ISOSTATIC RECOVERY

A mechanism inducing earthquakes by isostatic recovery was proposed by McGarr (1991). The central idea is that fluid production from a field results in removal of mass that stimulates an isostatic adjustment in the form of an earthquake.

To quantify this concept McGarr first derives an expression for the amount of crustal thickening needed to isostatically balance the mass removal from production — the concept here is that thrust faulting beneath the reservoir acts to effectively thicken the low density crust that is "floating" on the denser mantle. He then uses this result to determine the equivalent earthquake moment required to restore the isostatic conditions that existed prior to mass removal by fluid production.

$$M_0 = \frac{2G\Delta m\gamma}{\rho_c} \qquad \text{Eq. 5}$$

where G is the shear modulus, Δm is the mass change, ρ_c is average crustal density and γ is the fraction of the crust that is seismogenic.

McGarr examines three earthquakes that occurred beneath producing oil fields (Coalinga 1983, Kettleman N. Dome 1985, Whittier Narrows 1987). In each of these cases the moment required for isostatic compensation (Equation 5) agrees quite closely with the moments of the earthquakes (individual and summed moments of the associated sequence are all within 12% and 29%, respectively of the buoyancy moment). McGarr takes this result as confirmation of the proposed mechanism — in fact he states that a failure to match the moments would invalidate the application of his theory to those earthquakes.

Using the McGarr model (Equation 5) the equivalent moment of mass removal at Cavone, to the time of the 2012 earthquakes, is about $M_0 = 4.1\text{x}10^{16}$ Nm. The total seismic moment release in the vicinity of Cavone is dominated by of the M_w 6.0 20 May 2012, and M_w 5.8 29 May 2012 which have moments of $1.0\text{x}10^{18}$ Nm and $5.0\text{x}10^{17}$ Nm, respectively. Hence, the earthquake moments individually exceed the buoyancy moment by factors of 24 and 12 for the M_w 6.0 and M_w 5.8 earthquakes, respectively. The factor increases to ~50 for the summed moments of the entire May 2012 sequence. According to the criteria defined by McGarr

(1991) this mechanism could not responsible for earthquakes in the vicinity of the Cavone field.

We calculated the change in Coulomb stress resulting from the removal of mass by production in the Cavone field provides to obtain a more quantitative analysis of this mechanism. Mindlin (1936) gives analytic expressions for stresses and displacements resulting from a point force in the interior of an elastic halfspace. We used these expressions to calculate the change in Coulomb stress at the location of the M=5.8 May 29 aftershock. Because the hypocenter of the aftershock is 8.7 km ESE of the Cavone 14 well and at a depth of 10.2 km, almost 7 km deeper than the injection and production levels, approximating the mass removal as a point force load is adequate. We take the net mass change (production – injection) as 2.4 Mtonne, and the fault strike and dip as 95° and 45° respectively (Pezzo et al., 2013). This unloading leads to an increase of Coulomb stress at the hypocenter of 9 Pa (0.09 millibars). This is an extremely small stress change, smaller than daily variations in atmospheric pressure.

The small stresses we obtain highlight a fundamental problem with the McGarr model. As first noted by Segall (1985) the direct stressing effect due to mass removal is negligible compared to poroelastic effects. In turn the poroelastic stresses are small compared to the pore fluid pressure effects. The stress changes considered by McGarr for other oil fields are more than a factor of 10 larger than the Cavone result, but still too small relative to earthquakes stress drops to be considered relevant to inducing earthquakes.

3.4 INDUCED SEISMICITY BY THERMO-ELASTIC STRESSING

For completeness, we have also examined induced seismicity due to thermo-elastic stressing resulting from injection of cold water into hot rocks. By this mechanism the cooling due to extraction of hot fluids and re-injection of cooler water into reservoir rocks causes thermal contraction, which induces stress changes within the reservoir and surrounding regions. The volume changes from temperature changes of ~ 1° C are comparable to those caused by pressure changes of ~ 2 bars.

The thermoelastic mechanism has been proposed to be the primary cause of extensive induced seismicity observed at the Geysers geothermal field in northern California, USA (NRC 2012). At the Geysers, the seismicity is closely associated both spatially and temporally with the injection wells (Figure 3.4.1). To date the maximum magnitude of induced earthquakes at the Geysers is M 4.6. In contrast to the earthquakes at the Geysers geothermal field, clustering of earthquakes near the injection well at Cavone is completely absent.

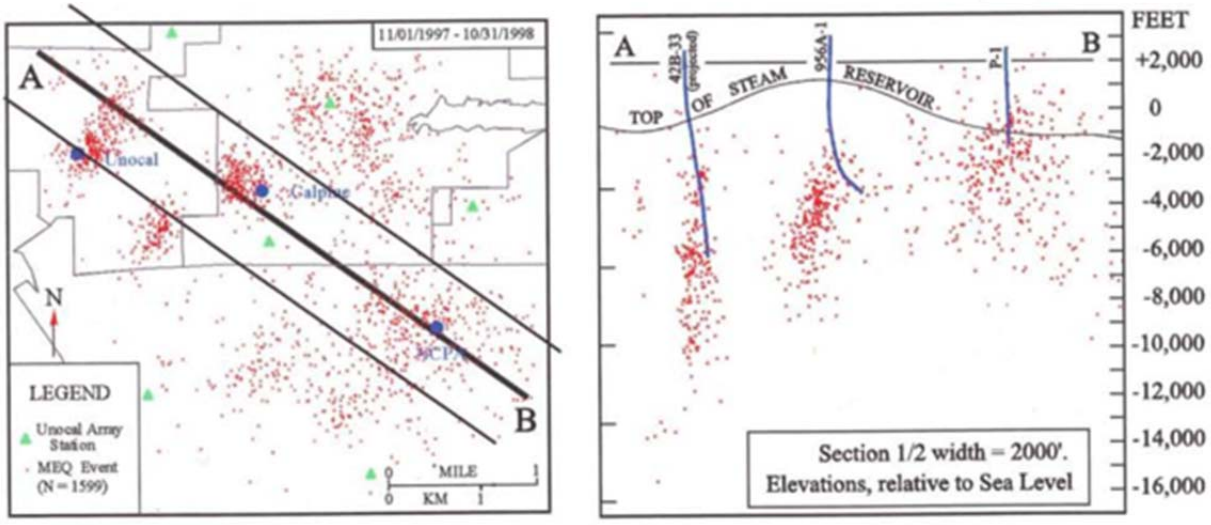

Figure 3.4.1: Seismicity at the Geysers geothermal field, which is located in northern California, USA. Left panel is map of showing location of injection wells (blue) all located earthquakes 1997-1998 (red) and line of cross section. Right panel is cross section showing injection wells and depth locations of earthquakes. Figures from NRC, (2012), source: Beall et al. (1999).

From Table 3.1.1, 2.9 10^6 m^3 of water was injected into the Cavone field. The temperature at the top of well Cavone 14 is ~ 25° C, while the temperature at the well bottom is ~ 50° C. There is a net cooling of the region surrounding the Cavone 14 injection well because the injected water is about 25 °C cooler than the ambient formation. Assuming a porosity of 3%, 2.9 10^6 m^3 of water would occupy 0.09 km^3 of rock, equivalent to a cylinder centered on the well of height 100 m and radius 500 m. Assuming a density of 2.5 g/cm^3 and a specific heat of 0.22 cal/(g °C) leads to a cooling of the rock mass by 1.4 °C. For a volumetric thermal expansion coefficient of 2.4 10^{-5}/°C, the rock surrounding the well would contract by 3.4 10^{-5}, or 0.0034 %, giving a volume reduction of 3 $10^3 m^3$.

Thus, thermoelastic effects at Cavone are much smaller than the poroelastic effects at Cavone and can be safely ignored.

3.5 CONCLUSIONS

- *Because injection volumes at Cavone are about half the total fluid production volume, and because injection pressures have been held close to the pre-production field pressures, our models strongly indicate decreases of the average fluid pressures in the vicinity of the field. Increases in fluid pressures occur near the injection wells, but they are highly localized to distances within 1 – 2 km from the injector wells.*

- *Comparisons of the space-time patterns of earthquakes in the vicinity of the Cavone oil field with known cases of induced earthquakes do not support an injection-related hypothesis for past earthquakes.*

- *Clock changes due to fluid pressure changes that may advance or retard the time of tectonically driven earthquakes appear to be negligible in the areas of the May 2012 hypocenters .*

- *The change in Coulomb stress at the hypocenter of the 20 May mainshock resulting from production-induced compaction of the Cavone reservoir has a magnitude (~0.001 bar) a factor of 100 smaller than the accepted minimum value for triggering of earthquakes by static stress changes and a factor of 10-20 smaller than fluctuations of stress by earth tides. Closer to the Cavone field, changes in Coulomb stress on the rupture plane of the main aftershock of 29 May resulting from production-induced compaction of the Cavone reservoir are in a sense to inhibit failure.*

- *Changes in Coulomb stress due to both production-induced decrease in weight of the Cavone reservoir (the "isostatic effect"), and the thermoelastic contraction from injection of cool fluids into the warmer reservoir formation are negligibly small compared to the already very small stresses from poroelastic compaction.*

4 INTERPRETATION OF INJECTION TESTS AND RESERVOIR MODELING

In considering the possibility of triggering or inducing earthquakes by fluid injection and withdrawal, we need to address the questions: Does the pore fluid pressure at the time and location of an earthquake exceed the ambient pre-production pressure at this location by an amount large enough to provide a possible causative link between the operations and the earthquake? Or, alternatively, does production lead to a net decrease in pressure, thereby reducing the tendency of faults to slip? What are the changes in Coulomb stress, including both the effects of fluid pressure variation and the stresses resulting from expansion or contraction of the reservoir? Answering these questions requires a model of porous flow both within the reservoir, as well as in surrounding regions that are in hydraulic communication with the reservoir, along with a geomechanical model.

Pressure changes associated with production and injection of fluids in a porous medium are governed by a diffusion equation (e.g., Wang, 2000):

$$\frac{\partial p}{\partial t} = \kappa \nabla^2 p + {Q}/{\varphi c} \qquad \text{Eq. 6}$$

Here the diffusivity, $\kappa = k/(\mu\varphi c)$, where k is the permeability, μ is the pore fluid viscosity, ϕ is the porosity, and c is the total compressibility of the pore fluid plus matrix. Q is the rate of volume of fluid injected. Note that the diffusion equation for pressure is isomorphous to the diffusion equation for temperature that governs heat transport in a solid.

In diffusion problems, the characteristic distance, d_c, that a disturbance propagates over some characteristic time, t_c, is given by:

$$d_c = \sqrt{4\kappa t_c} = \sqrt{\frac{4kt_c}{\mu\phi c}} \qquad \text{Eq. 7}$$

Characteristic times for the Cavone field range from days, for variations in production volumes and well tests, to decades - the lifetime of the field. As discussed in Section 4.1, typical effective values of permeability, viscosity, porosity, and compressibility, are about 1 mD, 0.4 mPa s, 3%, and 1.3 10^{-9} Pa^{-1}, respectively. For these parameter values, κ = 0.062

m^2/s. For this value of κ, pressure diffuses about 150 m in one day, 400 m in one week, 3 km in one year, and 10 km in a decade.

In order to calculate the pressure field, we need to know the spatial variation of κ (i.e., of k, ϕ, μ, and c) and the distribution in space and time of the sources and sinks of fluid injection, Q (the wells). Although we have production and injection records, there is little information available about the three-dimensional distribution of κ. Therefore we use the available information about the geologic structure, as well as matching the available pressure data for injection, particularly at well Cavone 14, to estimate plausible variations in effective κ that govern the distribution of pressure.

We begin by considering the geologic structure and stratigraphy. Figure 4.0.1 shows the stratigraphic section intersected by each of the wells in the Cavone field. Measurements of porosities and permeabilities for most of the units were made available (cavone oilfield table_rev1.xlsx). There is wide range in these properties. In the following we indicate the range and median in the format (minimum - maximum, median). The Scaglia Calcarea (not shown Figure 4.1, see Figure 4.2) provides the caprock for the reservoir. Although its permeability is not reported, because it is the cap rock we assume that it must have a very low permeability. The Marne Del Cerro formation (tan) has porosity range (0.01 – 5.0%, 1.8%) and permeability range (0 - 6.4 mD; 0.2 mD). The Brecce di Cavone (red) is a reservoir unit, with porosities (0.01 – 20%, 2%) and permeabilities (0 – 410 mD, 1 mD). The Maiolica, Malm, and Dogger (green) are tight rocks, with porosities (0.01 – 3%, 1%) and permeabilities (0 - 13 mD, 0.1 mD). The underlying Calcari di Noriglio reservoir is divided into several layers: Oolitico (red), with porosities (0.01 – 5%, 1%) and permeabilities (0 – 1.6 mD, 0.2 mD); Noriglio A (blue), with porosities (0.01 – 5%, 1%) and permeabilities (0 – 3.2 mD, 0.3 mD); the radiogenic Marker unit (purple), with porosities (0.01 – 5%, 1%) and permeabilities (0 – 3.2mD, 0.4 mD); and Noriglio B (yellow), with porosities (0.01 – 5%, 1%) and permeabilities (0 – 26 mD, 0.8 mD).

For comparison, a summary of parameters determined from mechanical core tests and cuttings, taken from the report on the Cavone Laboratory interference/injectivity tests (*Risultati del Programma di Prova di interferenza/iniettività*), is given in Table 4.0.1. There is substantial variation in the porosities and permeabilities obtained from these two sources, probably indicative of substantial heterogeneity in the distribution of these parameters.

Table 4.0.1: Representative flow parameters for Cavone field

Formazione	Porosità media %	Spessore netto m	Spessore medio m	Permeabilità media mD	Note
Brecce	5--23	0,75--17	11--105	100--1000	non presente ad Est
Maiolica	3--20	0,3--25	ND	5--55	Non presente ai pozzi 14-7-17
Malm	1--5	1,0--19,5	ND	ND	Spessore che aumenta verso Ovest
Dogger	3--7	2,5--20	ND	1--60	Spessore che aumenta verso Ovest
Oolitico	1--7	0,6--11	10	20--40	
NOR-A	1--3	10--39	120	2--20	
NOR-B	1--3	9--122	ND	2--20	

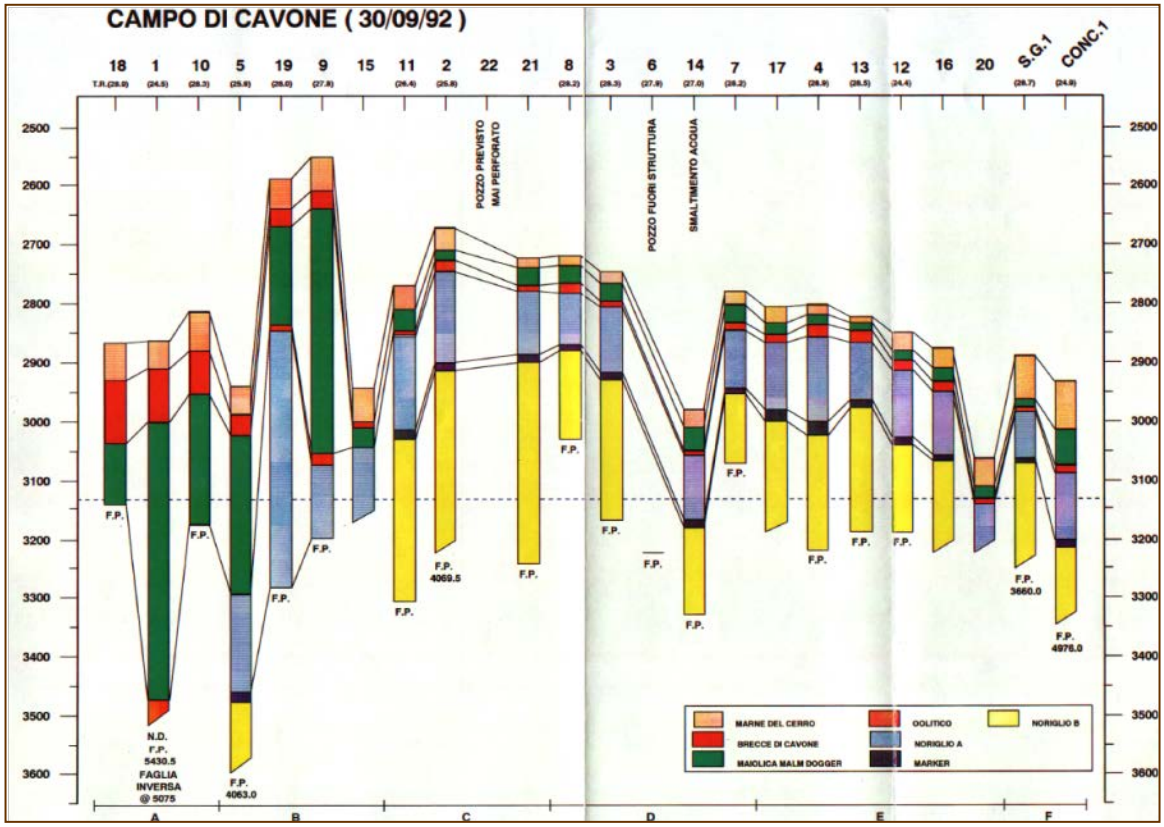

Figure 4.0.1: Stratigraphic columns and correlation for wells in the Cavone field.

Figure 4.0.2 is a cross section through the Cavone 2 well, the most prolific production well in the field. As can be seen, the well bottoms in the Noriglio B formation, which extends at least 600 m beneath the oil-water interface. Similar structure and stratigraphy applies to the other important wells.

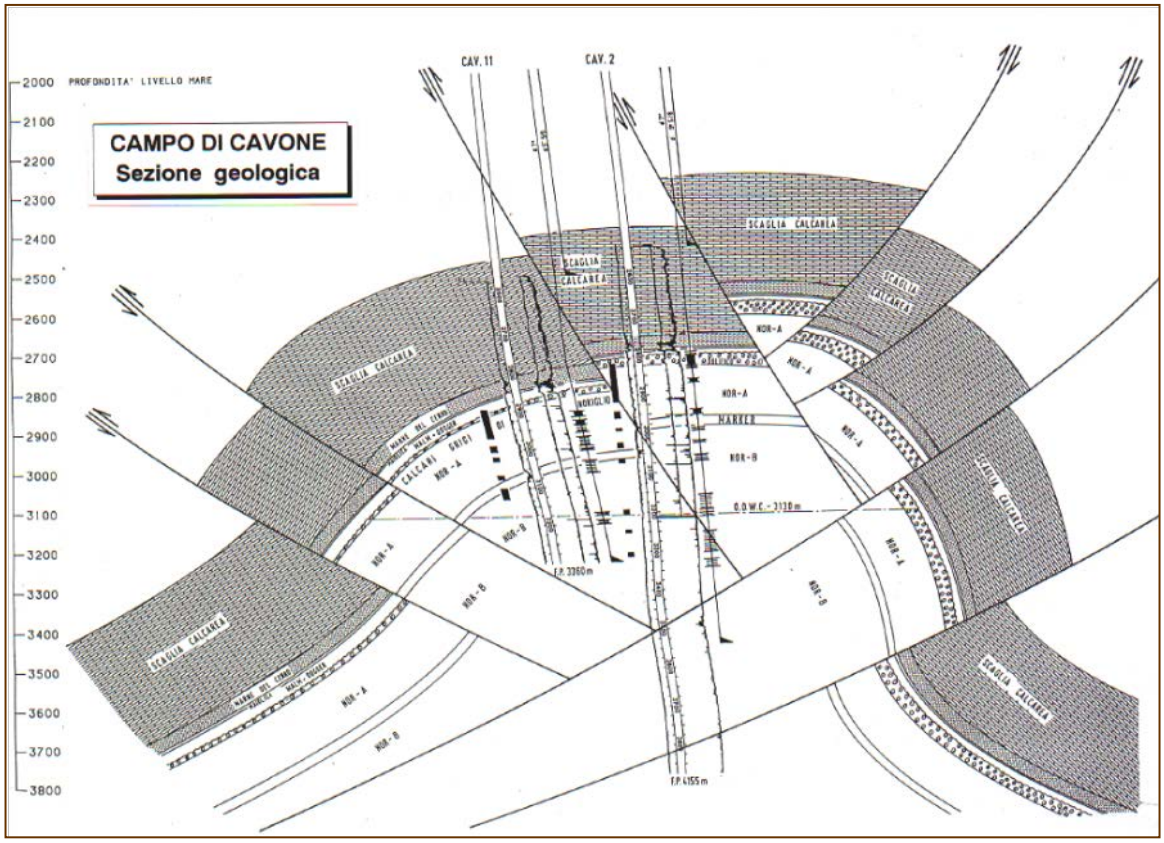

Figure 4.0.2: Cross section through wells Cavone 2 and 11.

Records of pressures, along with production and injection rates, can be used to infer effective properties on spatial scales applicable to the near-well region, to the reservoir, and to the surroundings to estimate the hydrologic properties of the regions deeper than 3900 m. Thus, the relation between pressure and sources of fluid volume in Eq. 6 provides a key constraint on the average properties of the reservoir beneath the caprock.

Records of pressure variations for injection well Cavone 14 at time scales of minutes to days were obtained as part of the interference/injectivity tests carried out over 32 days beginning 13 May 2014. On day 1, injection was ended and well-bottom pressure and temperature gauges installed. Injection began again on day 8 at a constant rate of 600 m^3/day for 96 hours. The injection was then stopped until day 31. Production at wells Cavone 7, 8, and 17 was also monitored to see if any interference was observed. These wells are at distances of 581 m, 946 m, and 810 m, respectively from Cavone 14. No interference was reported, placing constraints on the permeability of the region between these wells.

The variation in bottom well pressure measured during this test is shown in Figure 4.0.3. Pressure dropped in response to cessation of injection, increased during the 96-hour injection phase, and dropped again during the remainder of the measurement period.

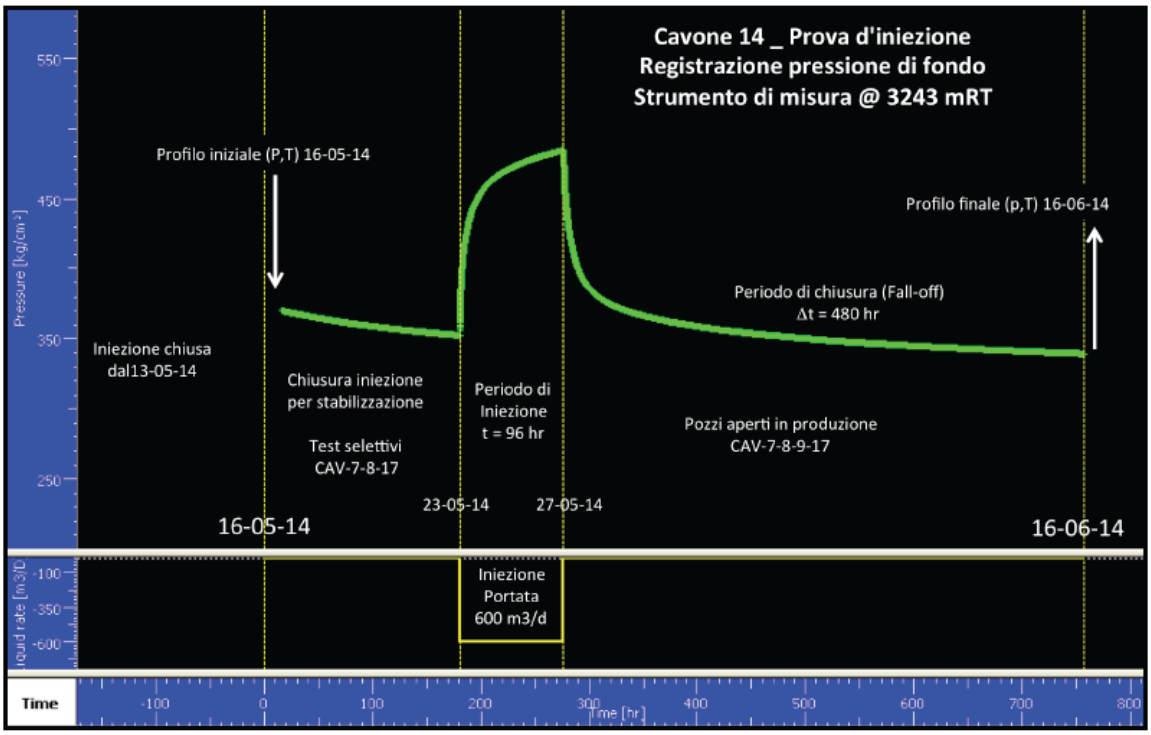

Figure 4.0.3. Detailed record of bottom hole pressure in Cavone 14 during the interference/injection test. Injection was stopped on 15 May, 2014, and kept off except for the 96-hour window from 23 – 27 May, when 600 m3/day was injected.

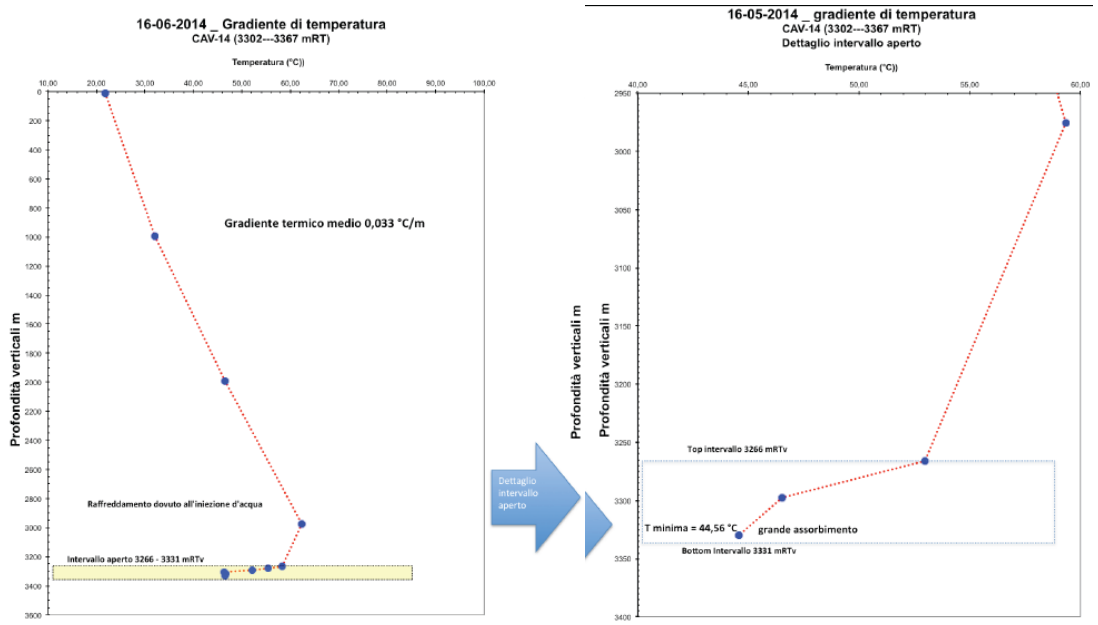

Figure 4.0.4. Profiles of temperature in Cavone 14 as a function of depth below the surface. a) Entire well. b) Zoom in on the region near the bottom of the well.

The measured variation of temperature with depth from the surface to within 1 m of the bottom of the Cavone 14 well is shown in Figure 4.0.4a, with a zoom of the bottom part of the well shown in 4.0.4b. For most of the depth, the temperature profile increases with depth along the geotherm. In the injection region, the surrounding rock has been cooled by the injection of cooler water, so the temperature profile decreases with depth. Interestingly, this temperature inversion is not symmetric across the injection interval. This temperature profile provides evidence that rock beneath the end of the well is being cooled by injection.

The response of the pressure at the well to the effective permeability structure at the scale of kilometers can be constrained by longer-term measurements. We have good records of pressure at the well head and fluid flux for injection well Cavone 14, where we have daily values over a > 15-year long interval between April 1, 1999, and June 30, 2014. (We have monthly figures over the longer interval given in Table 3.1.1.) The volume of water injected daily is shown Figure 4.0.5a, which shows that the daily injection was, except for minor exceptions, capped at 600 m^3/day. However, although not apparent on this plot, there were many days in which no water was injected. The longer term variability in injection rate is more apparent when monthly injection rates are plotted over the same time span in Figure 4.0.3b. The daily record of injection pressure at the well head (338 bars lower than the pressure at the well bottom) is shown in Figure 4.0.3c. From 2004 – 2008, the monthly injection rate was approximately 16,000 m^3/month, with the pressure remaining fairly steady at ~ 200 bars. During 2009 – 2012, the injection rate was usually 600 m^3/day when injection was carried out, but injection did not occur on roughly 1/3 of the days. Because the average injection rate was lower during this time, with the average monthly injection rate approximately 10000 m^3/month, the average pressure also dropped, to ~ 160 bars. Because of the diffusive nature of porous flow, the pressure varies less rapidly than the injection volume. From this information, we expect that an excess average pressure of approximately 160 bars at Cavone 14 provides a good calibration for the flow model that we use to estimate pressures at regional scales, including the calculations reported in Section 3.1.3.

In addition to the pressure records at Cavone 14, there is sparse information about the pressures at the producing wells at times when production was stopped, e.g., for maintenance operations. Maximum decreases in pressure associated with production are up to 15 – 20 bars.

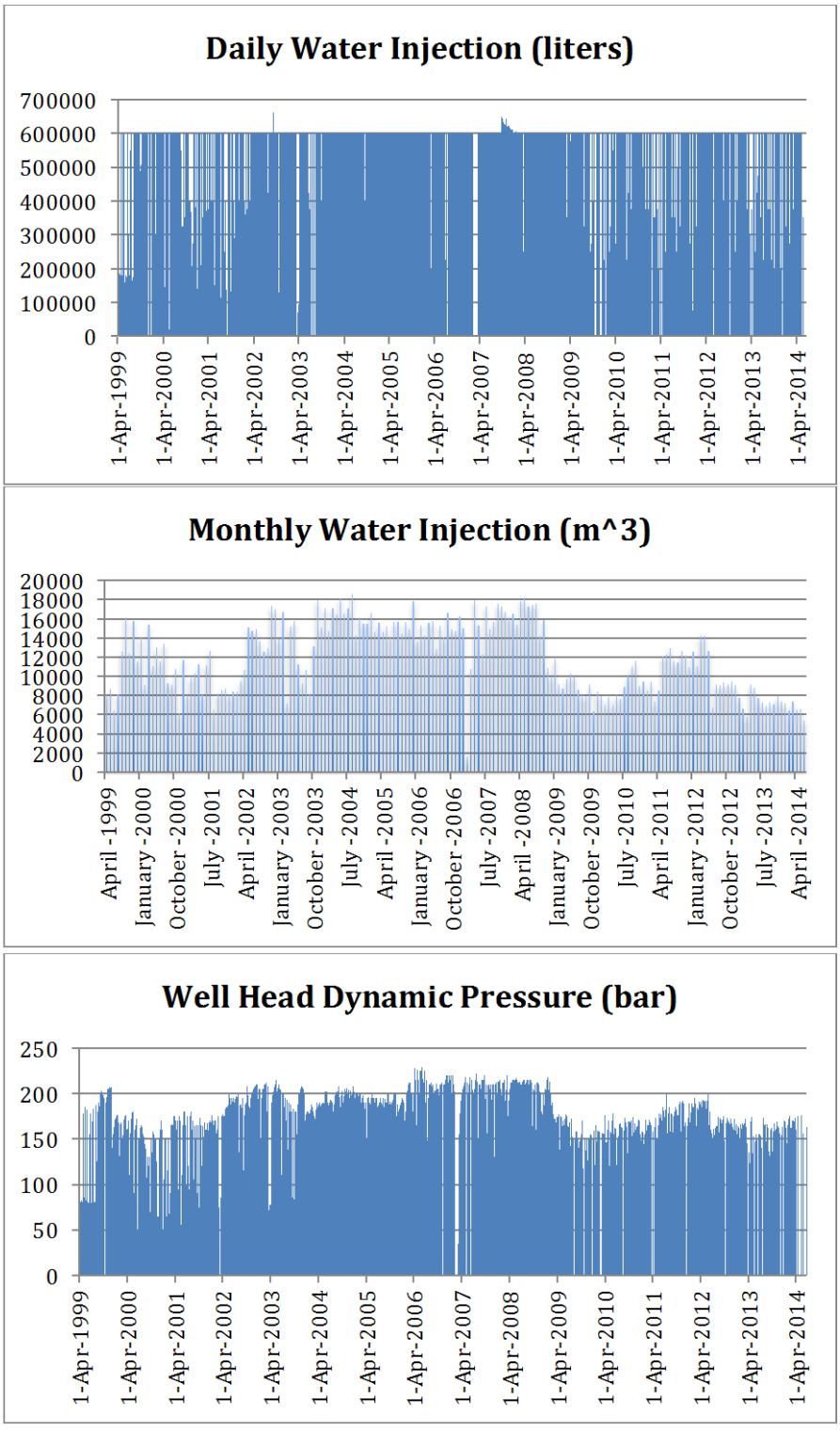

Figure 4.0.5: a) Daily record of the volume of water injected into the Cavone 14 well between April 1, 1999 and June 30, 2014, b) Corresponding monthly record of the volume of water injected into the Cavone 14 well, c) Corresponding daily record of the reinjection pressure at the Cavone 14 well head.

4.1 Inference of Effective Permeability over a Range of Spatial and Temporal Scales

In this section, we first discuss the report of results of the interference/injection test carried out in May – June, 2014 (*Risultati del Programma di Prova di interferenza/iniettività*), then test the properties inferred by comparing to the longer-term record of pressure variations associated with production and injection. We use analytical models that assume a diffusivity structure that is either uniform or varies in at most three regions centered on the injection well. We investigate the effects of varying the assumed diffusivity on the calculated pressure field, both in the reservoir and at distances up to 10's of km from the reservoir.

Fluid is injected in the Cavone 14 well in a 65 m thick zone of open well in the Noriglio B unit between 3266 and 3331 m depth. The injection test lasted 4 days; using the example diffusivity given above, the pressure perturbation from injection might be expected to penetrate ~ 250 m during this test – a distance about four times the length of the injection zone. The nominal reference model used in interpreting injection tests is that due to Theis (1935). This hydrological model assumes that the well penetrates completely through a reservoir of thickness, *H*. The problem is assumed to have cylindrical symmetry, with the axis at the center of the well.

For the Theis solution, the change in pressure, *p*, at time, *t*, resulting from fluid injection at a rate, *Q*, as a function of distance, *r*, from a the center of a well is:

$$p(r,t) = \frac{\mu Q}{4\pi kH}\mathrm{Ei}(x);\ x = \frac{\phi\mu c r^2}{4kt} \qquad \text{Eq. 8}$$

where k is the permeability, μ is the pore fluid viscosity, ϕ is the porosity, c is the total compressibility of the pore fluid plus matrix, and Ei(x) is the exponential integral. The asymptotic expansion Ei(x) = log(1/x) is accurate for x < 0.01.

The pressure history plotted in Figure 4.0.3 is analyzed in some detail in the document *Risultati del Programma di Prova di interferenza/iniettività*. The curve can be matched well during both the injection and fall-off phases using a model with three permeability regimes. The response early in the transient phase can be matched by including a negative geometric skin effect as would result from fractures intersecting the well, making the effective permeability larger than the nominal value. A dual porosity model explains the behavior in the interval 2 – 96 hours after the beginning of the transients. The behavior of the evolution of pressure at times of several days to weeks is approximately that expected for the Theis model with parameter values close to those that we have already mentioned. Effective values of permeability, viscosity, porosity, and compressibility, are about 1.1 mD, 0.4 mPa s, 3%, and 1.3 10^{-9} Pa^{-1}, respectively. But at the latest stages of the fall-off phase, the pressure falls

off more slowly than predicted by Eq (4), which the report attributes to a geometric constriction of flow on three sides at a distance of approximately 500 m from the injection well. Although this model explains the observations in the time window of the tests, it is not unique. For example, a radially symmetric decrease in permeability by a factor of 4 at a distance of about 500 m could also explain the observations.

The next test of internal consistency is to determine whether the Theis model, using the parameters inferred from the interference test, is consistent with the pressure and injection records in Table 3.1.1 and Figure 4.0.5. Because the pressure predicted by the Theis equation varies as $\log(1/r^2)$ in the vicinity of the well, and because the injection and fall-off tests show large effective permeability near the well, we need to take this near-well high effective permeability into account. We do this by calculating an effective well radius that satisfies the pressure increase of 132 bars observed after injecting 600 m^3/day for 96 hours. The resulting value of the effective well radius is 30 m.

Using the injection volume given in Table 3.1.1 for Cavone 14, 2.8 10^6 m^3 injected over 21 years, gives an average monthly flux of 8,000 m^3/month, very close to the average monthly injection of 8,066 m^3/month between 1 June, 2012 and 30 June, 2014. Using a permeability of 1.1 mD, as inferred from the 96-hr long injection test, Eq (3) predicts that after 21 years of injection, the pressure at 30 m distance from the axis of the well is 174 bars, dropping to 27 bars at a distance of 5 km from the well. Using a permeability of 0.27 mD, as inferred from the pressure change several weeks into the fall-off test, Eq (3) predicts that after 21 years of injection, the pressure at 30 m from the axis of the well is 616 bars, dropping to 41 bars at a distance of 5 km from the well. A dynamic pressure at the well of 174 bars is consistent with typical values of the pressure shown in Figure 4.0.5, but a dynamic pressure of 616 bars is much too large. The conflict between the permeability needed to model the 3-week-long fall-off test and the 3-decade-long injection history suggests that the flow model could be improved. For this reason, we develop a more realistic numerical model in section 4.2.

In addition, the temperature profile in Figure 4.0.4 suggests that water is flowing into the region below the well. Certainly the geologic model shown in Figure 4.0.2 suggests that the Noriglio B formation extends far below the bottom of the injection interval. Because the open interval of the injectin well is much smaller than the thickness of the Calcari di Noriglio formation, a more appropriate model for the Cavone reservoir treats the injection as a point source in a halfspace overlain by an impermeable layer. Wang (2000, p. 112) gives the formula for the pressure in a uniform, infinite domain at time, t, and distance, R, from an instantaneous injection of a slug of finite volume V at t=0 and R=0. By symmetry, no fluid flows through a plane passing through the point source. Since in Wang's formulation, half of the fluid flows upward and half downward, we can obtain the formula for injection/production at the surface of a halfspace overlain by an impermeable layer by doubling the volume, V, in Wang's expression, obtaining:

$$p(R,t) = \frac{V}{4\varphi c(\pi\kappa t)^{3/2}} exp\left(-\frac{R^2}{4\kappa t}\right) \quad \text{Eq. 9}$$

The pressure field resulting from injection at a constant rate Q, beginning at t = 0, can be found by integrating this impulse response:

$$p(R,t) = \frac{0.1593Q\mu}{kR} erf\left(\frac{R}{\sqrt{4\kappa t}}\right)$$

Using a permeability of 1.1 mD, as inferred from the 96-hr long injection test, Eq (9) predicts that after 29 years of injection, the pressure at 30 m from the axis of the well is 42 bars, dropping to 0.4 bars at a distance of 5 km from the well. Using a permeability of 0.27 mD, Eq (4) predicts that after 29 years of injection, the pressure at 30 m distance from the axis of the well is 167 bars, dropping to 1.7 bars at a distance of 5 km from the well. Thus, for injection into a thick aquifer, the pressures associated with the record of long-term injection over 3 decades are consistent with the permeability inferred from the fall-off test lasting 3 weeks.

In summary, the permeability structure of the Cavone field and surrounding region can be constrained by geologic structure and by records of injection rates and corresponding pressures over time scales of minutes to decades. On time scales of minutes to days, the interference/injection tests show clear evidence for the influence of fractures and dual porosity. But on time scales of weeks to decades, these complications are not needed to match the observations. There is evidence from the temperature profile in well Cavone 14 that injected water is penetrating the formation beneath the bottom of the injector, suggesting that flow is not confined to a layer of the same thickness as the open section of the well. A model that includes flow into the formation below the well can explain the long-term pressure records.

Although the simple models presented in this section are robust enough to support the conclusion that pressure perturbations associated with production and injection are small at distances comparable to the dimensions of the field, they are not adequate to predict pressure perturbations in regions within several km of the field. In order to understand pressure variations in the near-field, a numerical approach, as outlined in the next section, is required.

4.2 RESERVOIR FLOW AND GEOMECHANICAL MODELING

4.2.1 CAVONE RESERVOIR STATIC MODEL

4.2.1.1 STRATIGRAPHIC MODEL

To facilitate the first phase of our reservoir simulation and geomechanical modeling in the Cavone field, we developed a new reservoir model that includes the major stratigraphic and structural elements in the region (Figure 4.2.1). The new model is based on an earlier reservoir model on the crest of the Cavone structure, but has been extended to encompass all of the production and injection wells and the Mirandola fault. We placed an emphasis on defining the precise structural relationships between the reservoir units and Mirandola fault so that the simulation and geomechanical modeling can examine how field operations might influence the fluid pressures and stresses acting on the fault. The top of the reservoir layer corresponds to the "Breccia top" and the base to the "Nor_B bottom" horizon, consistent with the initial model. We extended these horizons away from the Cavone fold crest based on interpretation of 2-D seismic reflection data described earlier in this report. These seismic data were depth-converted using velocity functions based on sonic logs from the Cavone field. This mapping, guided by structural analysis using fault-related folding methods, defined the structure of the forelimb of the Cavone anticline, which dips steeply (> 50°) to the northeast and is cut by splays of the Mirandola fault. Both hanging wall and footwall cutoffs of the reservoir horizons were defined. In addition, we extended the reservoir horizons down dip along the backlimb and plunging noses of the Cavone fold. For this model, we did not explicitly include the displacements of secondary faults within the Cavone anticline, but rather represented these faults as localized dip and elevation changes in the reservoir horizons. Notably, both the initial and our extended model show significant along strike changes in the thickness of the reservoir units that may influence fluid flow and pressure changes due to production and injection activities.

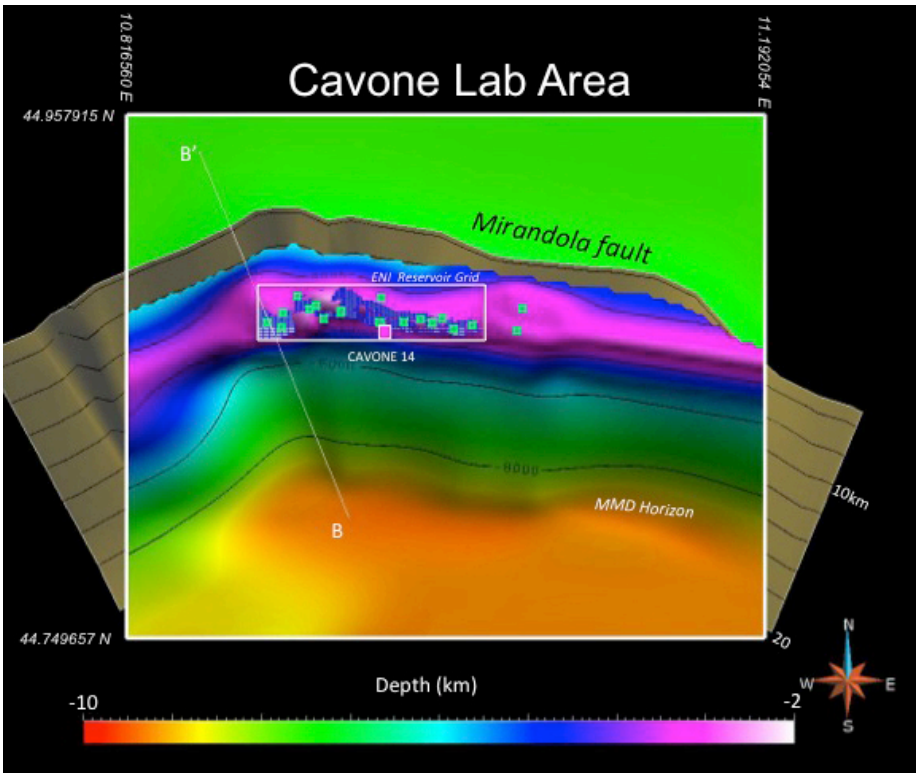

Figure 4.2.1: Map view of the Cavone lab Area, showing depth contours on the top reservoir surface. The small white rectangle shows the extent of the initial reservoir Model, which has been extended to include the Mirandola fault. Section B-B' is shown in Figure 1.2.5.

We developed triangulated surface representations of the stratigraphic horizons and faults (Figure 4.2.2) that served as the basis for developing a hexahedral mesh that was used for the computations. Developing a regular, volumetric mesh for the structure was challenging given the steep bed dips and the cutoff relationships with the Mirandola fault. Thus, this process involved iteratively simplifying and smoothing the initial structural model in order to develop a mesh that would support the computational analysis. In particular, the geometry of the reservoir in the footwall of the Mirandola fault was simplified, as this was anticipated to have little influence on the calculations.

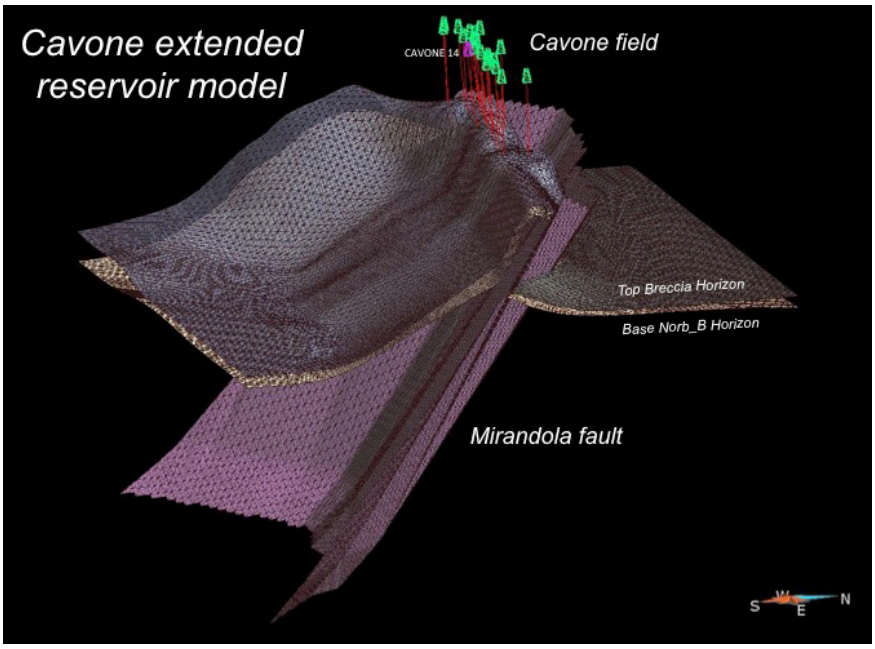

Figure 4.2.2: Perspective view of the extended Cavone reservoir model, showing the upper and lower reservoir horizons and the Mirandola fault.

A follow-on phase of reservoir modeling could include more detailed representations of stratigraphic units within the reservoir sequence and secondary faults. As dictated by the resolution of this modeling, the Maiolica, Malm, Dogger, Oolitico, Nor_A, and Nor_B (top) horizons could be added to the reservoir model, as well as splays of the Mirandola fault and backthrusts present in its hanging wall. This would allow refinement of the reservoir and geomechanical modeling, and assess how field operations may influence fluid pressures and stresses acting on these secondary faults that are closer to the wells.

4.2.1.2 GEOMECHANICAL GRID

The next step in the Cavone geomechanical study is the construction of a geomechanical grid, based on the surfaces identified during the stratigraphic model step. We used the following surfaces: hanging wall side surfaces of Breccia Top and Nor_B Bottom horizons and the Mirandola fault surface extended to the ground level with average dip of the fault. We used the Trelis software (CUBIT, 2013) to generate the hexahedral grid that honors these three surfaces.

Our workflow to generate the mesh is as follows. The surfaces are exported from Gocad using the facet representation, where each surface is triangulated and the coordinates of the nodes of the triangles, or facets, are exported in a file. This is an example of a mesh-based geometry where geometrical objects such as surfaces and curves are represented using facets. We used a resolution of 250 m in both *x* (east-west) and *y* (north-south) directions to export the

triangulated surface. To build a solid model and allow geometry decompositions (surface cuts), we had to convert the mesh-based geometry into a solid geometry format such as the CAD or ACIS format. Using the non-uniform rational b-splines (NURBS) in Trelis, we created solid surfaces that pass through the nodes of the facets. We encountered important challenges during this process because of the following reasons: steeply dipping Breccia Top and Nor_B surfaces, thinning of the reservoir layer as the two surfaces approach the Mirandola fault, and proximity of the Cavone fold crest to the fault.

Once the surfaces are created, we generated a 3D box domain of dimensions 29 km x 23.75 km x 20 km that contains the surfaces and the region of interest. We cut the box with the fault surface and imprint the reservoir surfaces on the south fault block. Then we merge all the geometries and mesh the boundary surfaces. Finally, we mesh the 3D volume. We check the mesh quality (condition numbers of the hex cells) and iterate the meshing process until achieving a satisfactory mesh quality. Note that the mesh quality is important for numerical integration of equations, solver convergence, and solution accuracy of the coupled flow and geomechanics simulation.

Figure 4.2.3 and Figure 4.2.4 show the geomechanical grid employed in this geomechanical study. Despite its coarseness, it allows us to test the entire methodology from mesh construction to coupled simulation, which is the objective of this coupled geomechanical study. We export the grid in Exodus format, which is a type of finite element grid format that can be read directly into our coupled simulator.

We process the Exodus grid using Matlab scripts to export coordinates of cell centroids and cell sizes, which are read by our flow simulator to create the equivalent finite volume grid.

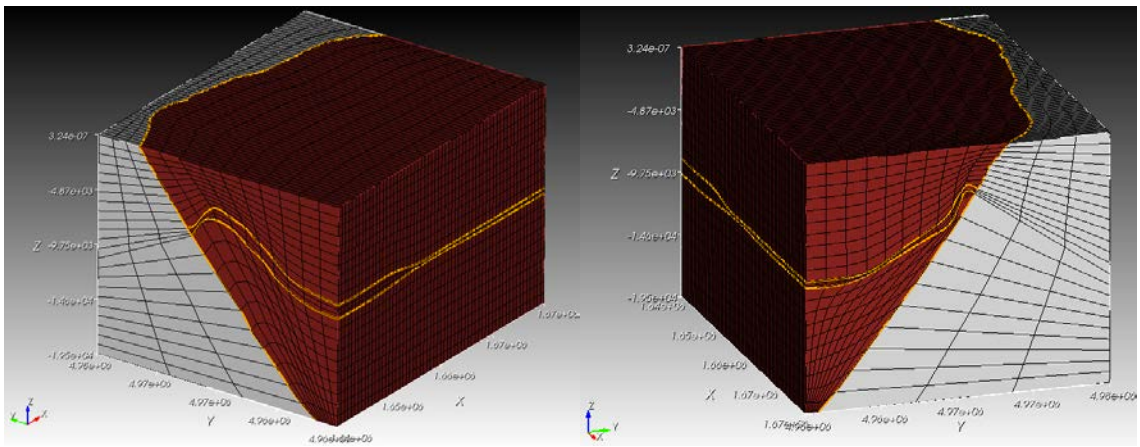

Figure 4.2.3: Cavone geomechanical grid constructed using the three surfaces (Breccia Top, Nor_B, and Mirandola fault). Red color indicates the hanging wall, and light color the foot wall. The coordinate system is such that the x-axis is easting, the y-axis is northing, and the z-axis is elevation in meters. Left: eastward view, right: westward view of the grid.

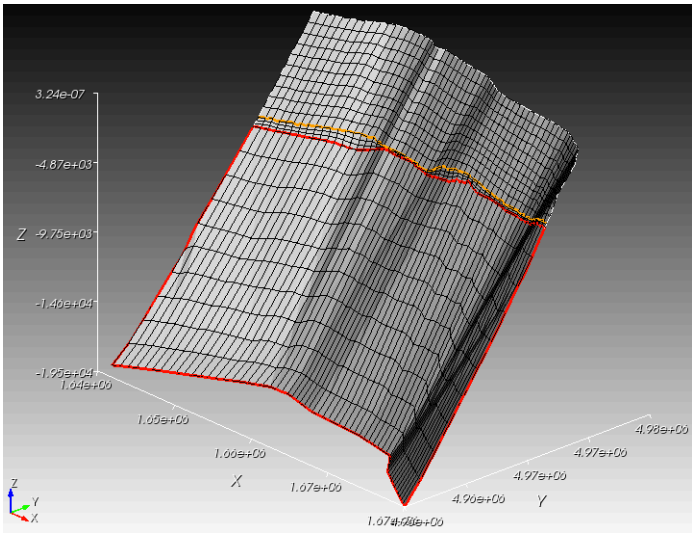

Figure 4.2.4: The Mirandola fault surface in the Cavone geomechanical grid. The reservoir layer, defined by the Breccia top and Nor_B bottom surfaces, is highlighted.

4.2.2 Cavone Reservoir Dynamic Model

4.2.2.1 Coupled Flow and Geomechanical Modeling

4.2.2.1.1 Introduction

Coupling between fluid flow and mechanical deformation in porous media plays a critical role in subsurface hydrology, hydrocarbon recovery, and seismic activity in the Earth's crust. Subsidence due to groundwater withdrawal has been studied for decades, but continues to pose significant challenges in many parts of the world (Geertsma, 1973a,b; Gambolati and Freeze, 1973; Bear and Corapcioglu, 1981; Mossop and Segall, 1997; Galloway et al., 1998; Gambolati et al., 2000; Galloway and Burbey, 2011). Production and injection of fluids in oil, gas, and geothermal fields have also been associated with surface subsidence and earthquakes along preexisting faults (Raleigh et al., 1976; Yerkes and Castle, 1976; Lofgren, 1981; Segall, 1989; Fialko and Simons, 2000; Ellsworth, 2013; Brodsky and Lajoie, 2013). Earthquakes triggered due to groundwater withdrawal (Gonzalez et al., 2012), reservoir impoundment (Carder, 1945; Lomnitz, 1974; Gupta, 2002), and wastewater disposal (Keranen et al., 2013, 2014; van der Elst et al., 2013) have been reported, as has been fluctuation in groundwater levels due to earthquakes (Roeloffs, 1996; Wang et al., 2001).

Recently, coupled flow and geomechanics has also gained attention due to its role in the long-term geologic storage of carbon dioxide CO2 in saline aquifers, which is widely regarded as a promising technology to help mitigate climate change by significantly reducing anthropogenic CO2 emissions into the atmosphere (e.g., Lackner, 2003; Pacala and Socolow, 2004; IPCC,

2005; Orr, 2009; Szulczewski et al., 2012). Injection of CO2 requires displacement or compression of the ambient groundwater, and an overpressurization of the target aquifer, which could fracture the caprock (Birkholzer and Zhou, 2009), trigger seismicity, and cause shear slip on preexisting faults (Rutqvist et al., 2007, 2008; Chiaramonte et al., 2008; Rutqvist et al., 2010; Morris et al., 2011a, 2011b; Cappa and Rutqvist, 2011a, 2011b), and potentially compromise the caprock by activating faults (Zoback and Gorelick, 2012a).

One of the fundamental issues is the ability to describe the mechanical and hydraulic behavior of faults, and the influence of the full stress tensor and change in pressure on fault slip. Injection and production of fluids from a geologic reservoir induce changes in the state of stress, both within and outside the reservoir, and these can affect the stability of preexisting faults. The effects of injection and production depend on the initial state of stress, the elastic moduli of the geologic structures, and the fault frictional properties. The effects are not always intuitively obvious and should be quantified using geomechanical models. This requires the development of a new generation of geomechanical models that include coupling between fluid flow and fault motion.

Currently, geomechanical models typically treat faults as failure zones that are discretized as three- dimensional elements where the rheology is allowed to be different (e.g., plastic with weakening failure) than in the rest of the domain (e.g., elastoplastic with hardening law) (Rutqvist et al., 2008; Cappa and Rutqvist, 2011a, 2011b). This approach has several limitations, including the inability to model actual slip along a surface of discontinuity, and the dependence of the simulation results on the level of grid refinement. Other models represent faults as surfaces using interface elements (e.g., Ferronato et al., 2008), but so far these models are uncoupled to flow, and they model fault slip using a penalty method (Glowinsky and Le Tallec, 1989). Such methods require a priori selection of the penalty parameters for the fault, and therefore cannot represent dynamically evolving fault strength, such as slip-weakening or rate- and state-friction models (Dieterich, 1979a). Interface elements have also been used to model tensile fractures during the simulation of coupled flow and deformation in fractured media (Segura and Carol, 2004, 2008a, 2008b).

The interactions between flow and geomechanics have been modeled computationally using various coupling schemes (Dean et al., 2006; Jeannin et al., 2007; Jha and Juanes, 2007; Mainguy and Longuemare, 2002; Minkoff et al., 2003; Settari and Mourits, 1998; Settari and Walters, 2001; Thomas et al., 2003; Tran et al., 2004, 2005; Kim et al., 2011a, 2011b, 2011c, 2013). In the fully implicit method, one solves the coupled discrete nonlinear system of equations simultaneously, typically using the Newton-Raphson scheme (Sukirman and Lewis, 1993; Pao and Lewis, 2002; Lewis et al., 2003; Li et al., 2005; Ferronato et al., 2010). The fully implicit method guarantees unconditional stability if the mathematical problem is well posed, but the simulation of flow and geomechanics for realistic fields becomes computationally very expensive (Settari and Mourits, 1998; Thomas et al., 2003; Jha and Juanes, 2007). Sequential approaches to modeling coupled flow and geomechanics are highly desirable because they offer the flexibility of using separate simulators for each subproblem

(Felippa and Park, 1980; Samier and Gennaro, 2007; Minkoff et al., 2003; Rutqvist et al., 2002). The design and analysis of sequential methods with appropriate stability properties for poromechanics and thermomechanics has a long history (Zienkiewicz et al., 1988; Armero and Simo, 1992, 1993; Armero, 1999; Settari and Mourits, 1998; Mainguy and Longuemare, 2002; Jeannin et al., 2007).

Recently, a new sequential method for coupled flow and geomechanics, termed the "fixed-stress split," has been proposed and analyzed (Kim et al., 2011a, 2011b, 2013). Stability and convergence analyses have shown that the fixed-stress split inherits the dissipation properties of the continuum problem and is therefore unconditionally stable, both in the linear (poroelastic) and nonlinear (poroelastoplastic) regime. The analysis has shown that the fixed-stress split enjoys excellent convergence properties, even in the quasi-incompressible limit. It has also been shown recently that the stability and convergence properties of the fixed-stress split for single-phase flow carry over to multiphase systems if a proper definition of pore pressure, the "equivalent pore pressure" (Coussy, 2004), is used (Kim et al., 2013).

In this section, we describe our computational model for coupled flow and geomechanics of faulted reservoirs. We couple a flow simulator with a mechanics simulator using the fixed-stress scheme (Kim et al., 2011b). We employ a rigorous formulation of nonlinear multiphase geomechanics (Coussy, 1995) based on the increment in mass of fluid phases, instead of the more common, but less accurate, scheme based on the change in porosity (Settari and Mourits, 1998; Minkoff et al., 2003; Thomas et al., 2003; Tran et al., 2004, 2005; Rutqvist et al., 2002). Our nonlinear formulation is required to properly model systems with high compressibility or strong capillarity (Coussy, 1995), as can be the case for geologic CO2 sequestration (Rutqvist et al., 2007, 2008), groundwater extraction from unconfined aquifers (Gambolati and Freeze, 1973; Gonzalez et al., 2012), and shale gas production (Engelder, 2012). To account for the effect of surface stresses along fluid-fluid interfaces, we use the equivalent pore pressure in the definition of multiphase effective stress (Coussy, 2004; Kim et al., 2013). We model faults as surfaces of discontinuity using interface elements (Aagaard et al., 2012, 2013). This allows us to model stick-slip behavior on the fault surface for dynamically evolving fault strength.

4.2.2.1.2 MATHEMATICAL FORMULATION OF COUPLED MULTIPHASE POROMECHANICS

Balance laws

We use a classical continuum representation in which the fluids and the solid skeleton are viewed as overlapping continua (Bear, 1972; Coussy, 2005). The governing equations for coupled flow and geomechanics are obtained from conservation of mass and balance of linear momentum. We assume that the deformations are small, that the geomaterial is isotropic, and that the conditions are isothermal. Let Ω be our domain of interest and $\partial\Omega$ be its closed

boundary. Under the quasistatic assumption for earth displacements, the governing equation for linear momentum balance of the solid/fluid system can be expressed as

$$\nabla \cdot \boldsymbol{\sigma} + \rho_b \boldsymbol{g} = \mathbf{0}, \qquad \text{Eq. 10}$$

where $\boldsymbol{\sigma}$ is the Cauchy total stress tensor, $\boldsymbol{g}$ is the gravity vector, and $\rho_b = \phi \sum_{\beta}^{n_{\text{phase}}} \rho_\beta S_\beta + (1-\phi)\rho_s$ is the bulk density, ρ_β and S_β are the density and saturation of fluid phase β, and ρ_s is the density of the solid phase, ϕ is the true porosity, and n_{phase} is the number of fluid phases. The true porosity is defined as the ratio of the pore volume to the bulk volume in the current (deformed) configuration. Assuming that the fluids are immiscible, the mass-conservation equation for each phase α is

$$\frac{dm_\alpha}{dt} + \nabla \cdot \boldsymbol{w}_\alpha = \rho_\alpha f_\alpha, \qquad \text{Eq. 11}$$

where the accumulation term dm_α/dt describes the time variation of fluid mass relative to the motion of the solid skeleton, $\boldsymbol{w}_\alpha$ is the mass-flux of fluid phase α relative to the solid skeleton, and f_α is the volumetric source term for phase α. The two balance equations (10) and (11) are coupled by virtue of poromechanics. On one hand, changes in the pore fluid pressure lead to changes in effective stress, and induce deformation of the porous material—such as ground subsidence caused by groundwater withdrawal. On the other hand, deformation of the porous medium affects fluid mass content and fluid pressure. The simplest model of this two-way coupling is Biot's macroscopic theory of poroelasticity (Biot, 1941; Geertsma, 1957; Coussy, 1995). In the remainder of this section we provide the mathematical description of poroelasticityfor multiphase fluid systems.

Multiphase poromechanics

In the multiphase or partially saturated fluid system, it is not possible to linearize the equations of poroelasticity around a reference state because (Coussy, 1995):

1. Gases are very compressible,
2. Capillary pressure effects are intrinsically nonlinear, and
3. Phase saturations vary between 0 and 1 and, therefore, a typical problem samples the entire range of nonlinearity.

Therefore, following Coussy (1995), we use the incremental formulation of poromechanics for multiphase systems, which does not assume physical linearization of total stress from the initial state to the current (deformed) state. We make a modeling assumption that allows us to

express the deformation of a multiphase porous material in terms of the increment in applied total stresses and internal fluid pressures. We adopt an effective stress formulation in the multiphase poromechanics (Bishop, 1959; Bishop and Blight, 1963) because constitutive modeling of porous materials is usually done in terms of the effective stress. Under this formulation, we split the total stress on the porous material into two parts: one that is responsible for deformation of the solid skeleton (the effective stress), and another component that is responsible for changes in the fluid pressures,

$$\delta\boldsymbol{\sigma} = \boldsymbol{C}_{dr} : \delta\boldsymbol{\varepsilon} - \sum_{\beta} b_{\beta}\, p_{\beta}\mathbf{1}, \qquad \text{Eq. 12}$$

where b_β are the Biot coefficients for individual phases such that $\sum_\beta b_\beta = b$, where b is the Biot coefficient of the saturated porous material. It is common to further assume that b_β are proportional to the respective saturations S_β (Lewis and Sukirman, 1993; Coussy et al., 1998; Lewis and Schrefler, 1998).

The effective stress concept allows us to treat a multiphase porous medium as a mechanically equivalent single-phase continuum (Khalili et al., 2004; Nuth and Laloui, 2008). The appropriate form of the effective stress equation in a multiphase system is still an active area of research (Gray and Schrefler, 2001; Coussy et al., 2004; Nuth and Laloui, 2008; Vlahinic et al., 2011; Nikooee et al., 2013; Kim et al., 2013). Here we use the concept of equivalent pressure (Coussy et al., 2004) in the effective stress equation (Eq. (12)),

$$p_E = \sum_{\beta} S_\beta p_\beta - U, \qquad \text{Eq. 13}$$

where $U = \sum_\beta \int p_\beta dS_\beta$ is the interfacial energy computed from the capillary pressure relations (Kim et al., 2013). The equivalent pressure accounts for the interface energy in the free energy of the system, and leads to a thermodynamically consistent and mathematically well-posed description of the multiphase fluid response to the solid deformation (Kim et al., 2013). For a system with two phases, the wetting phase *w* and the non-wetting phase *o*, the capillary pressure is

$$P_c(S_w) \equiv P_{wo}(S_w) = p_o - p_w, \qquad \text{Eq. 14}$$

and the interfacial energy is $U = \int_{S_w}^{1} P_{wg} dS$. Assuming $b_\beta = bS_\beta$ (Lewis and Sukirman, 1993; Coussy et al., 1998; Lewis and Schrefler, 1998), and using Eq. (13) in Eq. (12), we obtain the stress-strain relation- ship for multiphase linear poroelasticity:

$$\delta\boldsymbol{\sigma} = \delta\boldsymbol{\sigma}' - b\delta p_E \mathbf{1}, \qquad \delta\boldsymbol{\sigma}' = \boldsymbol{C}_{dr} : \delta\boldsymbol{\varepsilon}. \qquad \text{Eq. 15}$$

Once we have a definition of the effective stress in multiphase systems, we now express the change in the fluid mass in terms of the mechanical deformation and the change in the fluid pressures. In the deformed configuration, the mass of phase α per unit volume of porous medium is

$$m_\alpha = \rho_\alpha S_\alpha \phi (1 + \varepsilon_v), \qquad \text{Eq. 16}$$

Note that, by definition, the sum of all fluid phase saturations adds up to 1. For multiphase systems (Coussy, 1995, 2004), we have

$$\left(\frac{dm}{\rho}\right)_\alpha = b_\alpha d\varepsilon_v + \sum N_{\alpha\beta} dp_\beta, \qquad \text{Eq. 17}$$

where $\boldsymbol{N} = \boldsymbol{M}^{-1}$ is the inverse Biot modulus. In a multiphase system, the Biot modulus is a symmetric positive definite tensor $\boldsymbol{M} = \left[M_{\alpha\beta}\right]$, and the Biot coefficient is a vector. To determine the coupling coefficients $N_{\alpha\beta}$ as a function of the primary variables (pressure, saturations, and displacements) and rock and fluid properties we develop an alternate expression for the differential increment in fluid mass. Using Eq. (16),

$$dm_\alpha = d\left(\rho_\alpha S_\alpha \phi (1 + \varepsilon_v)\right), \qquad \text{Eq. 18}$$

which can be expanded as

$$\left(\frac{dm}{\rho}\right)_\alpha = \phi \frac{\partial S_\alpha}{\partial P_{\alpha\beta}} dP_{\alpha\beta} + \phi S_\alpha c_\alpha dp_\alpha + \phi S_\alpha d\varepsilon_v + S_\alpha d\phi, \qquad \text{Eq. 19}$$

where c_α is the compressibility of the fluid phase α, and $\partial S_\alpha/\partial P_{\alpha\beta}$ is the inverse capillary pressure derivative. Above, repeated indices do not imply summation and we have assumed infinitesimal deformations. We can express the increment in porosity $d\phi$ as a function of the volumetric effective stress $d\sigma'_v$ to obtain a closed-form expression of Eq. (19). Let $V_s = V_b - V_p$ be the volume of the solid matrix, and $d\varepsilon_{sv} = dV_s/V_s = d\sigma_{sv}/K_s$ be the volumetric dilation of the solid matrix, where σ_{sv} is the volumetric matrix stress. From an expansion of $d\phi$ we can write the incremental form of strain partition as

$$(1-\phi)d\varepsilon_v = (1-\phi)d\varepsilon_{sv} + d\phi. \qquad \text{Eq. 20}$$

Similarly, the volumetric Cauchy total stress can be partitioned into the volumetric matrix stress and the fluid pressure as

$$d\sigma_v = (1-\phi)d\sigma_{sv} - \phi dp_E. \qquad \text{Eq. 21}$$

Substituting $d\sigma_{sv}$ from Eq. (21) into Eq. (20), we obtain

$$d\phi = \frac{b-\phi}{K_{dr}}(d\sigma'_v + (1-b)dp_E). \qquad \text{Eq. 22}$$

Equation (22) implies that an increment in porosity is related to increments in volumetric effective stress and fluid pressures. Substituting $d\varepsilon_v$ from Eq. (15) and $d\phi$ from Eq. (22) into Eq. (19) allows us to express the increment in the phase mass as a function of the increments in the total volumetric stress and phase pressures. Equating this to Eq. (18) yields the desired expressions for the coupling coefficients $N_{\alpha\beta}$.

Finally, we obtain the multiphase flow equation for phase α in a poroelastic medium by substituting the two constitutive relations, the effective stress equation, Eq. (15), and the fluid mass increment equation, Eq. (17), in the mass balance equation, Eq. (11):

$$\frac{\partial}{\partial t}\left(\rho_\alpha \sum_\beta \left(N_{\alpha\beta} + \frac{b_\alpha b_\beta}{K_{dr}}\right)p_\beta\right) + \frac{1}{K_{dr}}\frac{\partial}{\partial t}(\rho_\alpha b_\alpha \sigma_v) + \nabla\cdot\boldsymbol{w}_\alpha = \rho_\alpha f_\alpha, \qquad \forall\alpha = 1,\dots,n_{\text{phase}}$$

Eq. 23

The role of N and b as the coupling coefficients among different fluid phases and the solid phase is evident from the above equation. The bulk density, ρ_b, in the mechanical equilibrium equation, Eq. (10), also acts as a coupling parameter because it is a function of the porosity and the phase saturations. Because we assume that the fluids are immiscible, the mass-flux of phase α is $\boldsymbol{w}_\alpha = \rho_\alpha \boldsymbol{v}_\alpha$, where we adopt the traditional multiphase-flow extension of Darcy's law (Muskat, 1949; Bear, 1972):

$$\boldsymbol{v}_\alpha = \frac{\boldsymbol{k} k_\alpha^r}{\mu_\alpha}(\nabla p_\alpha - \rho_\alpha \boldsymbol{g}), \qquad \text{Eq. 24}$$

where μ_α and k_α^r are the dynamic viscosity and the relative permeability of phase α in presence of other fluid phases.

4.2.2.1.3 POROMECHANICS OF FAULTS

There are two basic approaches to represent faults in a three-dimensional medium: either as a three-dimensional fault zone (e.g., Rutqvist et al., 2008) or a two-dimensional fault surface (e.g., Juanes et al., 2002; Molinero et al., 2002; Ferronato et al., 2008). The advantage of representing faults as surfaces of discontinuity is that they can more faithfully describe the localized (discontinuous) displacement at the fault, and that one can incorporate models of dynamic frictional strength (like the rate- and state-friction model) capable of reproducing runaway fault slip characteristic of earthquakes. Moreover, introducing discrete fault surfaces does not preclude modeling an adjacent fault zone with appropriate rheology.

A central feature of our work is that we treat faults as surfaces of discontinuity embedded in the continuum, across which displacement is allowed to be discontinuous to recognize the possibility of fault slip (Figure 4.2.5). We use zero-thickness elements, also known as interface elements or cohesive elements in the finite element literature (Goodman et al., 1968; Beer, 1985; Carol et al., 1985; Gens et al., 1988; Lei et al., 1995), to represent the fault surfaces. Mathematically, the fault surface is treated as an interior boundary between the two adjacent domains. The two sides of the fault surface, which need not be planar, are designated as the '+' side and the '−' side, and the fault normal vector, $\boldsymbol{n}$, points from the negative side to the positive side. Slip on the fault is the displacement of the positive side relative to the negative side,

$$(\boldsymbol{u}_+ - \boldsymbol{u}_-) - \boldsymbol{d} = \boldsymbol{0} \quad \text{on} \quad \Gamma_f, \qquad \text{Eq. 25}$$

where $\boldsymbol{u}_+$ and $\boldsymbol{u}_-$ are the displacements on the two sides of the fault surface, denoted by Γ_f, and $\boldsymbol{d}$ is the fault slip vector. Fault slip is governed by the effective traction on the fault, which is a function of the effective stress tensors on both sides of the fault, the fault normal direction, and the fault constitutive law. We impose the effective traction on the fault by introducing a Lagrange multiplier, $\boldsymbol{l}$, which is a force per unit area required to satisfy the equilibrium equation for a given relative displacement, $\boldsymbol{d}$, across the fault. The magnitude of the effective normal traction on the fault is

$$\sigma'_n = \boldsymbol{l} \cdot \boldsymbol{n}. \qquad \text{Eq. 26}$$

A positive value of σ'_n indicates that a tensile effective stress is transmitted across the fault surface. The Kuhn-Tucker conditions of contact mechanics are obeyed such that no penetration occurs and the effective normal traction stays compressive at the contact surface. The shear traction vector is, by definition, tangent to the fault surface and its magnitude is

$$\tau = |\boldsymbol{l} - \sigma'_n \boldsymbol{n}|. \qquad \text{Eq. 27}$$

We use the Mohr-Coulomb theory to define the stability criterion for the fault (Jaeger and Cook, 1979). When the shear traction on the fault is below the friction stress, $\tau \leq \tau_f$, the fault does not slip. When the shear traction is larger than the friction stress, $\tau > \tau_f$, the contact problem is solved to determine the Lagrange multipliers and slip on the fault, such that the Lagrange multipliers are compatible with the frictional stress.

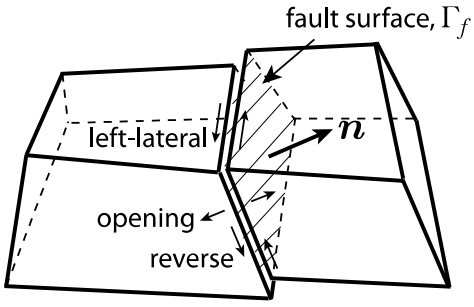

*Figure 4.2.5: Schematic of a 2D fault surface in a 3D domain. Discontinuity in the displacement across the fault is illustrated through the slip vector, **d**, on the fault. Here, slip is assumed to be in the fault plane with no opening. The fault normal vector **n**, strike angle ψ, dip angle δ, and slip rake angle γ are defined in the global coordinate system. The fault coordinate system is defined in terms of tangential and normal motion on the fault with positive values associated with left-lateral, reverse, and opening motions.*

4.2.2.1.4 FAULT PRESSURE IN THE FAILURE CRITERION

Traditionally, in the Andersonian faulting theory (Anderson, 1951), fault slip is modeled in a "dry environment," that is, in the absence of fluids. While, in some cases, the presence of fluid has been recognized through the effective stress concept, the dynamics of flow was not included for reasons of conceptual and computational simplicity, as well as for the belief that fluid flow played a secondary role in the release of tectonic stresses (Hubbert and Rubey, 1959; Reasenberg and Simpson, 1992). The effect of pore pressure was accounted for by modifying the coefficient of fault friction μ_f (Harris and Simpson, 1992; Harris et al., 1995), an approach later suggested to be "unwise" (Beeler et al., 2000). In the case of mature faults, the fault core permeability can be low due to comminution of grains while the damaged host rock permeability can be high due to fractures (Sibson, 1977, 1986; Chester et al., 1993; Caine and Forster, 1999). In addition, the permeability can vary substantially across the fault during the seismic cycle (Sibson, 1981, 1990). As a result, pore pressures can be significantly different across the fault (Sibson, 1994; Rice, 1992; Chester et al., 1993).

A difference in fluid pressure across the fault leads to a pressure jump $[\![p]\!]_{\Gamma_f} = p_+ - p_-$, where p_+ and p_- are the equivalent multiphase pressures (equation (13)) on the "positive" and the "negative" side of the fault. One of the key features of the 2-D representation of faults is the ability to reproduce a finite jump in the pressure, $[\![p]\!]_{\Gamma_f}$, across the fault. This pressure jump leads to a discontinuity in the effective stress across the fault, such that the total stress is continuous

$$\boldsymbol{\sigma'}_- \cdot \boldsymbol{n} - bp_-\boldsymbol{n} = \boldsymbol{\sigma'}_+ \cdot \boldsymbol{n} - bp_+\boldsymbol{n}, \qquad \text{Eq. 28}$$

a requirement for momentum balance on the fault. This gives rise to the question of how to incorporate in the formulation the pressure jump across a fault. This is important because it determines the stability of the fault.

Fault stability can be assessed by evaluating the stability criterion on both sides of the fault separately. The side of the fault where the criterion is met first determines the fault stability. Equivalently, this can be achieved by defining a *fault pressure* that is a function of the pressures on the two sides, p_+ and p_-. Introducing the fault pressure allows us to uniquely define the *effective* normal traction on the fault, σ'_n, and determine the fault friction τ_f. Since the stability criterion, $\tau \leq \tau_f$, is first violated with the larger pressure, we define the fault pressure, p_f, as

$$p_f = \max(p_+, p_-). \qquad \text{Eq. 29}$$

Our definition of fault pressure is a natural result of our fault representation, rather than a conservative assumption. Note that estimating the fault pressure as the arithmetic average of the pressures on the two sides, as proposed in the case of tensile fractures (Segura and Carol, 2004, 2008a, 2008b), may incorrectly delay the onset of shear failure. By univocally defining the pressure at the fault (equation (29)), we also univocally define the effective traction at the fault (the Lagrange multiplier $\boldsymbol{l}$), something that is required to evaluate the fault stability criterion.

4.2.2.1.5 IMPLEMENTATION INTO A SIMULATION SOFTWARE

We developed a coupled multiphase flow and geomechanical simulator by coupling the General Purpose Research Simulator (GPRS) (Cao, 2002; Pan and Cao, 2010) as the flow simulator, and PyLith (Aagaard et al., 2012, 2013) as the mechanics simulator. Below we describe the major steps in the development of this coupled simulator.

The flow simulator

GPRS is a general purpose, object-oriented, reservoir simulator for multiphase/multicomponent subsurface flows. It treats element connections through a general connection list, which allows for both structured and unstructured grids. GPRS is capable of handling complex production and injection scenarios in the field, such as wells perforated at multiple depths and flowing under variable rate and pressure controls. The original simulator (Cao, 2002; Pan and Cao, 2010) does not account for coupling with the mechanical deformation, and it models the mechanical behavior of the system through a user-provided rock compressibility (Aziz and Settari, 1979). We modified and extended the original code to implement the coupling with the mechanics simulator. In particular, we implemented the functionality to compute the modified accumulation term in the fluid phase mass balance equations. We also modified the setup of the linear system to implement the flow step of the fixed-stress sequential solution scheme (Kim et al., 2011a).

The geomechanics simulator

PyLith is a finite element code for the simulation of static and dynamic large-scale deformation problems (Aagaard et al., 2012, 2013). Much of its development has been motivated by the modeling of earthquake physics; however, its applicability extends to problems at any other scale, such as the reservoir scale or the laboratory scale. Some of the advantages of PyLith are (1) it is an open-source code and can be modified for specific purposes; (2) it is written using C++ and Python languages and is extendable; (3) it is suitable for parallel computing; (4) it allows localized deformation along discrete features, such as faults; and (5) it is well integrated with meshing codes, such as LaGriT for tetrahedral meshes (LaGriT, 2013) and CUBIT for both tetrahedral and hexahedral meshes (CUBIT, 2013). PyLith uses an implicit formulation to solve quasi-static problems and an explicit formulation

to solve dynamic rupture problems. Originally, PyLith is not coupled to any fluid flow model. We modified the code of PyLith version 1.8.0 and coupled it with the flow imulator, GPRS. In particular, we implemented a C++ class, iGPRS, to allow communication between the flow and the mechanics simulators. iGPRS provides the functionality required for exchanging information (pressures, saturations, and volumetric total stress) between the two simulators.

PyLith supports distributed memory parallelization (Message Passing Interface or MPI) whereas GPRS's parallelization is based on the shared memory architecture (Multiprocessing or OpenMP). We integrated the two such that we can run the coupled simulator on a cluster with multiple compute nodes (distributed memory) where individual nodes have multiple cores or processors (shared memory).

Grid

We use a single grid for both GPRS and PyLith. The grid is generated using CUBIT (CUBIT, 2013) or LaGriT (LaGriT, 2013) mesh generation software. We define geologic surfaces, material regions, faults, and pinch-outs during the geometry creation stage. Then we mesh the domain with hexahedral elements using a fine mesh in the reservoir domain and an increasingly coarse mesh in the overburden, underburden, and sideburden regions. We export the grid in a finite element format such as the Exodus-II format (CUBIT, 2013) for PyLith. We process the grid file using a MATLAB script to generate the equivalent finite volume grid in the domain with element centroid coordinates, element bulk volumes, and face transmissibilities in the Corner Point Geometry format (Schlumberger, 2009). Any grid elements lying outside the flow region of interest (e.g., in overburden and underburden) can be deactivated for the solution of the flow problem. GPRS uses the finite volume grid for simulating flow in the region of interest. The two simulators exchange pressures, saturations, and volumetric stress information inside this region.

Implementation of Faults

To support relative motion across fault surfaces, PyLith modifies the grid topology to create zero-thickness fault elements and adds additional degrees of freedom to hold the Lagrange multipliers and fault slip vectors at the Lagrange nodes (Aagaard et al., 2012, 2013) (Figures 4.2.5 and 4.2.6). PyLith solves the contact problem iteratively in two steps. In the first step, the elasticity problem is solved over the entire domain to update the displacements and the fault tractions (Lagrange multipliers) corresponding to the current estimate of the slip. The Lagrange multipliers are compared with the friction stress on the fault and are adjusted to be compatible with the fault constitutive model. In the second step, the fault slip is updated corresponding to the adjustment in the Lagrange multipliers while assuming that the deformation due to slip is localized to the elements adjacent to the fault, that is, that displacements at non-fault nodes do not change from their values at the current Newton iteration. If the fault slips over the entire domain, such that the assumption of deformation being limited to the adjacent elements is not met, the convergence of the iterative scheme is poor. Also, if the fault friction coefficient changes significantly with slip (e.g., in rate- and

state-dependent models), it leads to large changes in τ_f at every iteration and convergence may degrade. To improve convergence, a line-search routine is used as part of the iterative scheme to find the optimum perturbation in the Lagrange multipliers that minimizes the combined mismatch between the fault friction and the fault shear traction at all the fault nodes (Aagaard et al., 2013). We modified PyLith's original line-search routine such that the inequality constraint, $\tau \leq \tau_f$, is always honored.

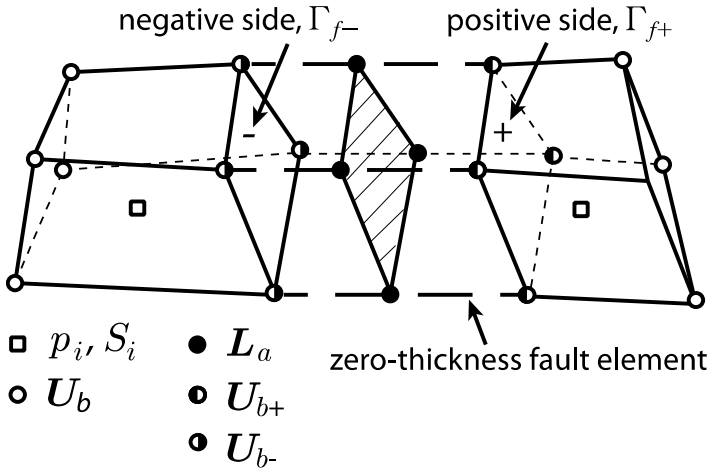

Figure 4.2.6. Exploded view of our computational representation of a fault, illustrating different node types, locations of different variables, and the zero-thickness fault element. Fluid pressures p_i and saturations S_i are located at the element centers as they are discretized using the finite volume method. Displacements and Lagrange multipliers at the fault are discretized using the nodal-based finite element method. There are two types of nodes in the domain: the displacement nodes and the Lagrange nodes. The displacement nodes carry the displacements $\boldsymbol{U}_{br}$ at the regular nodes, the displacements $\boldsymbol{U}_{b+}$ on the positive side of the fault, and the displacements $\boldsymbol{U}_{b-}$ on the negative side of the fault. The Lagrange nodes carry two types of fault variables: the Lagrange multipliers $\boldsymbol{L}_b$ (related to fault tractions), and the fault slip $\boldsymbol{D}_b$. The displacement nodes on the positive and negative sides, and the Lagrange nodes are collocated in the initial grid.

4.2.2.2 COUPLED FLOW-GEOMECHANICAL SIMULATION OF THE CAVONE RESERVOIR

We consider a two-phase Black Oil system with linear poroelasticity. The wells are operating within the reservoir layer; however, the coupled simulation is performed over the entire domain to account for the effect of flow on the stability of the fault. We impose reverse faulting conditions: lithostatic overburden as the minimum principal stress and north-south compression at twice the overburden as the maximum principal stress. The fault is treated as impermeable to flow, however, we could perform sensitivity analysis later by changing the fault permeability values, both along and across the fault. Similarly, we can perform sensitivity on the strength of the aquifer support. Below we discuss the initial conditions and boundary conditions in the model.

We follow one of the history-match simulations of the Cavone field (CAV2001_HIS_2_SAVE) in the data provided to initialize our flow model. We initialize the pressures hydrostatically with a datum pressure of 290.1 bar (4207.5 psi) at a depth of 2990 m (9809.6 ft), oil density of 22 API gravity, and water density of 1.0 gm/cc. We initialize the saturations with an irreducible water saturation of 0.38 and a residual oil saturation of 0.17. For this geomechanical study, we choose an oil-water contact (OWC) that is deeper than the OWC of 10270 ft in the Eclipse history match simulation. We choose these values such that the model is able to honor the historical rates of production and injection for the prescribed porosity and permeability values. Since in our simulations the OWC is deeper, the pressures from the coupled simulation are higher than the pressures in the history match simulation. However, we are more interested in the change in pressure to evaluate the change in Coulomb stresses on the fault.

Initial displacements are zero everywhere. Initial stresses are prescribed to be lithostatic in the vertical direction, twice the lithostatic in north-south, and 1.5 times the lithostatic in the east-west direction. The lithostatic gradient is calculated with the bulk density which depends on the solid grain density, assumed to be 2600 kg/m^3, fluid phase densities, fluid saturations, and porosity.

We apply compression at twice the lithostatic on the northern boundary and apply roller boundary conditions on east, west, south, and bottom boundaries. The top boundary is a traction-free surface. All boundaries are no-flow boundaries.

Now we discuss the rock and fluid properties distribution in the coupled model. For this study, we assume a uniform distribution of properties with values that are within the range of values used in the history match simulation: porosity = 0.1, permeability = 1 md, Young's modulus = 55 GPa, and Poisson's ratio = 0.28. We took the elastic properties from Cavone11_Geomech_Report.pdf, Carota no. 10, depth interval 2966-2975 m. We use the following fluid PVT data:

```
PHASE_NAME OIL
STANDARD_DENS 57.548
# P     BO      VISC    RGW
# PSI   RB/BBL  CP      SCF/STB
14.7     1.2000 8.4     0.0
812.211  1.1100 8.46    0.0
1116.791 1.1073 8.72    0.0
1479.385 1.1047 9.06    0.0
2219.077 1.0995 9.76    0.0
2958.770 1.0950 10.61   0.0
```

```
3698.462 1.0902 11.74   0.0
4423.651 1.0861 12.64   0.0
5801.510 1.0800 13.00   0.0

PHASE_NAME WATER
STANDARD_DENS 62.428
#P         BW          VISC   ROW
#PSI     RB/BBL        CP     STB/SCF
14.7     1.03          1.0     0
4351.13 1.018          0.4     0
```

We use the following relative permeability table for the entire domain:

```
#SW      KRW     KROW    PCOW (PSI)
0.381   0       0.814   11.60296
0.382   0.022   0.78    10.732738
0.43    0.055   0.68    8.70222
0.51    0.1     0.46    4.35111
0.586   0.15    0.255   2.90074
0.645   0.18    0.121   2.320592
0.688   0.19    0.058   2.030518
0.732   0.21    0.02    1.740444
0.802   0.22    0.002   1.305333
0.833   0.257   0       1.015259
0.87    0.257   0       0.725185
1       0.257   0       0
```

Both PVT and relative permeability data are derived from existing data (file petrel eclipse modeling/Cavone_Ecl_model_1996_updt2004/inputRSCTE11.PVT).

We perform the dynamic simulation from 1 March 1980 to 31 Dec 2012 (duration 11994 days) by imposing the historical oil production rate for producers and historical water injection rate for injectors. We include 19 Cavone wells in the flow model with their completion intervals and rates taken from Cavone history match simulation (COMPL1.DAT and HIS_01_2005.DAT, respectively). All the wells are located near the crest of the Cavone anticline. The following wells are oil producers: CA01 to CA04, CA07 to CA13, CA15, CA16, CA17, CA19, and CA21. The following wells are water injectors: CA05I, CA11I and CA14I. Well CA11 stops production on 31 May 1989 and begins injection within the same depth interval on 31 Aug 1989.

We perform two simulations with this model. The difference between the two simulations is in the type and magnitude of aquifer support during depletion of the reservoir, as this is one of the uncertainties in this field that could play a role in determining the stability of the Mirandola fault. The first simulation has only the lateral aquifer support coming from the water in the reservoir layers below the OWC and flow in the reservoir is prevented from communicating with the aquifer layers below the reservoir through use of vertical transmissibility multiplier. Although flow communication is prevented, elastic and poroelastic effects are still present. This model is relatively straightforward to understand because the pressure changes are highly localized to a thin layer.

The second simulation has both the lateral and the bottom aquifer support. For the overburden layers above the reservoir, we use a transmissibility multiplier in the vertical direction to isolate the reservoir from layers above it. As we discuss in Section 4.1, there is evidence both from the permeability measurements in cores and from the temperature profile in the injection test that flow extends into the aquifer below the reservoir. The added complication of pressure changes extending to substantial depth beneath the reservoir makes the results from this model more subtle to interpret. However it is our preferred model because it is consistent with the other constraints discussed in 4.1.

Case 1: Lateral aquifer support only

We drive the dynamic simulation with well rates as described above. In Figure 4.2.7 we plot simulated rates for the major producers and all three injectors. We did not attempt to history match the well pressures or the water cuts. There are some small differences in start dates for injection from those reported in Table 3.1.3 because of some test injections carried out before the main injection phase.

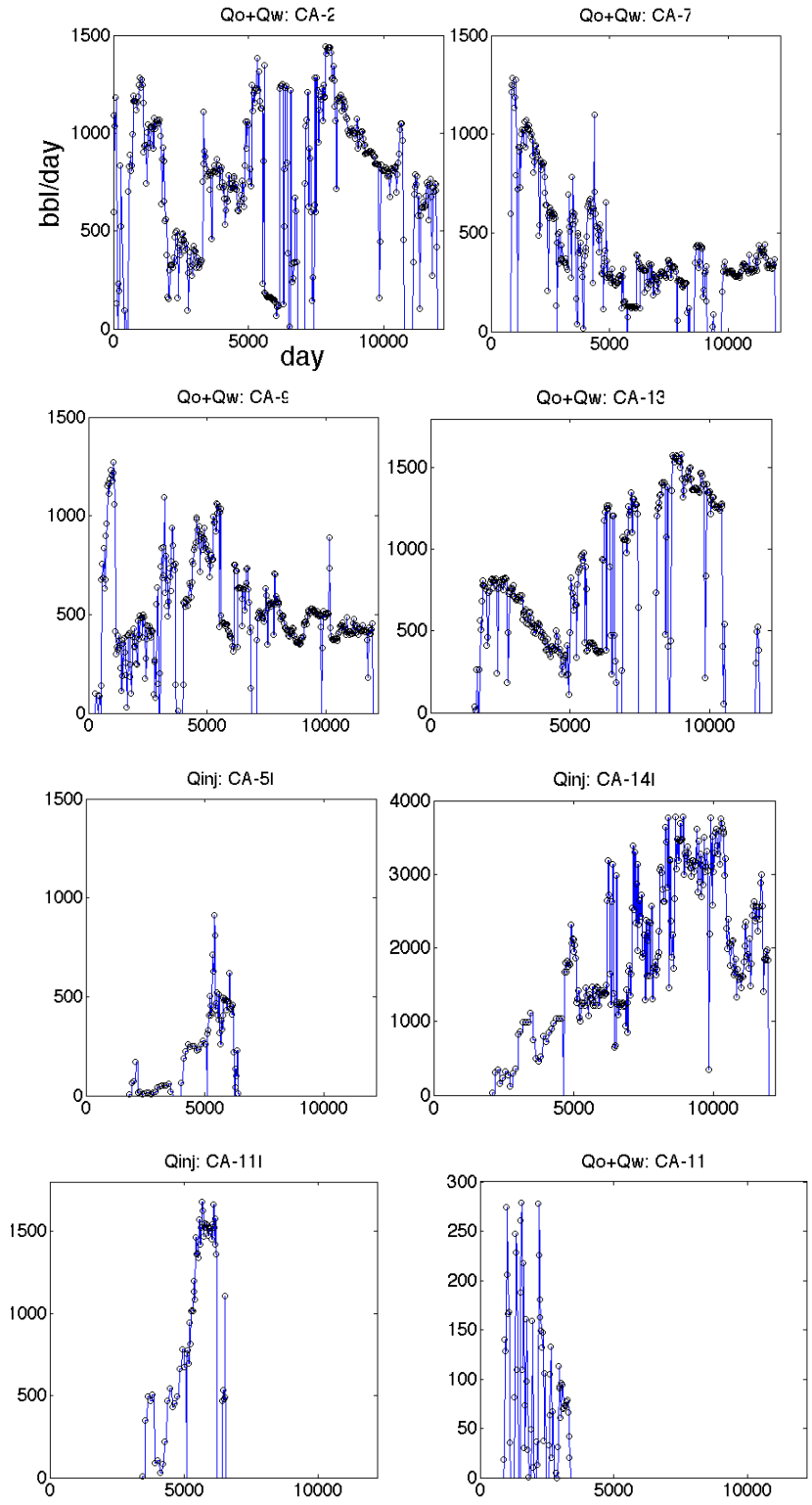

Figure 4.2.7: Liquid flow rates (Qo + Qw) for 5 producers (CA-2, CA-7, CA-9, CA-13, CA-11) and 3 injectors (CA-5I, CA-14I, CA-11I) out of the 19 Cavone wells from the coupled simulation. Wells are able to produce and inject at the historical rates as shown by the good agreement between the dotted curves (historical rates) and the solid curves (simulated rates).

We plot the pressure field from the coupled simulation in Figure 4.2.8. Since the size of the flow compartment is small, i.e. the three layers of the reservoir, a significant pressure drop due to production extends over a substantial portion of the reservoir. Also, the magnitude of the pressure drop around producers is larger than in the second case that allows deeper flow. The pressure increase in the vicinity of injection well CA14 is comparable to that observed (see Figure 4.5), but the decreases in the pressure in the vicinity of the producers is about an order of magnitude larger than the 15 – 20 bars discussed in Section 4, suggesting that lateral pressure support only is insufficient to explain observations.

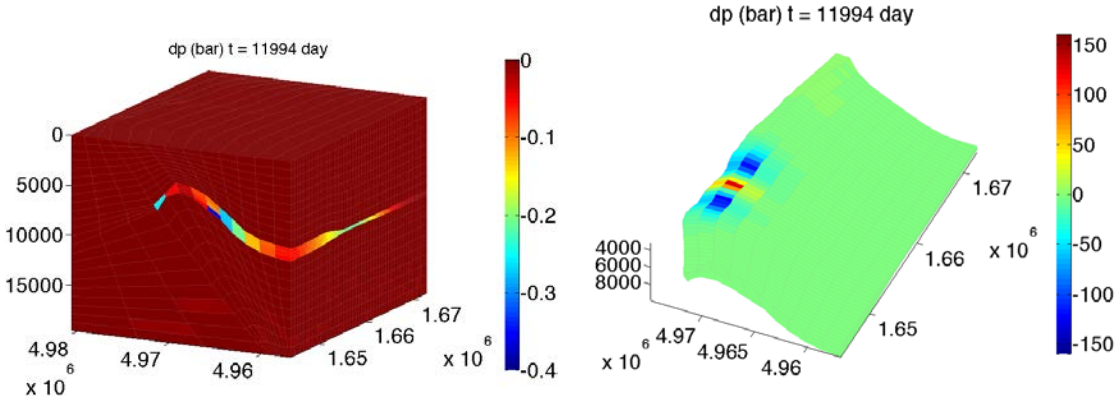

Figure 4.2.8: Changes in pressure in the domain (left) and in the reservoir layers (right) in the case with lateral aquifer support only.

The large pressure changes near the wells continue to the intersection of the reservoir with the Mirandola fault. (Equation (29)). In Figure 4.2.9 we plot the pressure on the hanging wall side, i.e. the side where the Cavone field is located.

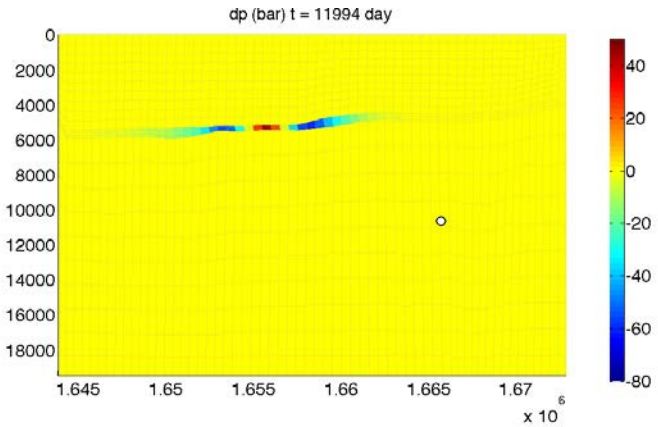

Figure 4.2.9: Change in pressure on the hanging wall side of the fault for the case with lateral aquifer support. The 29 May, 2012 hypocenter location is shown with a white circle. The 20 May, 2012 hypocenter location is on a different fault, for which the pressure changes from reservoir operations is predicted to be zero in this model.

To determine the stability of the Mirandola fault, we are interested in evaluating the change in Coulomb stress (dCFF) on the fault due to change in pressure and stress (Reasenberg and Simpson, 1992):

$$\mathrm{dCFF} = \Delta\tau + \mu_f \Delta\sigma'_n. \qquad \text{Eq. 30}$$

where $\Delta\tau$ is the change in the up-dip shear traction, $\mu_f = 0.6$ is the coefficient of friction on the fault, and $\Delta\sigma'_n$ is the change in effective normal traction on the fault. Note that our sign convention is such that tension is positive and compression is negative. Positive dCFF indicates destabilization of the fault.

Fault stability can be assessed by evaluating the stability criterion on both sides of the fault separately. The side of the fault where the criterion is met first determines the fault stability (Jha and Juanes, 2014). We compute dCFF on the fault using the maximum of the two fluid pressures on the two sides (the footwall and the hanging wall) of the fault (Equation (29)).

We plot fault tractions (along-dip shear traction and normal traction) and dCFF at the end of the simulation in Figure 4.2.10. The reservoir compartment contracts as a result of pressure depletion due to net production of fluids. This affects both the shear and the normal traction on the fault. While the pressure changes are confined to the reservoir layers, the region of influence extends above and below the reservoir because of mechanical force balance. Outside the reservoir, contraction leads to up-dip shear traction on the layers below the reservoir and down-dip shear traction on the layers above the reservoir. In the neighborhood of the CA-14I injector location, the changes are opposite because injection leads to expansion of the reservoir.

With regard to the normal traction, reservoir contraction leads to a drop in the effective compressive normal traction (red color in Figure 4.2.10) in the reservoir depth interval as well as below the reservoir, except near CA-14I where injection-induced expansion causes an increase in the effective normal compression above and below the reservoir (blue in Figure 4.2.10).

The change in Coulomb stress (dCFF) is a sum of the change in the up-dip shear traction and the change in the effective normal traction scaled with the fault friction coefficient (Equation (30)). We see from Figure 4.2.10 that dCFF is positive below the reservoir and negative above the reservoir. The sign reverses near the CA-14I injector.

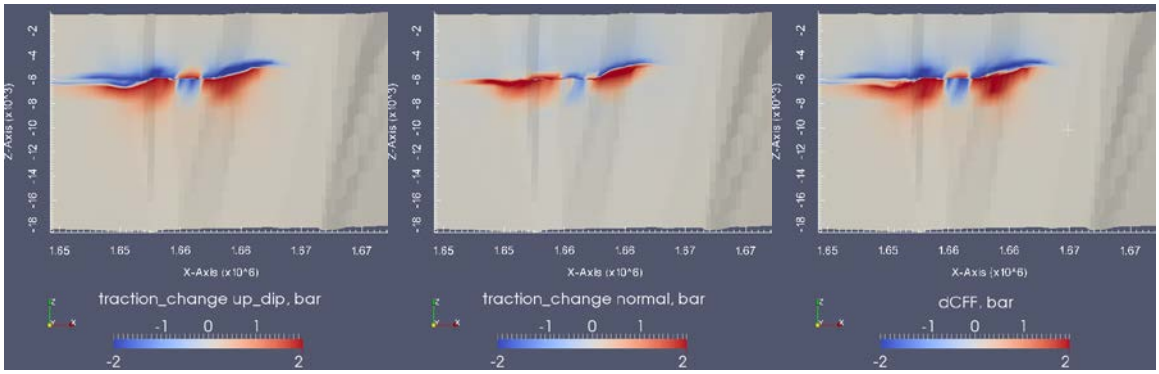

Figure 4.2.10: Changes in the fault tractions (left: change in up-dip traction; center: change in effective normal traction) and the Coulomb stress (dCFF, right) on the fault at t = 11994 day from the simulation with lateral aquifer support and no bottom aquifer support. The positive region of dCFF, which indicates fault instability, has expanded below the reservoir because of the increase in up-dip shear traction due to contraction of the reservoir compartment.

The interpretation of these results requires careful consideration of the effective stress changes inside and outside the reservoir. The conventional interpretation of *production-driven* stress changes is that the pressure decreases while the total (overburden) stress remains constant and, as a result, this leads to an increase in the compressive effective stress that stabilizes a fault plane with virtually any orientation or dip angle. While this conventional interpretation is fundamentally correct inside the reservoir, it is not necessarily correct for faults bounding the reservoir. If the fault is not conductive, as it is assumed here based on observational constraints, the pressure changes on the outside face of the fault are zero (Figure 4.2.8). Therefore, on the outside face of the fault, fluid production from the reservoir does *not* necessarily lead to an increase in compressive effective stress. Changes in effective stress on the outside face depend on the poroelastic effects from reservoir depletion (i.e., contraction of the reservoir volume). From Figure 4.2.10 (center), we observe that the effect of net fluid production is a reduction in compressive effective stress on the outside face of the Mirandola fault below the reservoir, and an increase above the reservoir.

The effect of *fluid injection* also requires careful consideration of the changes in effective stress. Fluid injection leads to an increase in pore pressure inside the reservoir and, as a result, a tendency to reduce the compressive effective stress on the inside face of the fault. Thus, while the arguments made above regarding the poroelastic effects apply (with reversed signed) above and below the reservoir, fluid injection will virtually always lead to a reduction in compressive effect stress within the reservoir layers, as evidenced by the small red-colored region in Figure 4.2.10 (center).

These calculations show that production-induced pressure depletion, if the reservoir were isolated from the aquifer below, could lead to positive changes in the Coulomb stress of up to 2 - 3 bars on the fault bounding the reservoir within a few km of the reservoir, beyond which it falls off rapidly. Static stress changes of this magnitude would tend to destabilize the fault.

However, it is important to note that these stress changes have accumulated over more than two decades of production, leading to average rates of change of Coulomb stress < 0.15 bars/yr. In addition, the region of destabilization is limited to a region < 2 km down dip of the reservoir and a few km in width; Coulomb stress changes outside this region being much smaller. As can be seen by comparison to Figure 4.2.15, the extent of the region depends on the magnitude of the pressure drop, which further depends on aquifer support and flow barriers in the reservoir.

We also track pressure and stress changes at the hypocenter location (1664840 m, 4968610 m, -10200 m) on the Mirandola fault. The hypocenter is located in the bottom aquifer. Since the reservoir layer is not in communication with the bottom aquifer, the pressure change at the hypocenter is zero in this case, which translates into a smaller drop in the effective normal traction and the Coulomb stress at the hypocenter (Fig. 4.2.11). These changes are due to poroelastic effects. The decreasing trend in dCFF initially occurs before the pressure signal in the reservoir arrives to the neighborhood of this point. During this period, a phenomenon similar to the Mandel-Cryer effect (Mandel, 1953; Abousleiman et al., 1996; Jha and Juanes, 2014) is responsible for the increase in compressive effective normal stress and accompanying reduction in dCFF. At time approximately 5000 days, the pressure wave from production arrives to the reservoir region above the hypocenter, and acts to contract this region and lead to a reversal in trend in dCFF due to a reduction in compressive effective stress on the outside face of the fault and the generation of small up-dip tractions, as explained above. Note that overall, dCFF is negative (suggesting a stabilizing effect of reservoir production and injection on this region of the fault) and of very small magnitude (< 0.01 bar).

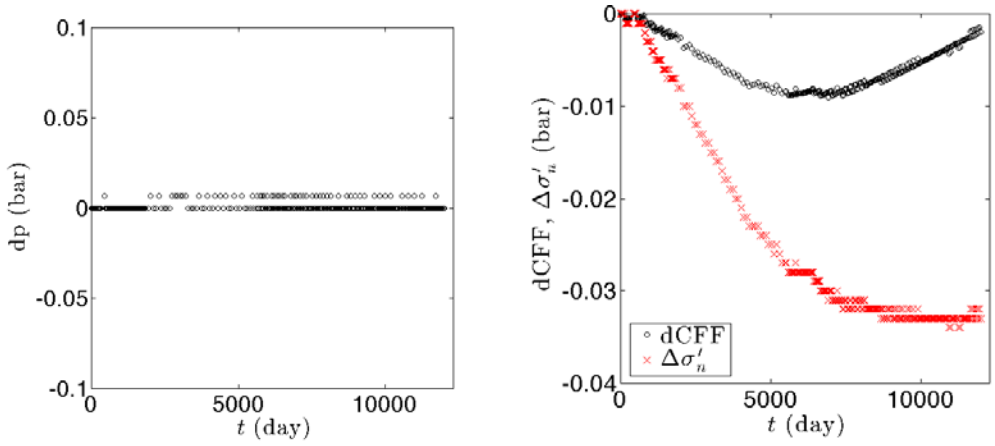

Figure 4.2.11: Change in the pressure and the Coulomb stress (dCFF) at the May 29th hypocenter on the Mirandola fault. The pressure change is almost zero because there is no communication between the reservoir and the bottom aquifer. The change in Coulomb stress is very small suggesting no effect of production and injection at the hypocenter in this model.

Surface displacements from the simulation are plotted in Figure 4.2.12. As expected from the overall decrease in volume from production, the *y* (north) displacements show motion directed towards the reservoir; the region above the reservoir (east side of the domain) shows overal subsidence, but less subsidence in the area above the Cavone 14 injector. The subsidence is smaller than the estimated 1 mm/year subsidence rate in the field. One possible reason is that we choose a constant value of 55 GPa for the Young modulus in the entire domain when, in reality, the rock may be significantly softer near the ground surface.

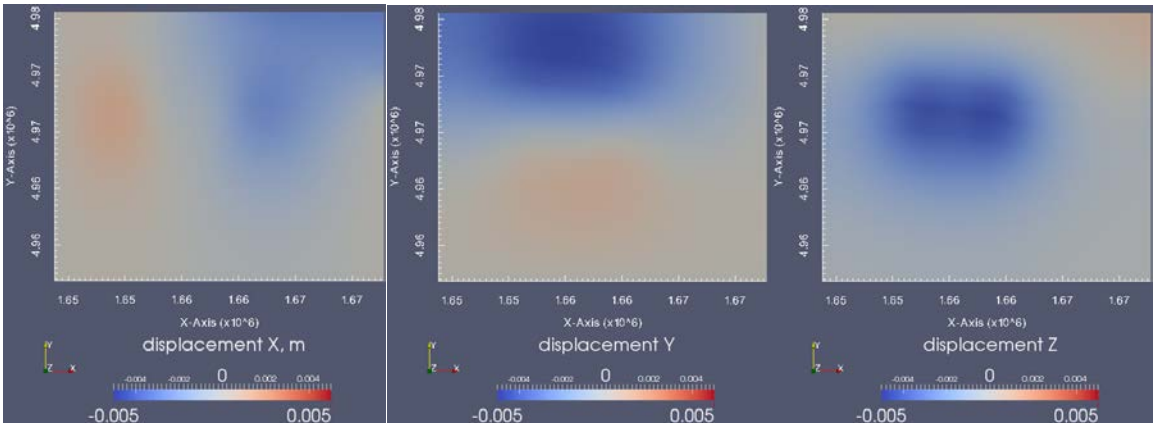

Figure 4.2.12: Displacement field on the ground surface at the end of simulation at t = 11994 day. Pressure depletion in the reservoir leads to formation of a subsidence bowl above the anticline. Left: east-west displacement; Middle: north-south displacement; Right: vertical displacement. Magnitudes are in meters. Maximum subsidence is about 5 mm.

Case 2: Bottom and lateral aquifer support

In this case, as is suggested by the observations of permeability in cores and the temperature profile in the injection test, we assume that the reservoir is communicating with the bottom aquifer, which is composed of layers below the oil-water contact (Figure 4.2.13). Bottom aquifer support leads to a smaller pressure drop around the producers and a smaller pressure rise around the injectors as seen by comparing Figure 4.2.8 and Figure 4.2.13. The pressure drops at the producing wells are now much closer to the observed pressure drops, although the pressure increase predicted for injector CA 14 is too small. (This may be evidence for lateral heterogeneity in the permeability structure, consistent with the fall-off test, as discussed in Section 4.1). In this simulation, pressure changes on the hanging-wall side of the Mirandola fault from production and injection propagate further down compared with the previous case, but the magnitude of the pressure variations is much smaller (Figure 4.2.14).

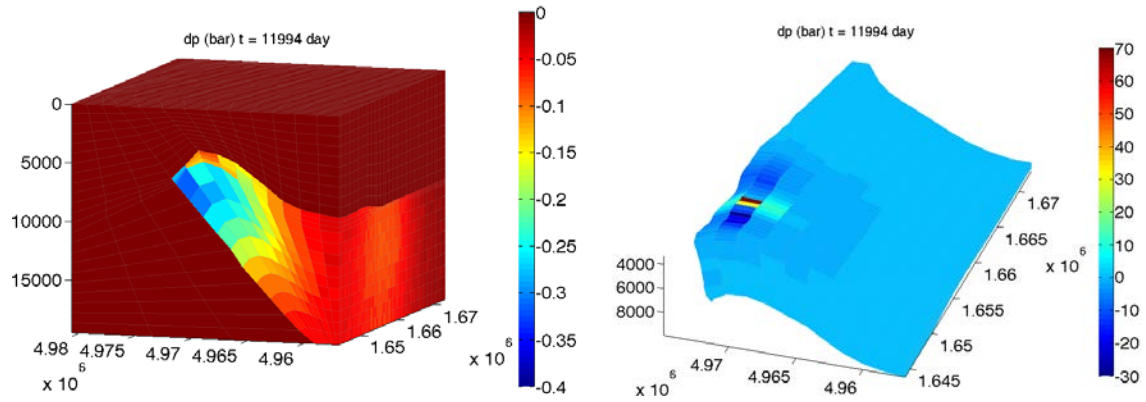

Figure 4.2.13: Change in pressure (dp) in the domain (left) and within the reservoir (right) at the end of the simulation. The oil reservoir at the top of the anticline is receiving pressure support from the aquifer below, which leads to a smaller pressure drop in the reservoir compared to the case without bottom aquifer support. The aquifer pressure decreases as water moves up to support the depletion in the reservoir. Within the reservoir, the pressure has increased in the injector cells and it has decreased in the producer cells.

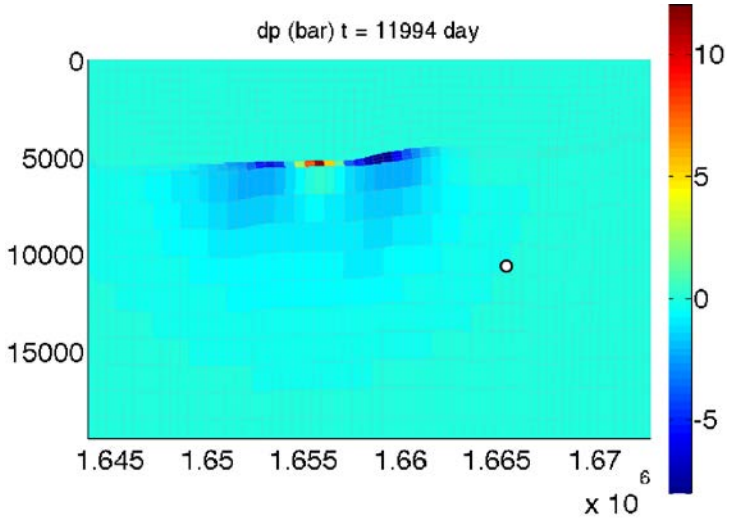

Figure 4.2.14: Changes in pressure (bar) on the hanging wall side of the fault surface. The pressure changes are concentrated in the reservoir layers around the well completions. However, pressure changes diffuse into the aquifer below with time. The 29 May, 2012 hypocenter location is shown with a white circle. The 20 May, 2012 hypocenter location is on a different fault, for which the pressure changes from reservoir operations is predicted to be zero in this model.

We plot the changes in fault tractions and Coulomb stress (dCFF) on the fault in Figure 4.2.15. The region of instability on the fault, based on the positive change in Coulomb stress, is much smaller in magnitude (< 0.5 bars) and also of more limited spatial extent in the current simulation compared to the previous simulation. This is because the shear traction is smaller as a result of a smaller pressure drop (Figure 4.2.14). For either case, the dimensions of the regions with nontrivial changes in Coulomb stress, a few square-kilometers, are much smaller than the rupture areas of the 20 and 29 May 2012 earthquakes (~ 250 km^2).

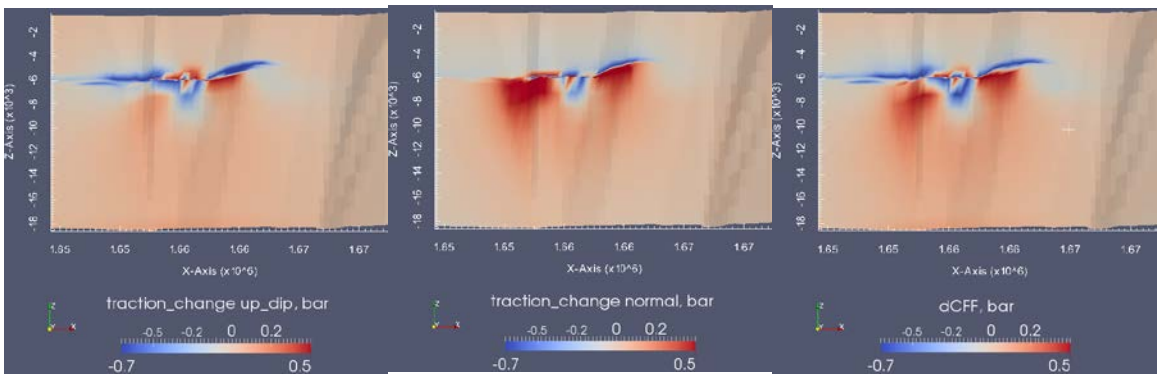

Figure 4.2.15: Changes in the effective tractions and the Coulomb stress (dCFF) on the fault at t = 11994 day for the case with bottom aquifer support. The change in the effective normal traction is positive near producers and negative near injectors because pressure depletion leads to contraction of the reservoir and pressure increase leads to increased compression on the fault. The white cross mark on the dCFF plot denotes the hypocenter location.

For this model, the *rates* of change, ~ 0.02 bars/yr, are comparable to the tectonic loading rates, so should have much less of an impact on seismicity than the changes in stress associated with the May, 2012 aftershock sequence.. Also, the slip and changes in Coulomb stresses from these large events may well have completely overshadowed the changes in Coulomb stress from production. With this in mind, it is useful to consider possible observational constraints.

The careful studies of earthquake locations in the time interval since the May 2012 earthquake sequence are useful in this regard. The cross sections plotted in Figure 2.3.3 show no concentration in the regions of increased Coulomb stress in Figures 4.2.10 or 4.2.15. From this we can conclude that the rapid changes in Coulomb stress on the Mirandola fault from the May 2012 earthquake sequence were much more important than the stress changes that slowly accumulated over the lifetime of production in the Cavone field.

We plot the time evolution of change in pressure (dp) and change in Coulomb stress (dCFF) at the hypocenter of the 29 May, 2012 aftershock in Figure 4.2.16. The change in pressure at the hypocenter is not zero because of the hydraulic communication between the reservoir and the bottom aquifer. However, dCFF is smaller than the pressure drop and it has a non-monotonic trend in time. For the first 4000 days, the pressure does not change significantly, while the effective normal traction and the Coulomb stress decreases due to poroelastic expansion. After 5000 days, the pressure depletion front reaches the hypocenter and the pressure starts to decrease. The compressive effective normal traction starts to decrease at the outside face of the fault because of contraction of the aquifer and, as a result, dCFF increases.

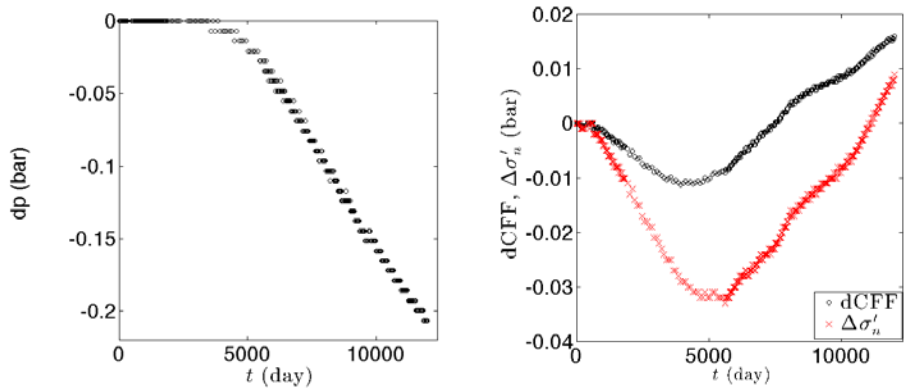

Figure 4.2.16: Time evolution of changes in pressure and the Coulomb stress at the hypocenter location.

We also plot the surface displacement maps from the simulation in Figure 4.2.17. The subsidence is smaller than in the previous case because the pressure drop is smaller with the bottom aquifer support.

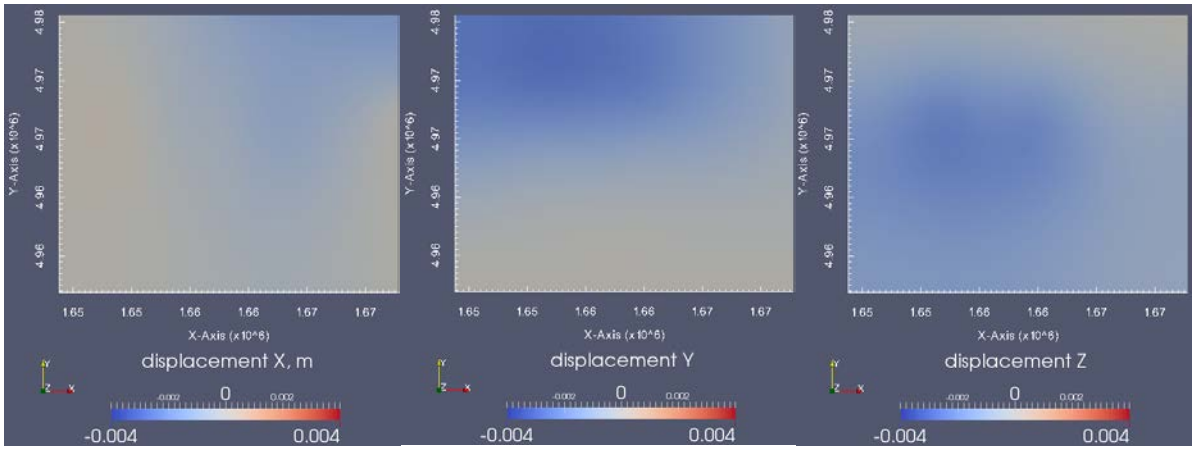

Figure 4.2.17: Displacement field on the ground surface at the end of simulation at t = 11994 day. Pressure depletion in the reservoir leads to subsidence. Left: east-west displacement; Middle: north-south displacement; Right: vertical displacement. Magnitudes are in meters. Maximum subsidence is less than 3 mm. Notice that subsidence spreads over a larger area of the hanging wall block compared to Figure 4.2.12 because of the pressure drop in the bottom aquifer.

4.3 Synthesis and Conclusions from the Dynamic Modeling

The present study illustrates the application of state of the art simulation technology for dynamic modeling of coupled flow and geomechanics, and its implications for the interpretation of induced seismicity. We constructed a simplified model of the Cavone field and its geologic surroundings to investigate the effect of fluid production and injection on the stress field within the reservoir, and on the Mirandola fault.

The methodology put forward in this study relies on the solution of the coupled equations of reservoir fluid flow and geomechanical deformation in the presence of faults (Jha and Juanes, 2014). The simulations of coupled multiphase flow and poromechanics of faults have been performed with a two-way coupled simulator that interlaces a geomechanics simulator (PyLith) with a multiphase flow simulator (GPRS). Our approach enjoys the following features:

1. It is computationally efficient because it relies on a sequential solution of the two-way coupled problem.
2. It is unconditionally stable, due to the use of the fixed-stress sequential split between multiphase flow and deformation. The model accounts rigorously for multiphase flow effects through a fully nonlinear poromechanics formulation.
3. It represents faults as surfaces embedded in a three-dimensional domain, therefore allowing for a discontinuous displacement field across the fault (fault slip). Our approach elucidates the role of the pressure discontinuity across the fault on the stability of the fault through the definition of a "fault pressure."
4. It incorporates realistic fault constitutive behavior, such as the rate- and state-dependent friction model, capable of simulating runaway fault slip typical of earthquakes.

Due to the severe time constraints for this study, we adopted the following assumptions:

1. We consider only the Mirandola fault, although it is known that other faults exist, and could play a role both for stress relaxation, and limiting pressure propagation.
2. We employ a fairly coarse computational mesh, due to the intrinsic computational cost of solving the set of coupled poromechanical equations and the need to extend the model to include the overburden (to the ground surface), the underburden (to a depth of 20 km) and the sideburden (to distances for which the boundary conditions do not greatly affect the pressures and stresses in the locations of interest).
3. We employ only approximate initial and boundary conditions, which could be refined especially in conjunction with a finer grid.
4. We use uniform rock properties.
5. We use the exact fluid production and injection rates, but did not attempt to perform history matching of well bottom-hole pressures or water-cuts.

While it is clear that more time would allow us to extend the model fidelity and sophistication, we believe that the current model is very informative, and provides insight into the mechanistic link between the reservoir fluid production/injection and its geomechanical behavior.

We perform simulations for two alternative cases: one which is very simple and instructive in which the aquifer support is limited to the reservoir layer (Case 1), and one which we consider to be more realistic based on Section 4.1 in which the aquifer support is both from the lateral

aquifer and the bottom aquifer (Case 2). From the current models, we can extract the following finding and conclusions:

1. In Case 1, as expected, the pressure variations are limited to the reservoir layers. Net production leads to overall pressure depletion, with local increases in pressure, in the neighborhood of the Cavone 14 injector well (Figure 4.2.8). This pattern is reflected in the pressure variations on the hanging wall of the Mirandola fault (Figure 4.2.9). However, on the foot wall, pressure variations are zero due to the assumption of an nonconductive fault.
2. These production/injection-driven pressure variations lead to a characteristic signature of up-dip and normal stress changes on the Mirandola fault. In principle, the net production tends to stabilize faults *within* the reservoir layer. However, for a bounding fault, the discontinuity in pore pressure means that there is a discontinuity in *effective* normal stress and that, therefore, the Coulomb failure criterion must be evaluated locally on both sides of the fault. Net production leads to contraction that creates (1) down-dip tractions above the reservoir, and up-dip tractions below; and (2) a reduction in compressive effective stress on the outside face of the Mirandola fault below the reservoir, and an increase above the reservoir. The result of these effects is a change in Coulomb stress (dCFF) that is positive in the reservoir depth interval as well as below the reservoir (Figure 4.2.10) and negative in the region above the reservoir.
3. These calculations suggest that production-induced pressure depletion in an isolated reservoir could lead to the accumulation of positive changes in the Coulomb stress of up to 3 bars on the fault bounding the reservoir within a few km of the reservoir, beyond which it falls off rapidly. Static stress changes of this magnitude, if they occurred over a short time, would tend to destabilize the fault. The region of destabilization is limited to the region around the reservoir experiencing the pressure changes—a region that has not experienced increased seismicity during over 20 years of operation. The changes in Coulomb stress in the region near the May 29th hypocenter on the Mirandola fault are stabilizing and very small (< 0.01 bar) suggesting no effect of production and injection at the hypocenter. The May 20th hypocenter is on a different fault and farther from the Cavone field, outside the domain of the geomechanical study, and for which the pressure changes from reservoir operations is predicted to be zero in our model.
4. In Case 2, we assume, as suggested in Section 4.1, that the reservoir is communicating with the bottom aquifer, which is composed of layers below the oil-water contact. Bottom aquifer support leads to a smaller pressure drop around the producers and a smaller pressure rise around the injectors as seen by comparing Figure 4.2.8 and Figure 4.2.13.
5. The magnitude of the total Coulomb stress change accumulating over more than 2 decades is < 0.5 bars. The average stressing rate is ~ 0.02 bars/yr, comparable to the tectonic stressing rate. The size of the region of instability on the fault, based on the positive change in Coulomb stress, is smaller in Case 2 than in Case 1. This is because the shear traction is smaller as a result of a smaller pressure drop (Figure 4.2.14).

These models are likely conservative regarding the stability of the Mirandola fault. The main reason is that other faults that are known to exist have not been included. These faults could both prevent pressure variations from reaching the Mirandola fault, and moreover release stress in case they are activated before a seismic event occurs in the Mirandola fault.

Except within a few hundred meters of Cavone 14 injector well, the fluid pressure within the reservoir is dominated by the net depletion of the field. Beyond that distance from the injection well the pressure drops substantially, decreasing the likelihood of tectonic earthquakes occurring within the region in hydraulic communication with the reservoir. Outside the reservoir, the stresses resulting from contraction of the reservoir are in a sense to promote earthquake activity. However, the loading rate in our preferred model, < 0.02 bars/yr, is comparable to the rate at which tectonic stress accumulates. The expected increase in seismicity rate is much less than the increase in seismicity rate from the impulsive stress changes associated with the May, 2012 earthquake sequence. In addition, analysis of the locations of aftershocks of the May 2012 sequence shows a lack of seismicity in the area where the stressing rates from contraction of the reservoir are largest. From this we can conclude that the rapid changes in Coulomb stress on the Mirandola fault from the May 2012 earthquake sequence were much more important than the stress changes that slowly accumulated over the lifetime of production in the Cavone field.

REFERENCES

Aagaard, B., S. Kientz, M. Knepley, L. Strand, and C. Williams (2012), PyLith User Manual, Version 1.8.0, Comput. Infrastruct. for Geodyn., Univ. of Calif., Davis, Calif.

Aagaard, B. T., M. G. Knepley, and C. A. Williams (2013), A domain decomposition approach to implementing fault slip in finite-element models of quasi-static and dynamic crustal deformation, J. Geophys. Res. Solid Earth, 118, 3059–3079, doi:10.1002/jgrb.50217.

Abousleiman, Y., A. H.-D. Cheng, L. Cui, E. Detournay, and J.-C. Roegiers (1996), Mandel's problem revisited, Geotechnique, 46, 187–195.

Ake, J., K. Mahrer, D. O'Connell and L. Block (2005). Deep-injection and closely monitored induced seismicity at Paradox Valley, Colorado, *Bull. Seismol. Soc. Amer., 95*, 664-683, doi:10.1785/0120040072.

Anderson, E. M. (1951), The Dynamics of Faulting and Dyke Formation With Application to Britain, Oliver and Boyd, New York, N. Y.

Armero, F. (1999), Formulation and finite element implementation of a multiplicative model of coupled poro-plasticity at finite strains under fully saturated conditions, Comput. Methods Appl. Mech. Eng., 171, 205–241.

Armero, F., and J. C. Simo (1992), A new unconditionally stable fractional step method for non-linear coupled thermomechanical problems, Int. J. Numer. Methods Eng., 35, 737–766.

Armero, F., and J. C. Simo (1993), A priori stability estimates and unconditionally stable product formula algorithms for nonlinear coupled thermoplasticity, Int. J. Plasticity, 9, 749–782.

Aziz, K., and A. Settari (1979), Petroleum Reservoir Simulation, Elsevier, London, U. K.

Barton, C. A., M. D. Zoback, and D. Moos (1995). Fluid flow along potentially active faults in crystalline rock: *Geology*, *23*, 683-686

Beall, J.J. M.A. Stark, J.L. Bill Smith and A. Kirkpatrick. 1999. Microearthquakes in the SE Geysers before and after SEGEP Injection. Geothermal Resources Council, Transactions 23: 253-257.

Bear, J. (1972), Dynamics of Fluids in Porous Media, John Wiley, New York, N. Y.

Bear, J., and M. Y. Corapcioglu (1981), Mathematical model for regional land subsidence due to water pumping, Water Resour. Res., 17, 937–958.

Beeler, N. M., R. W. Simpson, S. H. Hickman, and D. A. Lockner (2000), Pore fluid pressure, apparent friction, and Coulomb failure, J. Geophys. Res., 105, 25,533–25,542.

Beer, G. (1985), An isoparametric joint/interface element for finite element analysis, Int. J. Numer. Methods Eng., 21, 585–600.

Biot, M. A. (1941), General theory of three-dimensional consolidation, J. Appl. Phys., 12, 155–164.

Birkholzer, J. T., and Q. Zhou (2009), Basin-scale hydrogeologic impacts of CO2 storage: Capacity and regulatory implications, Int. J. Greenh. Gas Control, 3, 745–756.

Bishop, A. W. (1959), The principle of effective stress, Tekniske Ukeblad, 39, 859–863.

Bishop, A. W., and G. E. Blight (1963), Some aspects of effective stress in saturated and partly saturated soils, Geotechnique, 13, 177–197.

Block, L.V., C.K. Wood, W.L. Yeck and V.M. King (2014). The 24 January 2013 M_L 4.4 Earthquake near Paradox, Colorado, and Its Relation to Deep Well Injection. *Seism. Res. Lett., May/June 2014, v. 85, p. 609-624, doi:10.1785/0220130188*

Boccaletti, M., G. Corti, and L. Martelli (2010). Recent and active tectonics of the external zone of the Northern Apennines (Italy), *Geol. Rundsch. Z. Allg. Geol.*, *100*, 1331-1348, doi: 10.1007/ s00531-010-0545-y

Bonini, M. (2013) Fluid seepage variability across the external Northern Apennines (Italy): Structural controls with seismotectonic and geodynamic implications, *Tectonophysics*, *590*, 151-174.

Brodsky, E. E., E. Roeloffs, E. Woodcock, I. Gall and M. Manga (2003). A mechanism for sustained groundwater pressure changes induced by distant earthquakes. *J. Geophys. Res., 108*(B8), 2390. doi:doi:10.1029/2002JB002321

Brodsky, E. E., and L. J. Lajoie (2013), Anthropogenic seismicity rates and operational parameters at the Salton Sea Geothermal Field, Science, 341, 543–546.

Burrato, P., F. Ciucci, and G. Valensise (2003). An inventory of river anomalies in the Po Plain, Northern Italy: evidence for active blind thrust faulting, *Ann. Geophys.*, *46*, 5.

Byerlee, J. (1978). Friction of rocks .*Pure Appl. Geophys. 116*, 615–626.

Caine, J. S., and C. B. Forster (1999), Faults and Subsurface Fluid Flow in the Shallow Crust, Geophys. Monogr. Ser., vol. 113, edited by W. C. Haneberg et al., AGU, Washington, D. C.

Cao, H. (2002), Development of techniques for general purpose simulators, PhD thesis, Stanford Univ., Stanford, Calif.

Cappa, F., and J. Rutqvist (2011a), Impact of CO2 geological sequestration on the nucleation of earthquakes, Geophys. Res. Lett., 38, L17313, doi:10.1029/2011GL048487.

Cappa, F., and J. Rutqvist (2011b), Modeling of coupled deformation and permeability evolution during fault reactivation induced by deep underground injection of CO2, Int. J. Greenh. Gas Control, 5, 336–346.

Carder, D. S. (1945), Seismic investigations in the Boulder Dam area, 1940–1944, and the influence of reservoir loading on earthquake activity, Bull. Seismol. Soc. Am., ,,,,,,35, 175–192.

Carol, I., A. Gens, and E. E. Alonso (1985), A three dimensional elastoplastic joint element, in Fundamentals of Rock Joints, pp. 441–451, Centek, Lulea, Sweden.

Castelli, V., F. Bernardini, R. Camassi, C. H. Caracciolo, E. Ercolani, and L. Postpischl (2012). Looking for missing earthquake traces in the Ferrara-Modena plain: an update on historical seismicity. *Ann. Geophys. 55, 4, 519-524. doi:10.4401/ag-6110*

Cesca, S. T. Braun, F. Maccaferri, L. Passarelli, E. Rivalta and T. Dahm. (2013). Source modeling of the M 5-6 Emilia-Romagna, Italy earthquakes (2012 May 20-29). *GJI, doi:10.1093/gji/ggt069*

Chester, F. M., J. P. Evans, and R. Biegel (1993), Internal structure and weakening mechanisms of the San Andreas Fault, J. Geophys. Res., 98, 771–786.

Chiaramonte, L., M. D. Zoback, J. Friedmann, and V. Stamp (2008), Seal integrity and feasibility of CO2 sequestration in the Teapot Dome EOR pilot: Geomechanical site characterization, Environ. Geol., 54(8), 1667–1675.

Ciaccio, M.G., and C. Chiarabba (2002). Tomographic models and seismotectonics of the Reggio Imilia region, Italy, *Tectonophysics, 344*, 261–276.

Convertito, V., Catalli, F., & Emolo, A. (2013). Combining stress transfer and source directivity: the case of the 2012 Emilia seismic sequence. *Scientific reports*, *3*.

Coussy, O. (1995), Mechanics of Porous Continua, John Wiley, Chichester, U. K.

Coussy, O. (2004), Poromechanics, John Wiley, Chichester, U. K.

Coussy, O. (2005), Poromechanics of freezing materials, J. Mech. Phys. Solids, 53, 1689–1718.

Coussy, O., R. Eymard, and T. Lassabatere (1998), Constitutive modeling of unsaturated drying deformable materials, J. Eng. Mech., 124(6), 658–557.

Coussy, O., P. Dangla, T. Lassabatere, and V. Baroghel-Bouny (2004), The equivalent pore pressure and the swelling and shrinkage of cement-based materials, Mater. Struct., 37, 15–20.

CUBIT (2013), CUBIT 13.2 User Documentation, Sandia Natl. Lab., Albuquerque, N. M.

Dean, R. H., X. Gai, C. M. Stone, and S. E. Minkoff (2006), A comparison of techniques for coupling porous flow and geomechanics, Soc. Pet. Eng. J., 11, 132–140.

Devoti, R ., A. Esposito, G. Pietrantonio, A. R . Pisani, and F. Riguzzi (2011). Evidence of large scale deformation patterns from GPS data in the Italian subduction boundary, *Earth Planet. Sci. Lett. 311*, 230-241, doi: 10.1016/j.epsl.2011.09.034.

Dieterich, J. H. (1979a). Modeling of rock friction 1. Experimental results and constitutive equations, *J. Geophys. Res.*, *84*(B5), 2161-2168.

Dieterich, J. H. (1979b). Earthquake nucleation on faults with rate- and state-dependent strength, *Tectonophysics, 211*, 115-134,

Dieterich, J. H. (1992). Earthquake nucleation on faults with rate- and state-dependent friction, *Tectonophysics, 211*, 115-134.

Dieterich, J. H. (1994). A constitutive law for rate of earthquake production and its application to earthquake clustering. *J. Geophys. Res. 99*, 2601–2618.

Dieterich, J. H. and B. D. Kilgore (1994). Direct observation of frictional contacts: New insights for state-dependent properties. *Pure Appl. Geophys., 143*(1), 283-302.

Dieterich, J. H. (2007). Applications of rate- and state-dependent friction to models of fault slip and earthquake occurrence, *Treatise on Geophysics, Vol 4*, Elsevier, 107-129.

DISS WORKING GROUP (2007) - *Database of Individual Seismogenic Sources (version 3.0.4): A compilation of potential sources for earthquakes larger than M 5.5 in Italy and surrounding areas*. Available at: http://www.ingv.it/DISS.

Dolan, J., S. Christofferson and J. H. Shaw (2003). Recognition of Paleoearthquakes on the Puente Hills Blind Thrust Fault, California, *Science, 300:* 115-118.

Elkhoury, J. E., E. E. Brodsky and D. C. Agnew (2006). Seismic waves increase permeability. *Nature*, 441(7097), 1135-1138.

Ellsworth, W. L. (2013), Injection-induced earthquakes, Science, 341, 1–7.

Engelder, T. (2012), Capillary tension and imbibition sequester frack fluid in Marcellus gas shale, Proc. Natl. Acad. Sci. U. S. A., 109(52), E3625.

Felippa, C. A., and K. C. Park (1980), Staggered transient analysis procedures for coupled mechanical systems: Formulation, Comput. Methods Appl. Mech. Eng., 24, 61–111.

Ferronato, M., G. Gambolati, C. Janna, and P. Teatini (2008), Numerical modeling of regional faults in land subsidence prediction above gas/oil reservoirs, Int. J. Numer. Anal. Methods Geomech., 32, 633–657.

Ferronato, M., N. Castelletto, and G. Gambolati (2010), A fully coupled 3-D mixed finite element model of Biot consolidation, J. Comput. Phys., 229(12), 4813–4830.

Fialko, Y., and M. Simons (2000), Deformation and seismicity in the Coso geothermal area, Inyo County, California: Observations and modeling using satellite radar interferometry, J. Geophys. Res., 105, 21,781–21,793.

Freed, A. (2005). Earthquake triggering by static, dynamic, and postseismic stress transfer: Ann.Rev.*EarthPlanet. Sci*., 33, 335–67, doi: 10.1146/annurev.earth.33.092203.122505

Galloway, D. L., and T. J. Burbey (2011), Review: Regional land subsidence accompanying groundwater extraction, Hydrogeol. J., 19, 1459–1486.

Galloway, D. L., K. W. Hudnut, S. E. Ingebritsen, S. P. Phillips, G. Peltzer, F. Rogez, and P. A. Rosen (1998), Detection of aquifer system compaction and land subsidence using interferometric synthetic aperture radar, Antelope Valley, Mojave Desert, California, Water Resour. Res., 34, 2573–2585.

Gambolati, G., and R. A. Freeze (1973), Mathematical simulation of the subsidence of Venice: 1. Theory, Water Resour. Res., 9, 721–733.

Gambolati, G., P. Teatini, D. Bau, and M. Ferronato (2000), The importance of poro-elastic coupling in dynamically active aquifers of the Po river basin, Italy, Water Resour. Res., 36, 2443–2459.

Ganas, A., Z. Roumelioti and K. Chousianitis (2012). Static Stress transfer from the May 20, 2012, M 6.1 Emilia-Romgana (northern Italy) earthquake using a co-seismic slip distribution model. *Ann. Geophys. 55, 4, 655-662. doi: 10.4401/ag-676*

Geertsma, J. (1957), The effect of fluid pressure decline on volumetric change of porous rocks, Trans. AIME, 210, 331–340.

Geertsma, J. (1973a). Land subsidence above compacting oil and gas reservoirs, *Journal of Petroleum Technology, 25*, 734-744.

Geertsma, J. (1973b), A basic theory of subsidence due to reservoir compaction: The homogeneous case, Verhandelingen Kon. Ned. Geol. Mijnbouwk. Gen., 28, 43–62.

Gens, A., I. Carol, and E. E. Alonso (1988), An interface element formulation for the analysis of soil-reinforcement interaction, Comput. Geotech., 7, 133–151.

Glowinsky, R., and P. Le Tallec (1989), Augmented Lagrangian and Operator-Splitting Methods in Nonlinear Mechanics, Soc. Ind. Appl. Math., Philadelphia, Pa.

Gonzalez, P. J., K. F. Tiampo, M. Palano, F. Cannavo, and J. Fernandez (2012), The 2011 Lorca earthquake slip distribution controlled by groundwater crustal unloading, Nat. Geosci., 5, 821–825.

Goodman, R. E., R. L. Taylor, and T. L. Brekke (1968), A model for the mechanics of jointed rock, J. Soil Mech., 94, 637–659.

Grasso, J.-R. (1992,). Mechanics of seismic instabilities induced by the recovery of hydrocarbons, *Pure Appl. Geophys., 139(3-4),* 507–534.

Gray, W. G., and B. A. Schrefler (2001), Thermodynamic approach to effective stress in partially saturated porous media, Eur. J. Mech.-A/Solids, 20, 521–538.

Gupta, H. K. (2002), A review of recent studies of triggered earthquakes by artificial water reservoirs with special emphasis on earthquakes in Koyna, India, Earth Sci. Rev., 58, 279–310.

Hardebeck, J. L., J. J. Nazareth and E. Hauksson (1998). The static stress change triggering model: Constraints from two southern california aftershock sequences. *J. Geophys. Res.*, *103*(24), 427-37. Retrieved from Google Scholar.

Harris, R. A., and R. W. Simpson (1992), Changes in static stress on southern California faults after the 1992 Landers earthquake, Nature, 360, 251–254.

Harris, R. A., R. W. Simpson, and P. A. Reasenberg (1995), Influence of static stress changes on earthquake locations in southern California, Nature, 375, 221–224.

Herrmann, R. B., S.-K. Park and C.-Y. Wang (1981). The Denver earthquakes of 1967-1968, *Bull. Seismol. Soc. Amer., 71*, 731-745.

Hsieh, P. A. and J. D. Bredehoeft (1981). A reservoir analysis of the Denver earthquakes: A case of induced seismicity, *J. Geophys. Res., 86*, 903-920.

Hubbert, M. K., and W. W. Rubey (1959), Role of fluid pressure in mechanics of overthrust faulting. I. Mechanics of fluid-filled porous solids and its application to overthrust faulting, Geol. Soc. Am., 70, 115–166.

Husen, S., R. Taylor, R. B. Smith and H. Healser (2004). Changes in geyser eruption behavior and remotely triggered seismicity in yellowstone national park produced by the 2002 M 7.9 denali fault earthquake, alaska. *Geology*, *32*(6), 537-540. doi:doi:10.1029/2002JB002321

International Seismological Centre, *On-line Bulletin*, http://www.isc.ac.uk, Internatl. Seis. Cent., Thatcham, United Kingdom, 2011.

IPCC (2005), Special Report on Carbon Dioxide Capture and Storage, edited by B. Metz et al., Cambridge Univ. Press, Cambridge, U. K.

Jaeger, J. C., and N. G. W. Cook (1979), Fundamentals of Rock Mechanics, Chapman and Hall, London, U. K.

Jeannin, L., M. Mainguy, R. Masson, and S. Vidal-Gilbert (2007), Accelerating the convergence of coupled geomechanical–reservoir simulations, Int. J. Numer. Anal. Methods Geomech., 31, 1163–1181.

Jha, B., and R. Juanes (2007), A locally conservative finite element framework for the simulation of coupled flow and reservoir geomechanics, Acta Geotech., 2, 139–153.

Jha, B. and R. Juanes (2014), Coupled multiphase flow and poromechanics: a computational model of pore-pressure effects on fault slip and earthquake triggering. Water Resources Research, 50, doi:10.1002/2013WR015175.

Johnson, P. A. and X. Jia (2005). Nonlinear dynamics, granular media and dynamic earthquake triggering. *Nature*, *437*(7060), 871-4. doi:10.1038/nature04015

Juanes, R., J. Samper, and J. Molinero (2002), A general and efficient formulation of fractures and boundary conditions in the finite element method, Int. J. Numer. Methods Eng., 54(12), 1751–1774.

Kagan, Y.Y. and D. D. Jackson, (1991). Long-term earthquake clustering. Geophys. J. Int. 104, 117-133.

Kanamori, H. and E. E. Brodsky (2004). The physics of earthquakes. *Reports on Progress in Physics*, *67*(8), 1429-1496. doi:10.1088/0034-4885/67/8/R03

Keranen, K. M., H. M. Savage, G. A. Abers and E. S. Cochran (2013). Potentially induced earthquakes in Oklahoma, USA: Links between wastewater injection and the 2011 M_w 5.7 earthquake sequence, *Geology*, doi:10.1130/G34045.1

Keranen, K. M., M. Weingarten, G. A. Abers, B. Bekins, S. Ge (2014). Sharp increase in Oklahoma seismicity since 2008 triggered by massive wastewater injection, Science, doi: 10.1126/science.1255802

Khalili, N., F. Geiser, and G. E. Blight (2004), Effective stress in unsaturated soils: A review with new evidence, Int. J. Geomech., 4, 115–126.

Kim, J., H. A. Tchelepi, and R. Juanes (2011a), Stability and convergence of sequential methods for coupled flow and geomechanics: Drained and undrained splits, Comput. Methods Appl. Mech. Eng., 200, 2094–2116.

Kim, J., H. A. Tchelepi, and R. Juanes (2011b), Stability and convergence of sequential methods for coupled flow and geomechanics: Fixed-stress and fixed-strain splits, Comput. Methods Appl. Mech. Eng., 200, 1591–1606.

Kim, J., H. A. Tchelepi, and R. Juanes (2011c), Stability, accuracy and efficiency of sequential methods for coupled flow and geomechanics, Soc. Pet. Eng. J., 16(2), 249–262.

Kim, J., H. A. Tchelepi, and R. Juanes (2013), Rigorous coupling of geomechanics and multiphase flow with strong capillarity, Soc. Pet. Eng. J., 18(6), 1123–1139.

Lackner, K. S. (2003), A guide to CO2 sequestration, Science, 300(5626), 1677–1678.

LaGriT (2013), LaGriT Manual, Los Alamos Natl. Lab., Los Alamos, N. M.

Lambert, A., H. Kao and G. Rogers, 2009. Correlations of tremor activity with tidal stresses in the northern Cascadia subduction zone. Jour Geophys. Res. V. 114. Issue B8, doi: 10.1029/2008JB006038

Lavecchia, G., R. de Nardis, D. Cirillo, F. Brozzetti and P. Boncio (2012). The May-June Ferrara Arc earthquakes (northern Italy): Structural control of the spatial evolution of the seismic sequence and of the surface pattern of coseismic fracture, *Ann. Geophys.*, *55*, 534-540.

Lei, X. Y., G. Swoboda, and G. Zenz (1995), Application of contact-friction interface element to tunnel excavation in faulted rock, Comput. Geotech., 17, 349–370.

Lewis, R. W., and B. A. Schrefler (1998), The Finite Element Method in the Static and Dynamic Deformation and Consolidation of Porous Media, 2nd ed., John Wiley, Chichester, U. K.

Lewis, R. W., and Y. Sukirman (1993), Finite element modelling of three-phase flow in deforming saturated oil reservoirs, Int. J. Numer. Anal. Methods Geomech., 17, 577–598.

Lewis, R. W., A. Makurat, and W. K. S. Pao (2003), Fully coupled modeling of seabed subsidence and reservoir compaction of North Sea oil fields, Hydrogeol. J., 11(1), 142–161.

Li, X., Z. Liu, and R. W. Lewis (2005), Mixed finite element method for coupled thermo-hydro-mechanical process in poro-elastic-plastic media at large strains, Int. J. Numer. Methods Eng., 64(5), 667–708.

Lin, J. and R.S. Stein (2004). Stress triggering in thrust and subduction earthquakes, and stress interaction between the southern San Andreas and nearby thrust and strike-slip faults, *J. Geophys. Res., 109*, B02303, doi:10.1029/2003JB002607.

Linker, M. F. and J. H. Dieterich (1992). Effects of variable normal stress on rock friction-observations and constitutive equations. *J. Geophys. Res., 97*(B4), 4923-4940.

Lockner, D. A., and Beeler, N.M. (2002). Rock failure and earthquakes, *International Handbook of Earthquake & Engineering Seismology part A*, ed W H K Lee et al (San Diego, CA: Academic) pp 505–37.

Lofgren, B. E. (1981), Monitoring crustal deformation in The Geyser Clear Lake region, in Research in The Geysers-Clear Lake Geothermal Area, Northern California, p. 1141, U.S. Gov. Print. Off., Washington, D. C.

Lomnitz, C. (1974), Earthquakes and reservoir impounding: State of the art, Eng. Geol., 8, 191–198.

Mainguy, M., and P. Longuemare (2002), Coupling fluid flow and rock mechanics: Formulations of the partial coupling between reservoir and geomechanics simulators, Oil Gas Sci. Technol., 57, 355–367.

Mandel, J. (1953), Consolidation of soils (mathematical study), Geotechnique, 3, 287–299.

Manga, M., I. Beresnev, E. E. Brodsky, J. E. Elkhoury, D. Elsworth, E. Ingebritsen, and C.-Y. Wang, (2012). Changes in permeability caused by transient stresses: Field observations, experiments, and mechanisms. *Rev. Geophys., 50*(2). doi:10.1029/2011RG000382

Marone, C. (1998). Laboratory-derived friction laws and their application to seismic faulting. *Annu. Rev. Earth Planet. Sci., 26.*

McGarr, A. (1991). On a possible connection between three major earthquakes in California and oil production. *Bull. Seismol. Soc. Amer., 81(3)*: 948-970.

McGarr, A. (2014). Maximum magnitude earthquakes induced by fluid injection, *J. Geophs. Res., 119, doi:10.1002/2013/2-13JB010597*

Mindlin, R. D., (1936). Force at a Point in the Interior of a SemiInfinite Solid, *Physics, 7*, 195-202; doi: 10.1063/1.1745385

Minkoff, S. E., C. M. Stone, S. Bryant, M. Peszynska, and M. F. Wheeler (2003), Coupled fluid flow and geomechanical deformation modeling, J. Pet. Sci. Eng., 38, 37–56.

Molinero, J., J. Samper, and R. Juanes (2002), Numerical modeling of the transient hydrogeological response produced by tunnel construction in fractured bedrocks, Eng. Geol., 64(4), 369–386.

Morris, J. P., R. L. Detwiler, S. J. Friedman, O. Y. Vorobiev, and Y. Hao (2011a), The large-scale geomechanical and hydrogeological effects of multiple CO2 injection sites on formation stability, Int. J. Greenh. Gas Control, 5(1), 69–74.

Morris, J. P., Y. Hao, W. Foxall, and W. McNab (2011b), A study of injection-induced mechanical deformation at the In Salah CO2 storage project, Int. J. Greenh. Gas Control, 5(2), 270–280.

Mossop, A., and P. Segall (1997), Subsidence at The Geysers geothermal field, N. California from a comparison of GPS and leveling surveys, Geophys. Res. Lett., 24, 1839–1842.

Muskat, M. (1949), Physical Principles of Oil Production, McGraw-Hill, New York, N. Y.

Nikooee, E., G. Habibagahi, S. M. Hassanizadeh, and A. Ghahramani (2013), Effective stress in unsaturated soils: A thermodynamic approach based on the interfacial energy and hydromechanical coupling, Transp. Porous Media, 96, 369–396.

NRC (National Research Council, 2012), *Induced Seismicity Potential in Energy Technologies,* Washington, DC: National Academy Press.

Nuth, M., and L. Laloui (2008), Effective stress concept in unsaturated soils: Clarification and validation of a unified framework, Int. J. Numer. Anal. Methods Geomech., 32, 771–801.

Okada, Y. (1985). Surface deformation due to shear and tensile faults in a half-space, Bull. Seismol. Soc. Am. 75, 1135-1154.

Orr, F. M., Jr. (2009), Onshore geologic storage of CO2, Science, 325, 1656–1658.

Pacala, S., and R. Socolow (2004), Stability wedges: Solving the climate problem for the next 50 years with current technologies, Science, 305, 968–972.

Pan, H., and H. Cao (2010), User Manual for General Purpose Research Simulator, Stanford Univ. Pet. Eng. Inst., Stanford, Calif.

Pao, W. K. S., and R. W. Lewis (2002), Three dimensional finite element simulation of three-phase flow in a deforming fissured reservoir, Comput. Methods Appl. Mech. Eng., 191, 2631–2659.

Parsons, T. (2005). A hypothesis for delayed dynamic earthquake triggering. *Geophys. Res. Lett.*, *32*(4). doi:10.1029/2004GL021811

Pezzo, G., J. P., Merryman Boncori, C. Tolomei, S. Salvi, S Atzori, A. Antonioli, E. Trasatti, F. Novali, E. Serpelloni and L. Candela (2013). Coseismic deformation and source modeling of the May 2012 (Northern Italy) earthquakes, *Seism. Res. Lett., 84*, 645-655.

Piccinini, D., N. A. Pino and G. Saccorotti (2012). Source complexity of the May 20, 2012 Mw 5.9, Ferrara (Italy) event, *Ann. Geophys., 55*, 568-573.

Pieri, M. (1983). Three seismic profiles through the Po Plain. In: Bally, A.W. (Ed.), Seismic Expression of Structural Styles. A Picture and Work Atlas: Am. Assoc. *Pet. Geol. Stud. Geol., 15* (3.4.1/8–3.4.1/26).

Pratt, T. L., J. H. Shaw, J. F. Dolan, S. Christofferson, R.A. Williams, J.K. Odum, and A. Plesch (2002), Shallow seismic imaging of folds above the Puente Hills blind-thrust fault, Los Angeles, California, *Geophys. Res. Lett.*, *29*/18-1.

Raleigh, C. B., J.H. Healy and J.D. Bredehoeft (1976). An experiment in earthquake control at

Rangely, Colorado, *Science 191*, 1230-1237.

Reasenberg, P. A., and R. W. Simpson (1992), Response of regional seismicity to the static stress change produced by the Loma Prieta earthquake, Science, 255, 1687–1690.

Rice, J. (1992), Fault Stress States, Pore Pressure Distributions, and the Weakness of the San Andreas Fault, pp. 475–503, Academic Press, London, U. K.

Roeloffs, E. (1996), Poroelastic techniques in the study of earthquake-related hydrologic phenomena, Adv. Geophys., 37, 135–195.

Rutqvist, J., Y. S. Wu, C. F. Tsang, and G. Bodvarsson (2002), A modeling approach for analysis of coupled multiphase fluid flow, heat transfer, and deformation in fractured porous rock, Int. J. Rock Mech. Min. Sci., 39, 429–442.

Rutqvist, J., J. T. Birkholzer, F. Cappa, and C. F. Tsang (2007), Estimating maximum sustainable injection pressure during geological seques- tration of CO2 using coupled fluid flow and geomechanical fault-slip analysis, Energy Convers. Manage., 48, 1798–1807.

Rutqvist, J., J. T. Birkholzer, and C. F. Tsang (2008), Coupled reservoir–geomechanical analysis of the potential for tensile and shear failure associated with CO2 injection in multilayered reservoir–caprock systems, Int. J. Rock Mech. Min. Sci., 45, 132–143.

Rutqvist, J., D. W. Vasco, and L. Myer (2010), Coupled reservoir-geomechanical analysis of CO2 injection and ground deformations at In Salah, Algeria, Int. J. Greenh. Gas Control, 4, 225–230.

Samier, P., and S. Gennaro (2007), A practical iterative scheme for coupling geomechanics with reservoir simulation, paper SPE 107077 presented at SPE Europec/EAGE, Society of Petroleum Engineers, London, U. K.

Schlumberger (2009), Eclipse 100 Reference Manual 2009.1, Schlumberger Inf. Solutions, Houston, Tex.

Scholz, C. H. (1989), Mechanics of faulting, Annu. Rev. Earth Planet. Sci., 17, 309–334.

Scholz, C. H. (1998). Earthquakes and friction laws. *Nature*, *391*, 37-42.

Scognamiglio, L., L. Margheriti, F. M. Mele, E. Tinti, A. Bono, P. De Gori, V. Lauciani, F. P. Lucente, A. G. Mandiello, C. Marcocci, S. Mazza, S. Pintore and M. Quintiliani (2012). The 2012 Pianura Padana Emiliana seimic sequence: Locations, moment tensors and magnitudes, *Ann. Geophys., 55*, 549-559.

Scrocca, D., E. Carminati, C. Doglioni and D. Marcantoni (2007). Slab retreat and active shortening along the central-northern Apennines. In: Lacombe, O., Lavé, J., Roure, F., Verges, J. (Eds.), *Thrust Belts and Foreland Basins: From Fold Kinematics to Hydro-*

carbon Systems. : Frontiers in Earth Sciences. Springer, Berlin, pp. 471–487.

Segall, P. (1985) Stress and subsidence resulting from subsurface fluid withdrawal in the epicentral region of the 1983 Coalinga earthquake, *J. Geophys. Res.*, *90*(B8), 6801-6816.

Segall, P. (1989). Earthquakes triggered by fluid extraction, *Geology* 17, 942-946.

Segall, P. (1992). Induced stresses due to fluid extraction from axisymmetric reservoirs, *Pure Appl. Geophys., 139(3/4)*: 535–560.

Segura, J. M., and I. Carol (2004), On zero-thickness interface elements for diffusion problems, Int. J. Numer. Anal. Methods Geomech., 28, 947–962.

Segura, J. M., and I. Carol (2008a), Coupled HM analysis using zero-thickness interface elements with double nodes. Part I: Theoretical model, Int. J. Numer. Anal. Methods Geomech., 32, 2083–2101.

Segura, J. M., and I. Carol (2008b), Coupled HM analysis using zero-thickness interface elements with double nodes. Part II: Verification and application, Int. J. Numer. Anal. Methods Geomech., 32, 2103–2123.

Serpelloni, E., M. Anzidei, P. Baldi, G. Casula, and A. Galvani (2006). GPS measurement of active strains across the Apennines, *Ann. Geophys. 49, no. 1*, 319-329.

Serpelloni, E. L. Anderlini, A. Avallone, V. Cannelli, A. Cavalier, D. Cheloni, C. D'Amborosio, E. D'Anastasio, A. Espositio, G. Pietrantonio, A. R. Pisani, M. Anzidei, G. Cecere, N. D"Agostino, S. Del Messe, R. Devoti, A. Galvani, A. Massucci, D. Melini, F. Riguzzi, G. Selvaggi, and V. Sepe. (2012). GPS observations of coseismic deformation following the May 20 and 29, 2012, Emilia seismic events (northern Italy): data, analysis and preliminary models. *Ann. Geophys. 55, 4, 759-766 doi: 10.4401/ag-6168*

Settari, A., and F. Mourits (1998), A coupled reservoir and geomechanical simulation system, Soc. Pet. Eng. J., 3, 219–226.

Settari, A., and D. A. Walters (2001), Advances in coupled geomechanical and reservoir modeling with applications to reservoir compaction, Soc. Pet. Eng. J., 6, 334–342.

Shaw, J. and J. Suppe (1994) Active faulting and growth folding in the eastern Santa Barbara Channel, California, *Geol. Soc. Amer. Bull., 106/5*, 607-626.

Shaw, J. H. and J. Suppe (1996) Earthquake hazards of active blind-thrust faults under the central Los Angeles basin, California, *J. Geophys. Res., 101/B4*, 8623- 8642.

Sibson, R. H. (1977), Fault rocks and fault mechanisms, J. Geol. Soc. London, 133, 191–213.

Sibson, R. H. (1981), Fluid flow accompanying faulting: Field evidence and models, in Earthquake Prediction: An International Review, Maurice Ewing Ser., vol. 4, pp. 593–603, AGU, Washington, D. C.

Sibson, R. H. (1986), Brecciation processes in fault zone: Inferences from earthquake rupturing, Pure Appl. Geophys., 124, 159–175.

Sibson, R. H. (1990), Rupture nucleation on unfavorably oriented faults, Bull. Seismol. Soc. Am., 80, 1580–1604.

Sibson, R. H. (1994), Crustal stress, faulting and fluid flow, Geol. Soc. Spec. Publ., 78, 69–84.

Skempton, A. W. (1954), The pore pressure coefficients A and B, Geotechnique, 4, 143–147.

Stein, R.S. (1999). The role of stress transfer in earthquake occurrence: *Nature, 402*, 605–609.

Stein, R.S. (2003). Earthquake conversations, *Scientific American, 288*, 72-79.

Stein, R. and R. Yeats (1989) Hidden earthquakes, *Scientific American, 260, pp. 48-57.*

Sukirman, Y., and R. W. Lewis (1993), A finite element solution of a fully coupled implicit formulation for reservoir simulation, Int. J. Numer. Anal. Methods Geomech., 17(10), 677–698.

Szulczewski, M. L., C. W. MacMinn, H. J. Herzog, and R. Juanes (2012), Lifetime of carbon capture and storage as a climate-change mitigation technology, Proc. Natl. Acad. Sci. U. S. A., 109(14), 5185–5189.

Taira, T., P. G. Silver, F. Niu and R. M. Nadeau (2009). Remote triggering of fault-strength changes on the San Andreas fault at Parkfield. *Nature, 461*(7264), 636-9. doi:10.1038/nature08395

Thomas, L. K., L. Y. Chin, R. G. Pierson, and J. E. Sylte (2003), Coupled geomechanics and reservoir simulation, Soc. Pet. Eng. J., 8(4), 350–358.

Toda, S., R. R. Stein and T. Sagiya (2002). Evidence from the 2000 Izu Islands swarm that seismicity is governed by stressing rate: *Nature, 419*, 58-61.

Toda, S., R. S. Stein, K. Richards-Dinger and S. Bozkurt (2005). Forecasting the evolution of seismicity in southern California: Animations built on earthquake stress transfer, *J. Geophys. Res., 110*, B05S16, doi:10.1029/2004JB003415.

Toda, S., R. S. Stein, G. C. Beroza and D. Marsan (2012). Aftershocks halted by static stress shadows. *Nature Geoscience*, *5*(6), 410-413.

Townend, J., and M. D. Zoback (2000). How faulting keeps the crust strong, *Geology*, 28, 399– 402.

Tran, D., A. Settari, and L. Nghiem (2004), New iterative coupling between a reservoir simulator and a geomechanics module, Soc. Pet. Eng. J., 9(3), 362–369.

Tran, D., L. Nghiem, and L. Buchanan (2005), Improved iterative coupling of geomechanics with reservoir simulation, paper SPE 93244 presented at SPE Reservoir Simulation Symposium, Society of Petroleum Engineers, Houston, Tex.

van der Elst, N. J. and E. E. Brodsky (2010). Connecting near-field and far-field earthquake triggering to dynamic strain. *J. Geophys. Res.*, 115(B7). doi:10.1029/2009JB006681

van der Elst N. J., Savage H. M., Keranen K. M., Abers G.A. (2013). Enhanced Remote Earthquake Triggering at Fluid-Injection Sites in the Midwestern United States. *Science*, **341**: 164-167.

Vlahinic, I., H. M. Jennings, J. E. Andrade, and J. J. Thomas (2011), A novel and general form of effective stress in a partially saturated porous material: The influence of microstructure, Mech. Mater., 43, 25–35.

Waldhauser, F. and W. L. Ellsworth (2000). A double-difference earthquake location algorithm: Method and application to the northern Hayward fault, *Bull. Seismol. Soc. Amer.*, 90, 1353-1368, 2000.

Wang, H. F. (2000). Theory of Linear Poroelasticity, *Princeton University Press*, Princeton, NJ, 287 pp.

Wang, C. Y., L. H. Cheng, C. V. Chin, and S. B. Yu (2001), Coseismic hydrologic response of an alluvial fan to the 1999 Chi-Chi earthquake, Taiwan, Geology, 29, 831–834.

Wang, C. -Y., C. H. Wang and M. Manga (2004). Coseismic release of water from mountains: Evidence from the 1999 (mw= 7.5) chi-chi, taiwan, earthquake. *Geology*, 32(9), 769-772.s doi:doi:10.1029/2002JB002321

West, M., J. J. Sánchez and S. R. McNutt (2005). Periodically triggered seismicity at mount wrangell, alaska, after the sumatra earthquake. *Science*, 308(5725), 1144-1146. doi:doi:10.1029/2002JB002321

Yerkes, R. F., and R. O. Castle (1976), Seismicity and faulting attributable to fluid extraction, Eng. Geol., 10, 151–167.

Zienkiewicz, O. C., D. K. Paul, and A. H. C. Chan (1988), Unconditionally stable staggered solution procedure for soil–pore fluid interaction problems, Int. J. Numer. Methods Eng., 26(5), 1039–1055.

Zoback, M. D., and S. M. Gorelick (2012a), Earthquake triggering and large-scale geologic storage of carbon dioxide, Proc. Natl. Acad. Sci. U. S. A., 109, 10,164–10,168.

Zoback, M. D. and J. Townend (2001). Implications of hydrostatic pore pressure and high crustal strength for the deformation of intraplate lithosphere: *Tectonophysics, 336,* 19-30.

Zoback M. L. and M. D. Zoback (1980). State of stress in the conterminus United States. *J. Geophys. Res., 85,* 6113-6156